AEROELASTIC INSTABILITY OF A STRUCTURAL ANGLE SECTION

by

JONATHAN ERNEST SLATER
B.A.Sc., University of British Columbia, 1964

A THESIS SUBMITTED IN PARTIAL FULFILMENT OF
THE REQUIREMENTS FOR THE DEGREE OF
DOCTOR OF PHILOSOPHY

in the Department
of
Mechanical Engineering

We accept this thesis as conforming to the
required standard

THE UNIVERSITY OF BRITISH COLUMBIA

March, 1969

In presenting this thesis in partial fulfilment of the requirements for an advanced degree at the University of British Columbia, I agree that the Library shall make it freely available for reference and Study. I further agree that permission for extensive copying of this thesis for scholarly purposes may be granted by the Head of my Department or by his representatives. It is understood that copying or publication of this thesis for financial gain shall not be allowed without my written permission.

JONATHAN E. SLATER

Department of MECHANICAL ENGINEERING

The University of British Columbia
Vancouver 8, Canada

Date April 25/69

ABSTRACT

Angle section members, used in open engineering structures, have been known to experience large amplitude oscillations when exposed to normal atmospheric winds, and in a few instances failure has been reported. The bluff geometry together with low natural frequency make these members susceptible to aeroelastic vibrations of a vortex resonant or galloping nature. The thesis aims at studying the nature of the aerodynamic forces and the resulting instabilities for the safe design of the structures. It presents information on the aerodynamics and dynamics of the angle section during stationary, plunging, torsional and combined plunging-torsional conditions.

From the measurements on stationary angle models, it is possible to predict the critical vortex resonant wind speeds for various angles of attack. The large variations of the unsteady aerodynamic coefficients indicate the dependence of the resonant instability on model orientation. Incorporating the stationary aerodynamic loadings, the quasi-steady analysis is able to predict the galloping instability and resulting amplitude and build-up time response. The absence of torsional galloping during the experiment is substantiated by the theory which shows the instability to occur only at high wind speeds or for systems with very low damping.

The dynamical study demonstrates that structural angle sections are susceptible, in general, to combined plunging and torsional vibrations. The nature of the instability depends on such system parameters as damping, natural frequency, angle of

attack, section size, etc. However, due to the existence of two distinct families of virtual hinge points, it is possible to represent the motion as predominantly plunging or torsion. Furthermore, the frequency of the coupled motion as well as the type and range of the instability are found to be similar to those in the single degree of freedom. This makes it possible to obtain pertinent information by studying, both experimentally and theoretically, the plunging and torsional degrees of freedom, separately.

During plunging resonance, the angle section experiences a vortex capture phenomenon where the shedding frequency is controlled by the cylinder motion over a finite wind speed range. On the other hand, the torsional vibration shows a vortex control condition over a large velocity range where the vortex shedding governs the frequency of oscillation and follows the stationary model Strouhal curve. Compared to the stationary and torsional results, the fluctuating pressures on the angle surface during plunging resonance are substantially larger in magnitude with less amplitude modulation and phase variation. Consequently, the unsteady aerodynamic coefficients increase with this instability. During resonance in either degree of freedom, the vortex velocity and longitudinal spacing remain essentially unaltered, however, the wake width experiences substantial increase with plunging motion. It appears that the torsional resonance has virtually no effect on the vortex shedding or wake characteristics.

TABLE OF CONTENTS

Chapter Page

LIST OF TABLES

LIST OF FIGURES

ACKNOWLEDGEMENT

The author wishes to express his sincere thanks and appreciation to Dr. V.J. Modi for the guidance and assistance given throughout the research programme and during the preparation of the thesis. His help and encouragement have been invaluable. The constant interest and encouragement shown by Dr. G.V. Parkinson during the experimental work, and helpful comments on the theoretical aspects of this study require special appreciation.

Thanks are also due to the Department of Mechanical Engineering for the use of their facilities, and to the technical staff members for their valuable help during the construction of the wind tunnel models and support systems, and the assemblying of electronic instrumentation.

Reduction of some of the experimental data and computer output, and typing of the original thesis manuscript were performed by my wife. Her hours of assistance are greatfully appreciated.

Financial assistance was received from the National Research Council of Canada in the form of direct postgraduate scholarship and operating grant (No. A-2181).

LIST OF SYMBOLS

C_L, C_D, C_M	Steady lift, drag and pitching moment coefficients, respectively
C_{F_y}	Lateral force coefficient
C_{M_θ}	Pitching moment coefficient
C_l, C_d, C_m	Sectional steady lift, drag and pitching moment coefficients, respectively
$C_{\bar{l}'}$, $C_{\bar{d}'}$, $C_{\bar{m}'}$	Average peak, fluctuating sectional lift, drag and pitching moment coefficients, respectively
C_p	Mean static pressure coefficient, $(p-p_o)/\frac{1}{2}\rho V^2$
$C_{\bar{p}'}$	Average peak fluctuating pressure coefficient, $\bar{p}'/\frac{1}{2}\rho V^2$
D	Drag, $\frac{1}{2}\rho V^2 h 1 C_D$
F_y	Lateral force for plunging system, $\frac{1}{2}\rho V^2 h 1 C_{F_y}$
I	Mass moment of inertia about elastic axis
$\bar{I}_o$	Mass moment of inertia about inertial axis
K_θ	Reduced frequency parameter for torsional galloping theory
L	Lift, $\frac{1}{2}\rho V^2 h 1 C_L$
M	Pitching moment, $\frac{1}{2}\rho V^2 h^2 1 C_M$
M_θ	Pitching moment for torsional system, $\frac{1}{2}\rho V^2 h^2 1 C_{M_\theta}$
N	Degree of polynomial curve fit
N_R	Reynolds number, Vh/ν
R_r	Dimensionless representative radius parameter, r_r/h
S_e, S_h	Strouhal numbers, $f_v e/V$ and $f_v h/V$, respectively
U	Dimensionless fluid velocity, $V/\omega_n h$

U_o	Dimensionless critical velocity, $2\beta/na_1$
U_{res}	Dimensionless resonant wind velocity, $1/(2\pi S_h)$
V	Fluid velocity far upstream of angle model
V_{rel}	Fluid velocity relative to oscillating cylinder
V_{res}	Resonant wind velocity, $\omega_n h U_{res}$
V_v	Streamwise vortex velocity
Y	Dimensionless lateral displacement of oscillating model, y/h
$\bar{Y}$	Dimensionless amplitude of lateral displacement, $\bar{y}/h$
$\bar{Y}_o$	Dimensionless initial amplitude of lateral displacement
a	Longitudinal spacing between vortices
a_i	(i=0,1,2,3,•••••,N) coefficients of polynomial curve fit
b	Lateral spacing between vortices
c	cos λ
e	Projected width of angle model
f_c	Frequency of cylinder oscillations
f_{n_y}	Natural frequency in plunging, $\omega_{n_y}/2\pi$
f_{n_θ}	Natural frequency in torsion, $\omega_{n_\theta}/2\pi$
f_v	Frequency of vortex shedding
h	Maximum width of angle model
k_y, k_θ	Plunging and torsional stiffnesses of the system, respectively
l	Length of angle model
m	Mass of oscillating system
n_y	Dimensionless mass parameter, $\rho h^2 l/(2m)$
n_θ	Dimensionless mass moment of inertia parameter, $\rho h^4 l/(2I)$
p	Mean static pressure

p_o	Static pressure far upstream of angle model
p'	Fluctuating static pressure
$\bar{p}'$	Average peak of fluctuating static pressure
r	Radial distance from elastic axis to surface element
r_y, r_θ	Plunging and torsional viscous damping coefficients, respectively
s	$\sin \lambda$
t	Real time
u	Velocity of vortex relative to surrounding fluid
v	Surface element velocity for torsional oscillation
x	Downstream coordinate from angle section inertial axis
y	Tranverse coordinate from angle section inertial axis or instantaneous lateral displacement of oscillating model, normal to flow direction
$\bar{y}$	Amplitude of lateral displacement
z	Coordinate along elastic axis from model midspan
Θ	Torsional displacement of oscillating model, $\equiv \theta$
$\bar{\Theta}$	Amplitude of torsional displacement
$\bar{\Theta}_o$	Initial amplitude of torsional displacement
Φ_{AF}	Phase lag between model displacement and fluctuating force or moment
Ω_v	Vortex frequency ratio, ω_v/ω_n
Ω_θ	System frequency ratio, $\omega_{n_\theta}/\omega_{n_y}$
α	Instantaneous angle of attack of oscillating system or attitude of stationary model
α_o	Mean angle of attack of oscillating system
β_y	Dimensionless damping parameter for plunging system, $r_y/2m\omega_{n_y}$
β_θ	Dimensionless damping parameter for torsional system, $r_\theta/2I\omega_{n_\theta}$

γ	Angle between relative and approaching fluid velocities for oscillating system
ε	Increment in angle of attack of oscillating torsional system, $\alpha-\alpha_o$
ζ	Coordinate along contourline of C_{M_θ}, passing through origin
η	Angle between surface element velocity and approaching fluid velocity for oscillating torsional system
η_{r_o}	Value of η_r at $\alpha_o=0°$
θ	Torsional displacement of oscillating system
λ	Angle between ζ and $\dot{\theta}/U$ axis
ν	Kinematic viscosity of the fluid
ξ	Coordinate perpendicular to ζ axis
ρ	Density of the fluid
σ	Distance between inertial and elastic axes
τ	Dimensionless time for oscillating system, $\omega_n t$
τ_v	Dimensionless time for vortex shedding, $\omega_v t$
τ^*	Reduced dimensionless time for oscillating system, $\beta\tau$
ϕ	Phase angle
$\overline{\phi}'$	Average phase angle between fluctuating pressure signals
ω_c	Circular frequency of cylinder oscillations
ω_n	Natural circular frequency of oscillating system
ω_{n_y}	Natural circular frequency in plunging, $(k_y/m)^{1/2}$
ω_{n_θ}	Natural circular frequency in torsion, $(k_\theta/I)^{1/2}$
ω_v	Circular frequency of vortex shedding

Subscripts

F	Value of the parameter under free stream conditions
e	Parameter based on projected width e
m	Pressure on model surface
max	maximum
r	Average value of the parameter for torsional oscillations of angle section
s	Value of the parameter for stationary model
w	Value of the parameter in wake
y	Value of the parameter in plunging
θ	Value of the parameter in torsion
∞	Constant value of the parameter at a large distance downstream

Superscripts

$(\cdot)$	Derivative with respect to dimensionless time τ
$(\circ)$	Derivative with respect to real time t
*	Reduced value of the displacement or velocity, parameter/U_o

1 INTRODUCTION

1.1 Preliminary Remarks

The oscillations of aerodynamically bluff bodies, when exposed to a fluid stream, have been a subject of considerable study. To engineers, the aeroelastic vibrations of smoke stacks, transmission lines, suspension bridges, buildings, etc., are of interest. In general, the nature of the wind loading, vortex shedding frequency and wake geometry form three important parameters in an aeroelastic instability study. The determination of the corresponding information associated with a structural angle, during static and dynamic conditions, forms the subject of this thesis.

Structural angles are frequently used in the construction of open civil engineering structures, such as high voltage transmission towers, antenna masts, and bridges. Incorporated as secondary members, these structural sections may be long and flexible. Furthermore, recent advances in the metallurgical science through experimental research and in engineering design with the aid of computers have encouraged the use of lighter and relatively more flexible individual components. Bluff geometry together with low natural frequency make these members particularly susceptible to aerodynamically induced vibrations. Some long slender angle members in transmission towers have been known to experience large amplitude oscillations when exposed to normal atmospheric winds, and in a few instances failure has been reported. It is, therefore, desirable to understand the nature of

the unsteady forces and the resulting instabilities for the safe design of these structures.

Depending on the nature of the aerodynamic excitation, a flexible structural member may exhibit various forms of vibration, e.g., vortex resonance, geometric-aerodynamic instability called galloping, classical or stall flutter, or random motion excited by the turbulence. However, in general, the aerodynamically induced oscillations of bluff cylinders are of the vortex resonant or galloping type with the vibrations occurring, predominately, in one of two degrees of freedom; flexure transverse to the flow direction, or torsion about the longitudinal elastic axis of the beam. Furthermore, since the elastic and inertial axes of angle members are not coincident, coupled torsional-flexural vibrations may occur. Nevertheless, as determined by Kosko[1] and observed by Wardlaw,[2] the coupled torsional-flexural oscillations can be considered as rotational motion about virtual hinge points which produces two distinctly different families of vibration. At the lower modes, one family appears predominantly flexural and the other torsional.

The natural turbulence of atmospheric winds to which the structural members are exposed is not, in general, comparable to that in the steady air stream of conventional wind tunnels. The atmospheric winds have fluctuating velocity components which may be a large fraction of the mean wind speed. However, since the peak of the power spectrum of the velocity fluctuations generally occurs at a frequency, which is much lower than the natural frequencies of typical angle section beams,[3] the atmospheric turbulence cannot be expected to cause serious resonant vibration

of individual structural members. On the other hand, buffetting by highly turbulent wakes from other bluff structures is more likely to cause excitation of members lying downstream since the turbulent energy spectrum can have peak(s) near the natural frequencies. Nevertheless, available literature reports that turbulence reduces the spanwise correlation of the vortex shedding phenomenon and thereby aids in suppressing the resonant vibrations. For the galloping instability, it should be mentioned that the influence of turbulence is not yet fully understood and may be significant under some circumstances.

The distinct character of vortex excited and galloping oscillations should be emphasized. The former is essentially a resonance phenomenon where the vortex formation frequency, and hence the frequency of the forcing function, coincides with the natural frequency of the system under consideration. This type of oscillation is referred to as a forced vibration since the sustaining alternating force exists independent of the motion and persists even when the motion is stopped. Although any bluff member of arbitrary cross-section, when suitably mounted, would exhibit vortex excited oscillation, the available literature is largely confined to such studies on circular cylinders because of the geometric simplicity as well as the practical importance of the section.

The second form of instability, referred to as galloping, represents an important type of self-excited vibration. The fluid forces which create a condition of instability are generated by the fact that the cross-section of the body is aerodynamically

unstable to small disturbances. These forces result in oscillations which grow in amplitude until the energy extracted from the fluid stream balances that dissipated through various forms of damping. Galloping oscillations are referred to as "self-excited" because the fluid forces that sustain the motion are created and controlled by the motion itself, and if the motion stops, the unsteady forces disappear. This is in contrast to vortex resonance. The main features of galloping are that the vibration can occur in a single degree of freedom and the steady-state amplitude tends to increase with increasing wind velocity.

Often, as is the case with a structural angle beam, the instability at a given fluid stream velocity and angle of attack may be the combined effect of both vortex resonance and galloping. To permit the study of the individual forms of excitation, the judicious choice of either damping, angle section size or natural frequency is required to separate the two phenomena.

1.2 Literature Survey

Strouhal[4] was the first to correlate the periodicity of the vortex shedding with the diameter of the circular cylinder and velocity of the fluid stream. This was followed by numerous experiments on wake geometry by Bénard,[5] the classical study of stability by Von Kármán,[6] and wake analysis by Heisenberg.[7] Ever since, interest in the vortex shedding phenomenon has resulted in many theoretical and experimental investigations by Roshko, Kovasnay, Rosenhead, Eskinazi and others. Marris[8] has presented an excellent review of this literature.

The mechanism of galloping excitation of bluff cylinders was probably first described by Den Hartog[9] together with the determination of his plunging stability criterion. Originally, however, it was Lord Rayleigh[10] who indicated the inadequacy of linear theory and proposed a nonlinear equation to explain the "sustained" oscillations. Van der Pol's development of his classical nonlinear equation in 1920 led to a flurry of research activity on this subject by Appleton, Greaves and others. Excellent reviews of these developments are summarized by van der Pol[11] and Le Corbeiller,[12] with many recent references found in Minorsky.[13] Wardlaw[2] extended Den Hartog's analysis by developing a generalized stability criterion for coupled torsional-flexural motion. Sisto,[14] Scruton,[15] Parkinson, et al, [16-18] Ii,[19] Dicker,[20] Novak,[21] etc., applied the quasi-steady approach to solve the nonlinear vibration problems for bodies of various geometric shapes with plunging and/or torsional degrees of freedom. The galloping oscillations of existing structures, mainly of transmission conductor lines, were observed and studied by Scruton,[22] Richardson, et al,[23] Cheers,[24] Dryden and Hill[25] and others. Davenport[26] suggested the possibility of galloping instability of tall thin buildings which may be constructed in the near future. A paper by Parkinson[27] discusses the aeroelastic behaviour of bluff cylinders and provides a good survey of the literature.

Scruton, as well as Davenport and associates have invesitgated in detail the wind loading and dynamics of certain complete structures such as stacks, towers, masts and buildings. On the other hand, Dale, et al,[28] have concentrated their study to the

dynamic behaviour of hydrophone cables. Intensive investigations into the aerodynamic instability of suspension bridges with special reference to the original Tacoma Narrows Bridge have been conducted by Farquharson, et al,[29] Kelley,[30] etc.

In addition to this, the unsteady forces and wake geometry associated with two-dimensional bluff cylinders have been intensively studied. McGregor[31] and Gerrard[32] have conducted experimental investigations of the fluctuating pressures on stationary circular cylinders. More recently, Ferguson[33] made wake survey as well as fluctuating surface pressure measurements on the same section. The corresponding results for stationary square, rectangular, and elliptical cylinders were presented by Modi and Heine,[34] and Wiland.[35] Similarly, Grove, et al,[36] Bishop and Hassan,[37] Humphreys,[38] and Fung[39] measured the fluctuating forces on stationary circular cylinders over different ranges of Reynolds number. In addition, Wardlaw and Davenport,[3] and Vickery[40] conducted some fluctuating force measurements on different shapes in laminar as well as in turbulent flow.

On the other hand, investigation of wake and surface conditions on oscillating bluff cylinders is less complete. The study of fluctuating lift and drag forces by Bishop and Hassan[41] showed that the vortex frequency is controlled over a range of circular cylinder frequencies; while Ferguson and Parkinson[42] measured fluctuating pressures and wake geometry related to a circular cylinder experiencing vortex induced oscillations. Molyneux[43] developed techniques for measuring the aerodynamic forces on oscillating airfoils. The three-dimensional structure of the wake and correlation along a circular cylinder during static or dynamic conditions have been investi-

gated by Gerrard,[44] Toebes,[45] Prendergast,[46] Feng[47] and others. Vickery[40] measured the correlation of lift along the surface of a stationary square cylinder.

Dynamic amplitude measurements of two-dimensional bluff cylinders of various cross sections have been investigated by Brooks.[48] Both Smith[49] and Santosham[50] concentrated their studies to aeroelastic galloping of rectangular cylinders in a plunging degree of freedom; while Chuan[51] and Otsuki[52] present investigations on torsional oscillations of airfoils and prismatic bars, respectively. On the other hand, Toebes and Eagleson,[53] and Eagleson, et al,[54] dealt with the hydroelastically self-excited vibrations of flat plates as related to the trailing edge geometry.

The influence of wake-body interaction on aeroelastic instability are reported for bodies of various cross-sectional geometry. But it should be emphasized that the bulk of the literature is devoted to the circular section. This is indicated by the fact that investigations into aerodynamically excited oscillations of structural angles were not initiated until 1962. Thornton[55] conducted experiments on the vibration of several single and double angle section members in steady flow and was able to suppress the motion by the addition of flat plate spoilers. More recently, Wardlaw[2] has reported the oscillations of a 3x3x3/16 in. aluminum structural angle beam together with distributions of sectional lift, drag and pitching moment. From a structural consideration, the coupled flexural-torsional vibrations in still air of equal-legged and unsymmetrical angle section beams were examined theoretically and experimentally by Kosko.[1]

1.3 Purpose and Scope of the Investigation

The problem of aeroelastic instability of two-dimensional bluff cylinders has been actively studied, both experimentally and theoretically, in this department since 1958. A review of the progress is reported in two survey papers.[56,57] These systematic investigations have contributed pertinent data to the general study of wind effects on buildings and structures. The investigation described here forms a part of this continuing programme. It presents information on the aerodynamics of the angle section, the wind speed and angle of attack ranges of instability, and the effects of the model dynamics on the important aerodynamic parameters. This is intended to provide, eventually, a source of information for the safe design of open structures composed of this simple section.

In particular, the investigations examined the aerodynamics and dynamics of equal-legged, angle section models in a conventional low turbulence, return-type wind tunnel with a test section of 36 in. x 27 in. x 8 2/3 ft. The experimental models had 1x1 in. and 3x3 in. cross-sectional dimensions with uniform leg thicknesses of 1/6 in. and 1/2 in., respectively. The exterior surfaces were smooth with sharp contour edges. Being rigid in themselves, the models were mounted normal to the flow on stationary or spring supporting systems with structural and mean aerodynamic conditions being essentially two-dimensional. A comparison of the geometric features of the 'idealized' angle models and commercially available angle sections is presented in Appendix I.

The research programme was divided into four stages investigating the angle section during stationary, plunging, torsion, and combined plunging-torsion conditions. For the stationary model tests, the thesis presents experimental results on:

(i) steady lift, drag and pitching moment coefficients;

(ii) variation of Strouhal number with Reynolds number;

(iii) mean and fluctuating static pressure distributions;

(iv) fluctuating lift, drag and pitching moment coefficients;

(v) wake geometry

as functions of angle of attack. In most tests the Reynolds number was confined to the range 2×10^4 to 10^5. For comparison, static force and vortex shedding frequency measurements were conducted on commercially available aluminum and steel angle members.

The results of the remaining three stages are combined in one chapter of the thesis to correlate the important features of the model dynamics and associated aerodynamics. The existing lateral supporting equipment was suitable for the study in the plunging degree of freedom, but a new spring mounting system and auxiliary measuring instrumentation were designed for the torsional investigations. Both the vortex induced and galloping instabilities were examined at various angles of attack and damping levels for each of the three oscillatory modes of vibration. For the angle section experiencing vortex excited resonance, the effects of the model motion on such parameters as:

(i) vortex shedding frequency and phase;

(ii) fluctuating static pressure;

(iii) wake geometry

were determined. Peak vortex resonant displacement amplitudes were predicted from resonant theory by incorporating the fluctuating force data. In addition, using the experimentally obtained static aerodynamic loadings, the quasi-steady analysis was applied to provide theoretical predictions of the galloping model dynamics.

Since the influences of the wind tunnel walls on the measured data are not well established, the results presented, unless otherwise stated, are uncorrected for these effects. A number of experiments were conducted to establish trends of the wall interference, and this data together with a summary of existing theories on wall confinement corrections are presented in Appendix II.

A comment concerning the applicability of this investigation to a practical situation is pertinent here. The results presented in this thesis relate to a rigid, two-dimensional element of a long angle section beam, with the stiffness lumped as springs and damping applied externally. However, for an actual beam, the potential energy is due to the strains and damping is associated with the internal friction of the material. Nevertheless, Novak[21] has reported an investigation showing compatability between vibrations of rigid sections and continuous systems. A procedure for model simulation of physical structures has been presented by Whitbread.[58] For sectional models, certain similarity requirements have to be satisfied. When geometric similitude exists, the static aerodynamic results are directly applicable, even at other Reynolds numbers within a certain range, if flow

separation is fixed by edge condition. However, for dynamical studies, the requirements involve correspondence of structural parameters, such as stiffness, inertia and damping. They are represented in nondimensional form as $\bar{U}$, n and β, respectively.

In these experiments, the spring stiffnesses have been chosen to provide a frequency ratio $\omega_\theta/\omega_y \doteq 3$ which is typical of angle section beams.[1,2] The inertia characteristics of the 1 in. and 3 in. angle models (Appendix I) make the former suitable for plunging studies, while the latter for torsional investigations. For the 3 in. models in the plunging case, the n_y values are approximately 3 times higher than those of the prototype. This was selected for convenience, but does not limit the applicability of the results obtained. Several investigators[59,60, et al] have shown that the internal friction of solids can be approximated by viscous resistance or other energy dissipative models so that the decay of the vibration is logarithmic. However, other investigations[61,62] indicate that the logarithmic decrement is dependent on amplitude as well, with damping increasing with displacement. In any case, it is well known that the internal friction is a function of the material and its particular chemical and physical properties. Typical values for aluminum would be of the order of $0.001 < \beta < 0.01$, while for steel $0.0008 < \beta < 0.006$. With this uncertainty in the value of internal damping, it was thought advisable to conduct the tests with damping levels in and below the range likely to occur in the full-scale structure.

2 AERODYNAMICS OF A STATIONARY ANGLE SECTION

2.1 Preliminary Remarks

In an aeroelastic instability study, stationary model investigations provide vital information from which critical oscillatory conditions such as wind speed and model orientation can be predicted. A set of angle section models were subjected to extensive wind tunnel testing to obtain information concerning mean wind loading, Strouhal number, fluctuating static pressure and wake geometry.

This chapter describes model construction, necessary apparatus, instrumentation, and experimental procedures which also form the basis for the dynamical study in the following chapter. The test results are discussed and conclusions presented. A list of the electronic instruments used in the experimental programme is given in Appendix III.

2.2 Models, Apparatus, Instrumentation and Calibration

2.2.1 Angle Models

Depending on the type of experimental test proposed, the angle section models are categorized as follows:

(i) pressure tap model;

(ii) dynamic model;

(iii) balance model.

The designed angle models had sharp contour edges and relatively smooth faces to facilitate construction and provide uniformity of surface conditions. However, commercially available angles usually have rounded edges and rough surfaces. To determine the

influence of the disparities between the models and prototypes on certain aerodynamic characteristics, three balance models were made from steel and aluminum structural angle members.

To examine the mean and fluctuating static pressures on the surface of an angle section during static and dynamic conditions the pressure tap model was designed. The 3x3x1/2 in. hollow angle model, 26 3/4 in. long, was constructed from 0.020 in. aluminum sheet bonded to acrylic bulkheads and 1/4 in. thick end fastening tab plates (Figure 2-1). A 39 hole pressure ring of 0.025 in. diameter taps, located at the midspan of the model, provided a means of examining the pressure distributions around the contour of the angle. Two taps were provided in the spanwise direction, at distances of 4 1/2 in. and 9 in. from the midsection, at the same contour position as tap number 5. The surface pressure signals were transmitted from the pressure taps to externally located transducers through 5 ft. long, 0.066 in. diameter "Intramedic" polyethylene tubing. The 1 in. and 3 in. dynamic models, which did not have pressure taps, were of identical geometry.

Six different angle section models (Appendix I) were designed and built for mounting on the Aerolab six component, strain-gauge balance. Models A, B and C had the same nominal leg width and thickness, while model D and E had half the leg thickness. Models A and B differed only by the 1/4 in. thick end plates mounted on the latter model. This was intended to determine the effects of the same end plates mounted on the pressure tap and dynamic angle models. Models C and D were steel structural angles with rounded corners and rough sur-

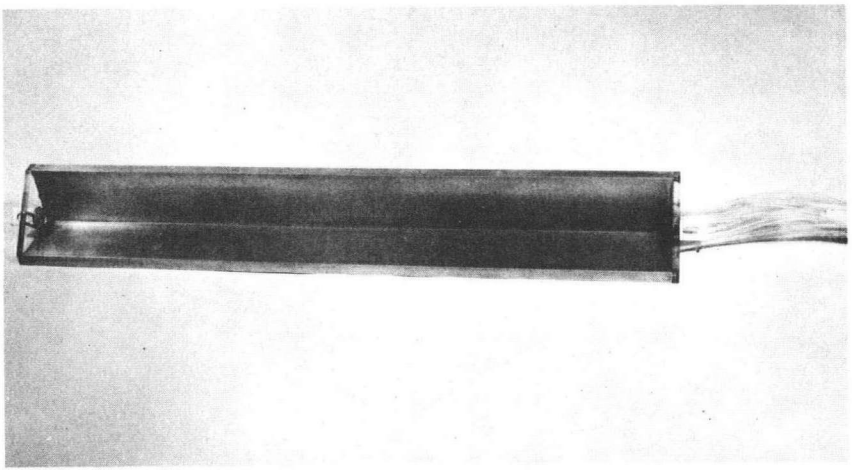

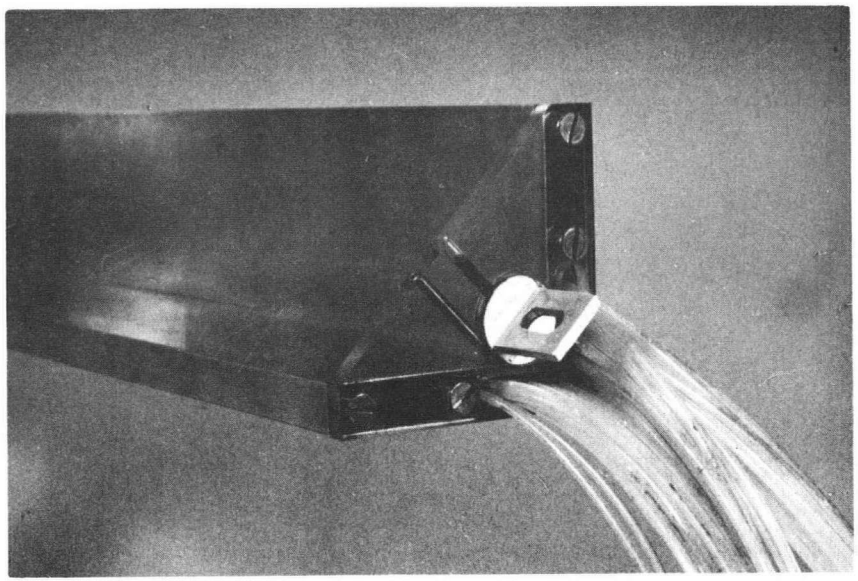

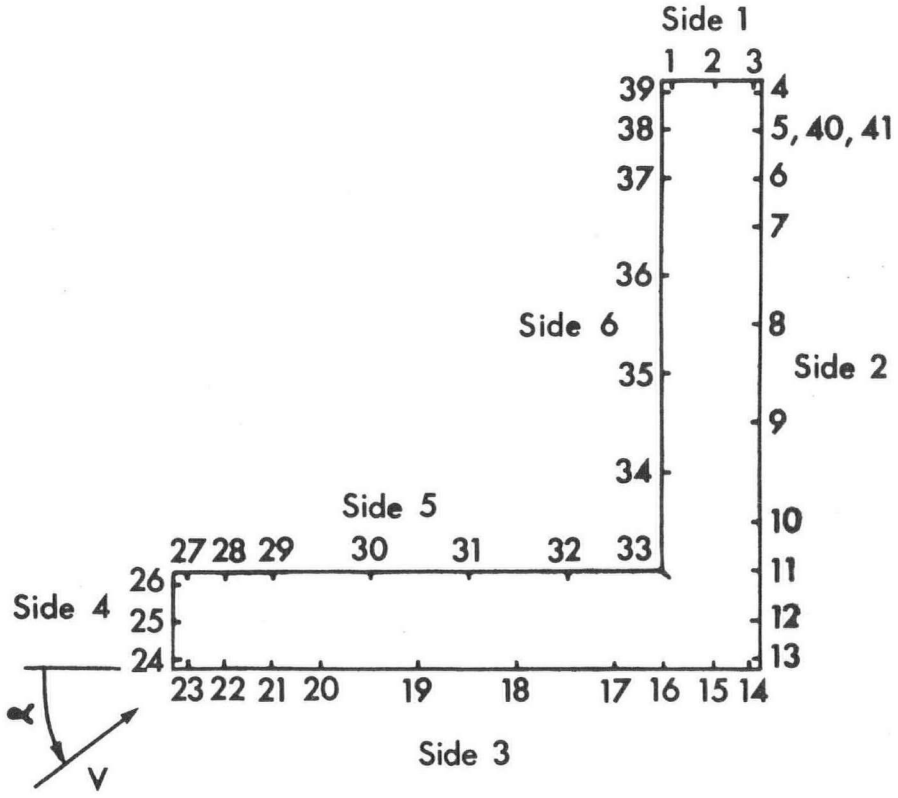

Figure 2-1 Pressure tap angle model and numbering of pressure holes and contour sides

faces. A typical commercial aluminum angle section with relatively smooth surface and small corner radius was represented by model E. Model F was geometrically similar to model B with cross-sectional dimensions of 2x2x1/3 in. For all balance models, the effective length which was exposed to the wind stream was nominally 27 in.

2.2.2 Fluctuating Pressure Transducer and Calibration

Datametrics Inc. of Waltham, Massachusetts, has developed a new pressure transducer called Barocel Modular Pressure Transducing System consisting of a pressure sensor, signal conditioner and power supply. The Barocel is a high precision, sensitive instrument which proved to be suitable for the intended fluctuating pressure measurements. The pressure sensor consists basically of a capacitive voltage divider with a stainless steel diaphragm separating the two pressure chambers. The signal conditioner provides 8 sensitivity ranges from 0-10 mm. of mercury on the least sensitive to 0-0.001 mm. of mercury on the most sensitive scale when coupled to a pressure sensor head. The output voltage is 0-5 volts d.c. full scale on any of the 8 sensitivity ranges with a linearity of ±0.1% and stability of ±0.1% for ±15°F ambient temperature changes. The prestressed diaphragm has a natural frequency of 2500 cps and the transient response of the pressure sensor head is less than 2 ms to a step pressure input. From experiment the Helmholtz resonator frequency of the cavity and connection on one side of the diaphragm was found to be approximately 210 cps.

The Barocel is accurately calibrated for steady pressures. However, for fluctuating pressures transmitted through relatively long, small diameter tubes considerable attenuation occurred. Therefore, the output electrical signal requires calibration against known input fluctuating pressure at the model surface. This was achieved using the calibration system developed by Wiland.[35]

The effect of amplitude and frequency of the source pressure on the output signal is shown in Figure 2-2(a). These curves indicate the linearity of the system. For convenience the calibration curves in Figure 2-2(a) were replotted in Figure 2-2(b) as a ratio of output to input. This eliminates frequency interpolation.

2.2.3 Wake Probe and Traversing Gear

The wake geometry survey was performed using a disc probe constructed by Ferguson[33] and described in detail by Bryer et al.[63] It was mounted on a 1 in. hypodermic needle which in turn was connected to a 14 in. long, 1/4 in. diameter sting. Static pressure calibration data were obtained for this particular probe from wind tunnel tests (Figure 2-3). The measurements indicate the probe to be relatively insensitive to a pitch of ±5° and yaw of ±20°. To enable the wake probe to be positioned in the test section of the tunnel with control of movement in a lateral and longitudinal direction, the wake traversing gear designed by Ferguson[33] was used. The accuracy in positioning the probe was approximately 0.02 in.

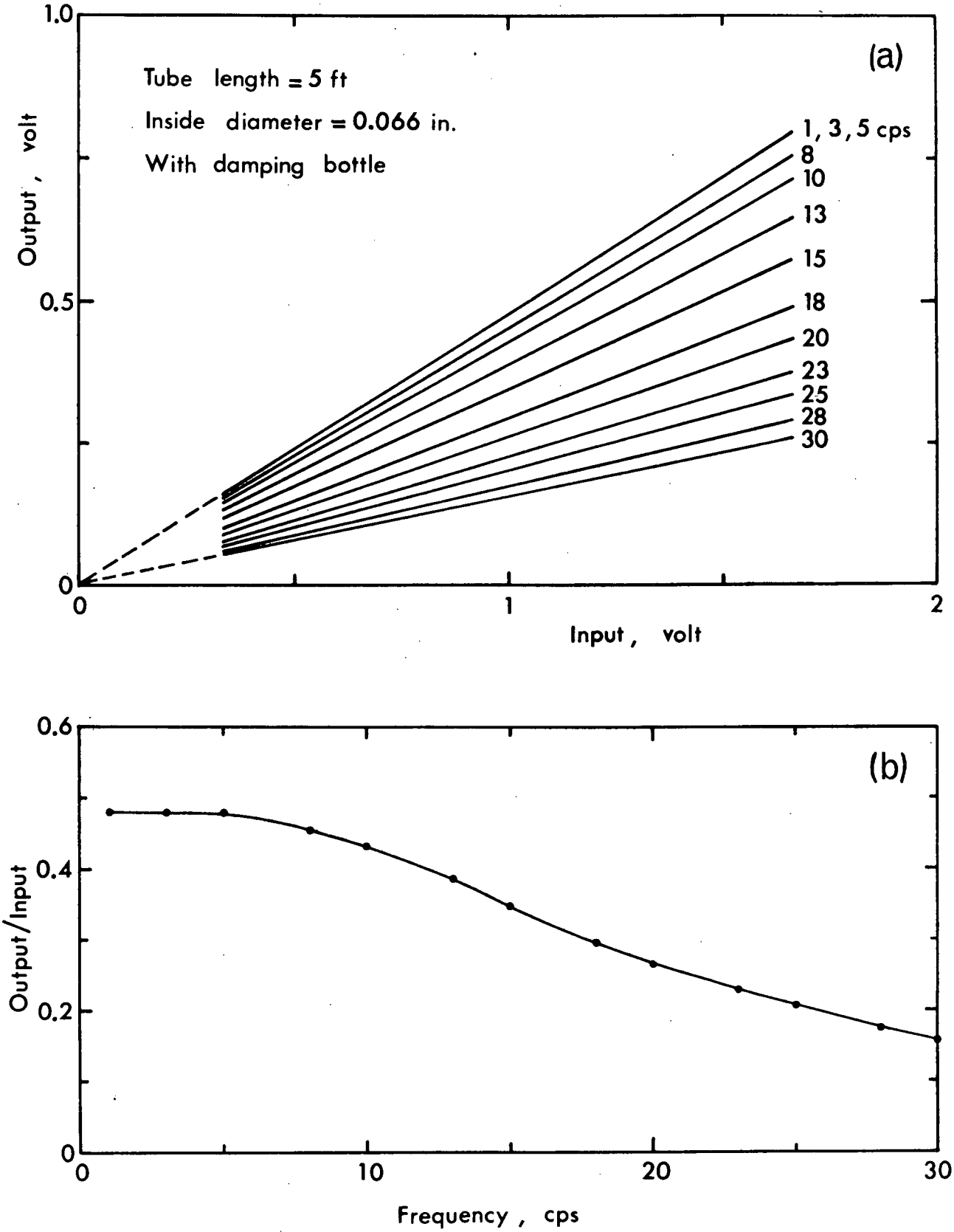

Figure 2-2 Calibration curves for Barocel transducer arrangement

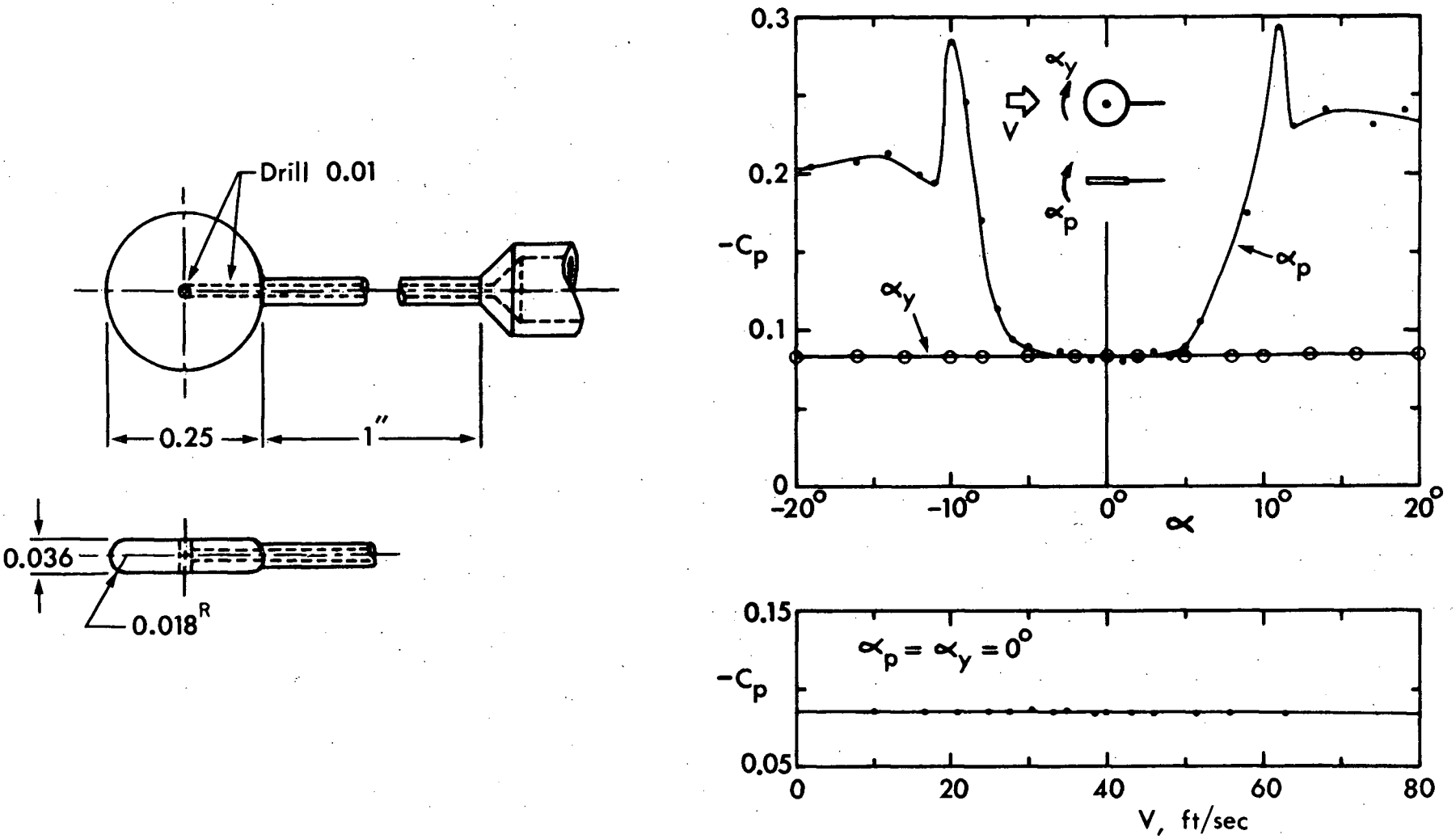

Figure 2-3 Dimensions and calibration data of disc probe

2.3 Test Procedures

2.3.1 Balance Measurements

After setting the angle of attack and increasing the wind speed to a preselected value, the lift, drag and pitching moment on a balance model were recorded. The wind speed was then increased to two further settings and corresponding data obtained. This procedure was repeated for the five balance models (A to E) over the entire range of angle of attack.

2.3.2 Vortex Shedding Frequency

Measurement of the Strouhal frequency was accomplished using the instrumentation layout shown in Figure 2-4. The wake probe was located at an appropriate position in the mid-plane where the fluctuating pressure signal was relatively clear. However, to improve the quality of the signal, a band pass filter was incorporated. Illustrated in Figure 2-5(a), are typical unfiltered and filtered fluctuating pressure signals from the probe. Using this system, the 1 in. and 3 in. angle models and the balance models (B,C,D,E, and F) were tested for vortex shedding frequency variation with angle of attack and Reynolds number.

2.3.3 Mean Static Pressure on Model Surface

The mean pressure distribution was obtained using a Lambrecht manometer with ethyl alcohol. The oscillation of the alcohol column caused by the fluctuating component of the static pressure was reduced using a restriction in the pressure line. To facilitate reduction of the data, the pressure on the model

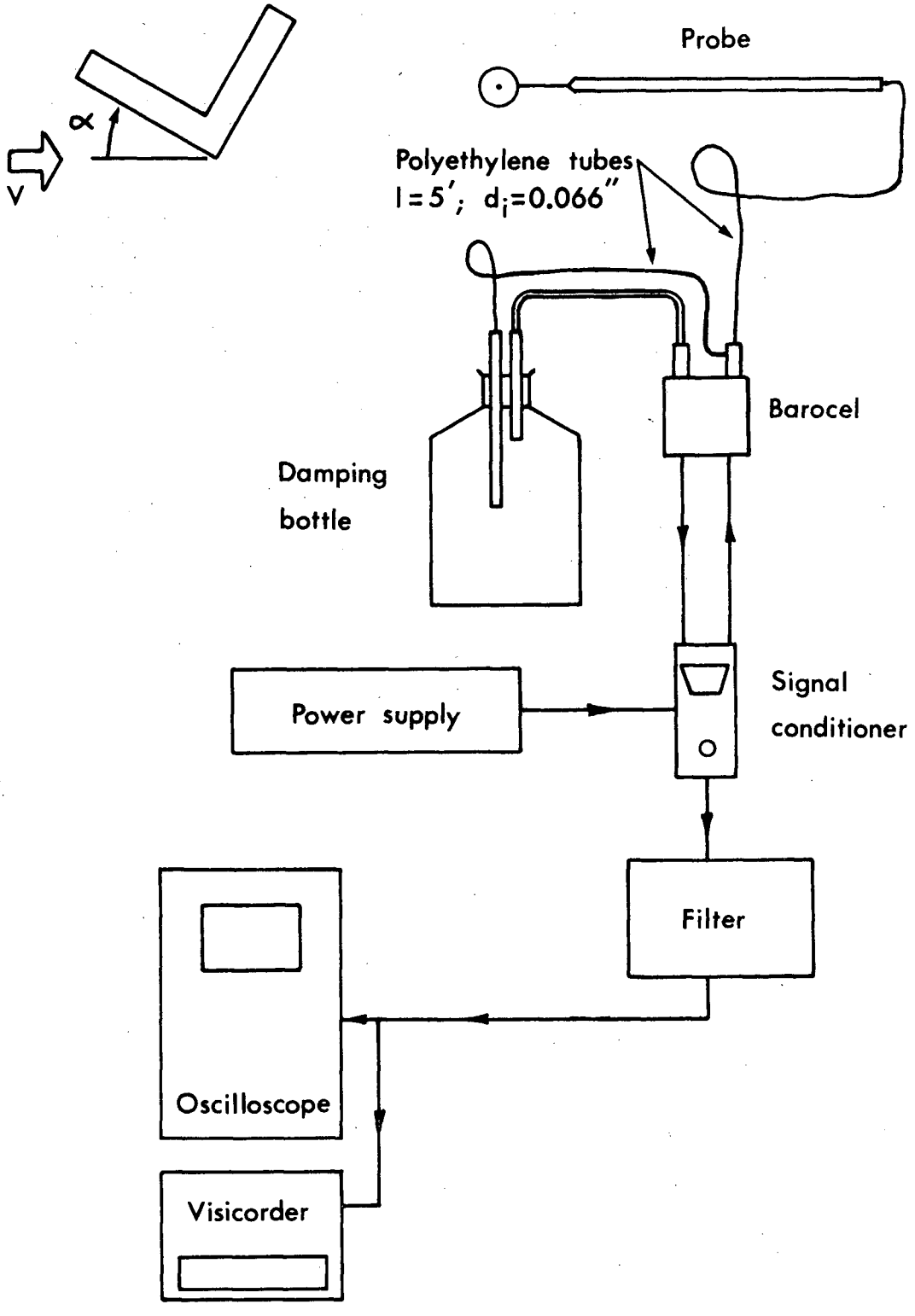

Figure 2-4 Instrumentation layout for vortex shedding frequency and fluctuating pressure measurements

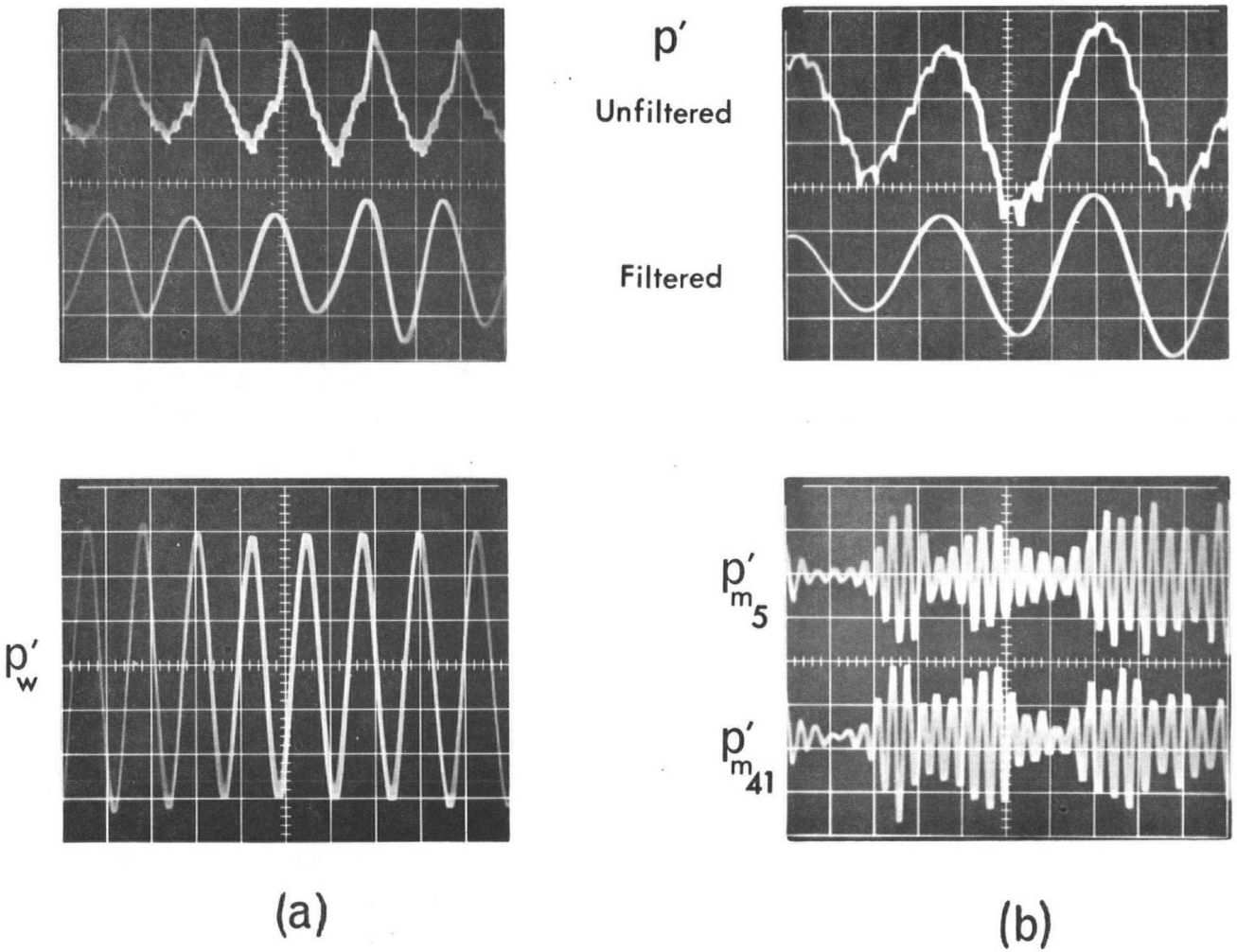

Figure 2-5 Typical fluctuating pressure signals from (a) wake probe (b) model surface

was measured relative to the total head in the settling section of the wind tunnel. This eliminated the effect of atmospheric pressure changes during the tests and produced a pressure differential which was always positive. The results were obtained for a range of wind speed and angle of attack.

2.3.4 Fluctuating Static Pressure on Model Surface

Investigation of the fluctuating pressure on the surface of the angle model was separated into amplitude and phase measurements. For studying the amplitude of the pressure fluctuations, the instrumentation shown in Figure 2-4 was used except that the signal was taken from the model taps and recorded on a Visicorder. As discovered by other investigators,[33,35] the fluctuating pressure signals on the model surface were at the frequency of the vortex shedding, and had seemingly random amplitude modulation. Figure 2-5(b) illustrates typical unfiltered, filtered and random amplitude modulated pressure signals from the model surface. For presentation of the fluctuating pressure amplitude, the average peak value over approximately 150 to 250 cycles was determined from the chart records. In addition, to evaluate the signal modulation, the ratio of maximum amplitude to average peak was obtained.

The phase difference between the fluctuating pressure signals from different model taps was obtained by incorporating a second Barocel transducer system and comparing the signals on Visicorder charts. To eliminate the effect of phase shift introduced by the instrumentation, the fluctuating pressure from one

model tap was arbitrarily selected as a reference. The relative phase angle was averaged over 10 to 20 cycles. The amplitude and phase measurements for the 41 pressure taps on the model were performed at three wind speeds and various angles of attack.

The band pass filter antenuation was determined for each wind speed and filter cut-off frequency settings by using a sinusoidal signal from a low frequency function generator. The Visicorder calibration and impedance attenuation were determined using the same procedure.

2.3.5 Wake Survey

Wake survey measurements were accomplished by examining the fluctuating pressure field associated with the vortices shed from the model using the instrumentation setup shown in Figure 2-6. Since the wake results were found to be substantially independent of Reynolds number, the measurements were confined to only one wind speed for various angles of attack.

Traversing the disc probe laterally at various x-stations and recording the average peaks of the fluctuating pressure signals provided a set of curves each having two maxima near the vortex centrelines. The y-distance between these maxima at each x-station was taken to be a measure of the lateral spacing between the two rows of vortices shed from the model. It was convenient to plot the results of the lateral traverse as a ratio of probe to model tap average fluctuating pressures. The model tap selected for the probe ratio was somewhat arbitrary, but represented a position on the model contour having a near maximum fluctuating pressure value. A true rms voltmeter was used for

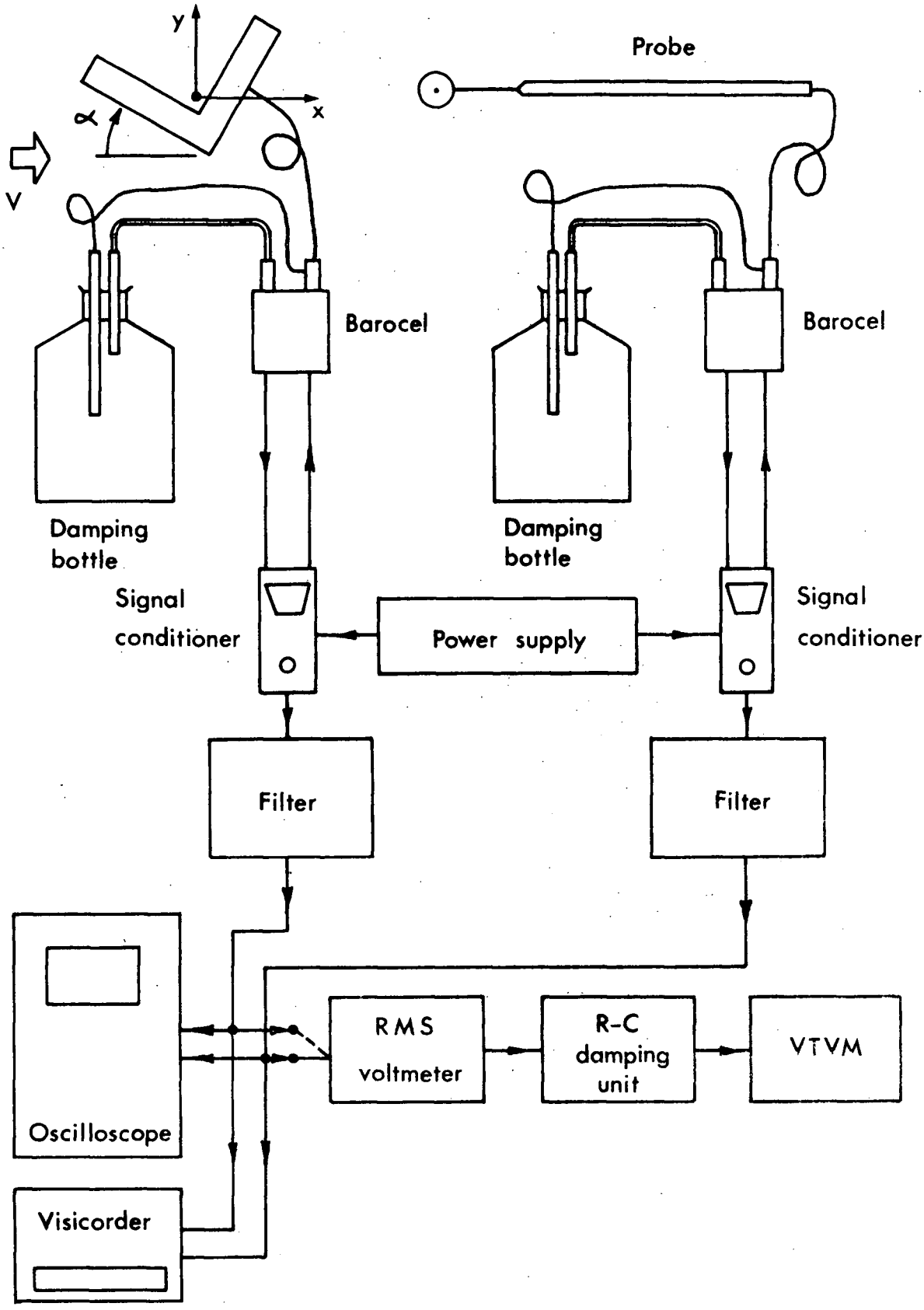

Figure 2-6 Schematic of instrumentation for wake survey measurements

averaging of the fluctuating pressure signals. The variation of the peak values with x coordinate gave an indication of the decay of the vortices in the downstream direction.

Longitudinal spacing, a, between consecutive vortices in one row of the vortex street was obtained indirectly from longitudinal phase measurements. The spacing distance corresponds to a 360° phase difference between the fluctuating pressure signals associated with consecutive vortices in the same row. Traversing the wake probe along the centreline of a vortex row, the fluctuating pressures from the probe and a reference model tap were recorded simultaneously on a Visicorder. The phase angle data, averaged over 10 to 20 cycles, was plotted as a function of the downstream coordinate from which the vortex spacing, a, was interpreted. In addition, the vortex streamwise velocity was determined from the longitudinal spacing using the relation

$$\frac{V_v}{V} = S_h\left(\frac{a}{h}\right) \qquad (2.1)$$

2.4 Experimental Results and Discussion

2.4.1 Steady Lift, Drag and Pitching Moment Distributions

The static lift, drag and pitching moment experienced by various angle sections over the Reynolds number range of 4×10^4 to 11×10^4 are presented in the following illustrations. The pitching moment has been measured relative to an axis coinciding with the centroid of an angle section. It was observed that over the wind speed range investigated, the force and moment

coefficients were independent of the Reynolds number.

Figure 2-7, presents the variation of the aerodynamic coefficients with angle of attack, α , for the balance model B which is geometrically similar to the pressure tap and dynamic angle models. It is apparent that the angle section experiences the maximum negative lift and moment at approximately $\alpha = 10°$ and corresponding maximum positive values near $\alpha = 40°$. On the other hand, the drag force is maximum at the symmetric angle $\alpha = -45°$ where the model angle section is open upstream. The variation of the drag coefficient with angle of attack can be reduced by basing the coefficient on the projected frontal area. However, the drag coefficient does not become completely independant of model orientation. A comparison of this data with the test results of model A indicated no significant influence of the 1/4 in. thick end plates on the overall aerodynamic characteristics.

The abrupt changes in the lift, drag and moment distributions at certain orientation such as $\alpha = 10°$, $40°$ and $104°$ are attributed to major changes in the flow field over the angle contour. This was substantiated by a qualitative study using a smoke tunnel. With the increase of angle of attack in the ranges 5° to 25° and 97° to 125°, the separated flow reattached on one side forming a separation bubble which decreased in length and finally disappeared producing attached flow over the entire side. In the vicinity of $\alpha = 40°$, the forward stagnation point shifted from the junction of sides 3 and 4 to approximately tap

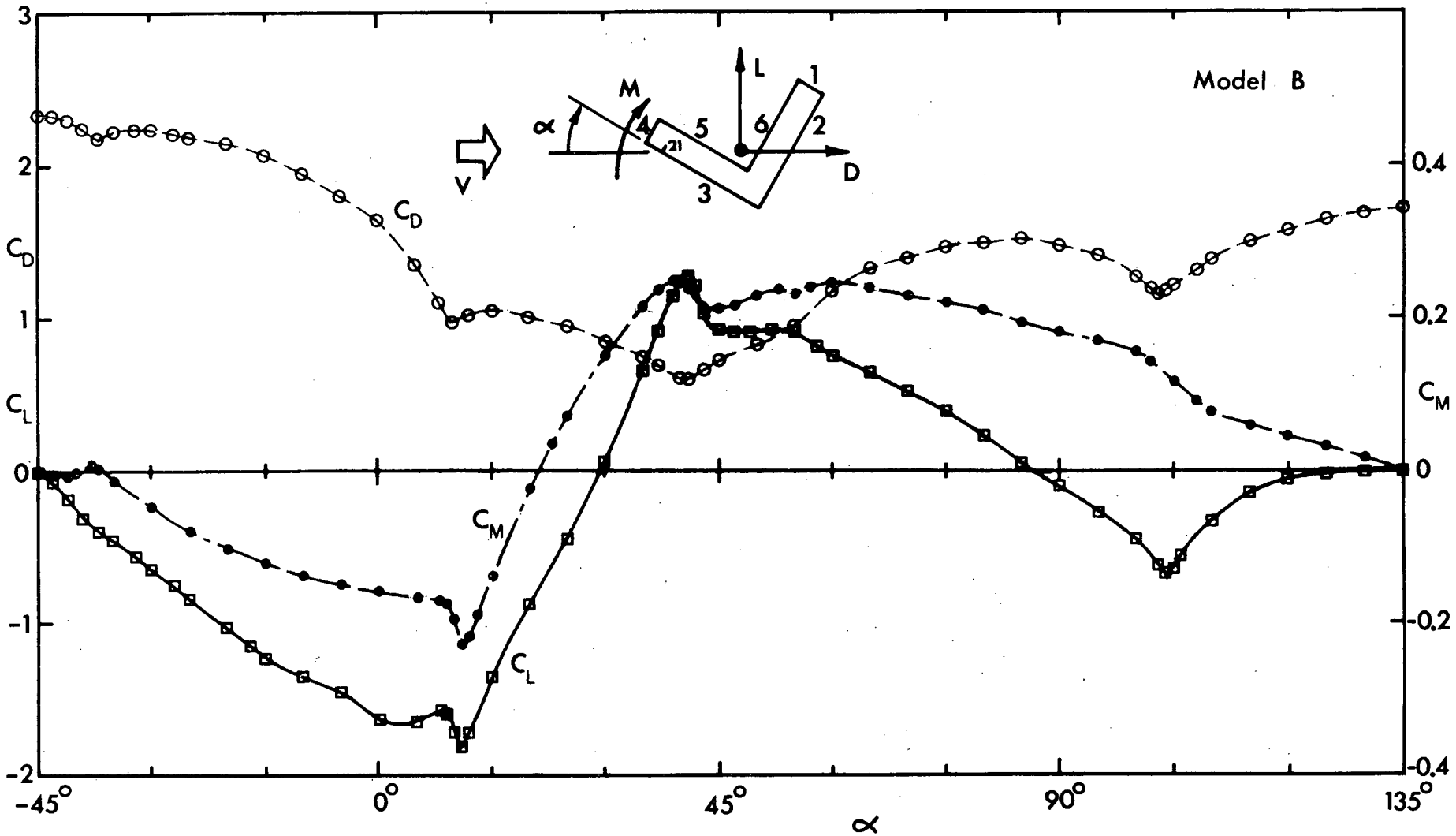

Figure 2-7 Distribution of steady lift, drag and pitching moment coefficients for balance model B

number 21 causing a change in the position of the separated shear layers downstream.

Figure 2-8 illustrates some of the effects of edge radius and surface roughness associated with commercially available angle members. The results show that angle model B and structural angle members C, D and E have reasonable aerodynamic similarity even though there are minor differences in geometric features. In Figure 2-8(c) slight deviations in the pitching moment distributions are apparent over the range of -45° to 15° due to differences in leg thickness and corner conditions. A comparison of the results suggests that a reduction in leg thickness or corner radius decreases the magnitude of the pitching moment. This variation is apparent from the mean static pressure distributions given later in Figure 2-12.

The present lift and drag distributions compare well with Wardlaw's measurements[2] and the few drag results for structural angles quoted by Hoerner.[64] For the angle models at $\alpha = -45°$, the corrected drag coefficient value of approximately 2.0 is similar to that of a normal flat plate or 90° wedge model.[64] Using the measured base pressure value for the pressure tap angle section at $\alpha = 135°$, Roshko's[65] notched hodograph solution for a 90° wedge, predicts a value of $C_D = 1.8$ which compares well with the experimental drag coefficient of 1.7 for balance model B.

2.4.2 Vortex Shedding Frequency and Strouhal Number

The dependence of the vortex shedding frequency on wind speed is shown in Figure 2-9 for various angles of attack of the pressure tap angle model. The linearity of the plots in-

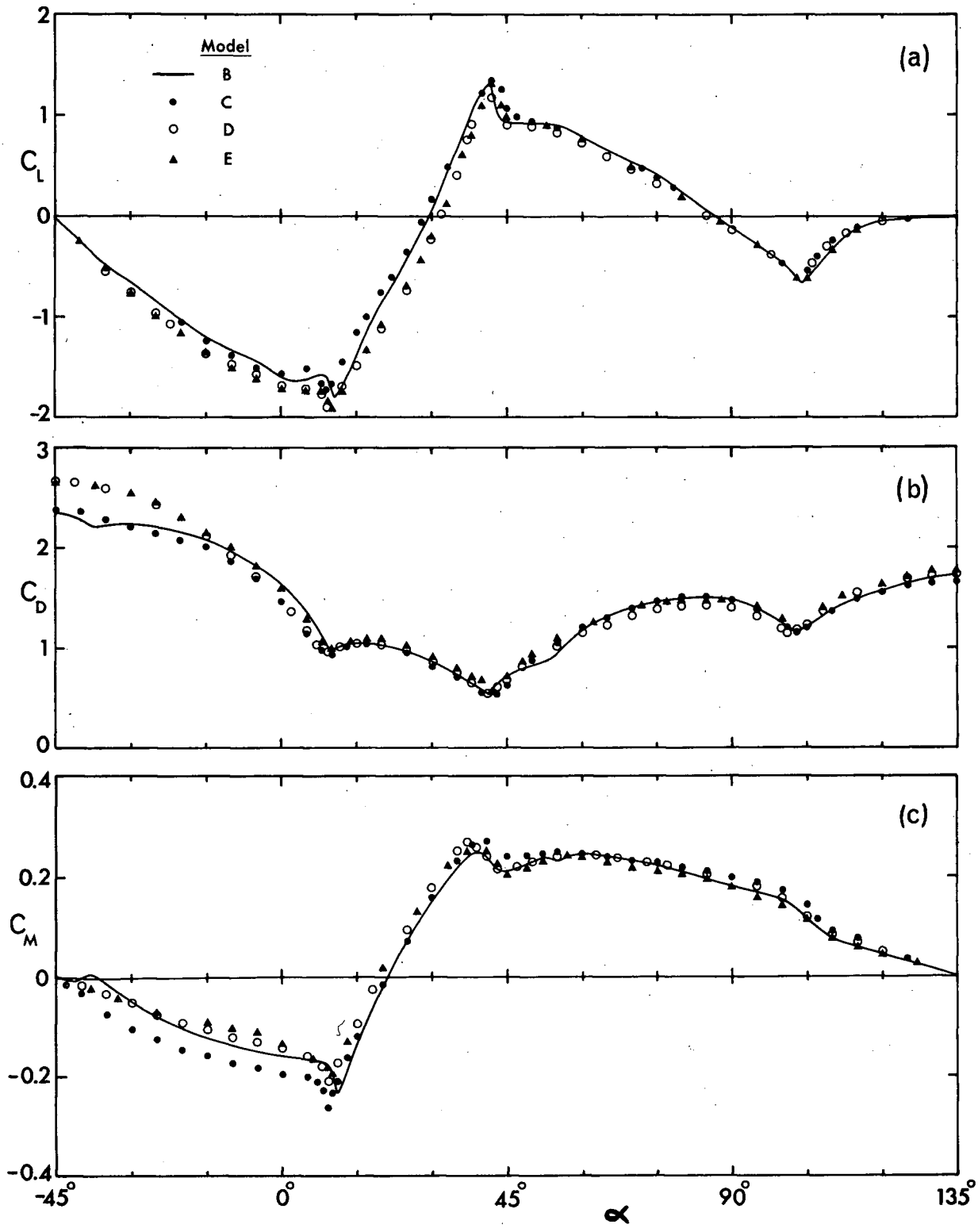

Figure 2-8 Comparison of aerodynamic coefficients for various structural angle sections

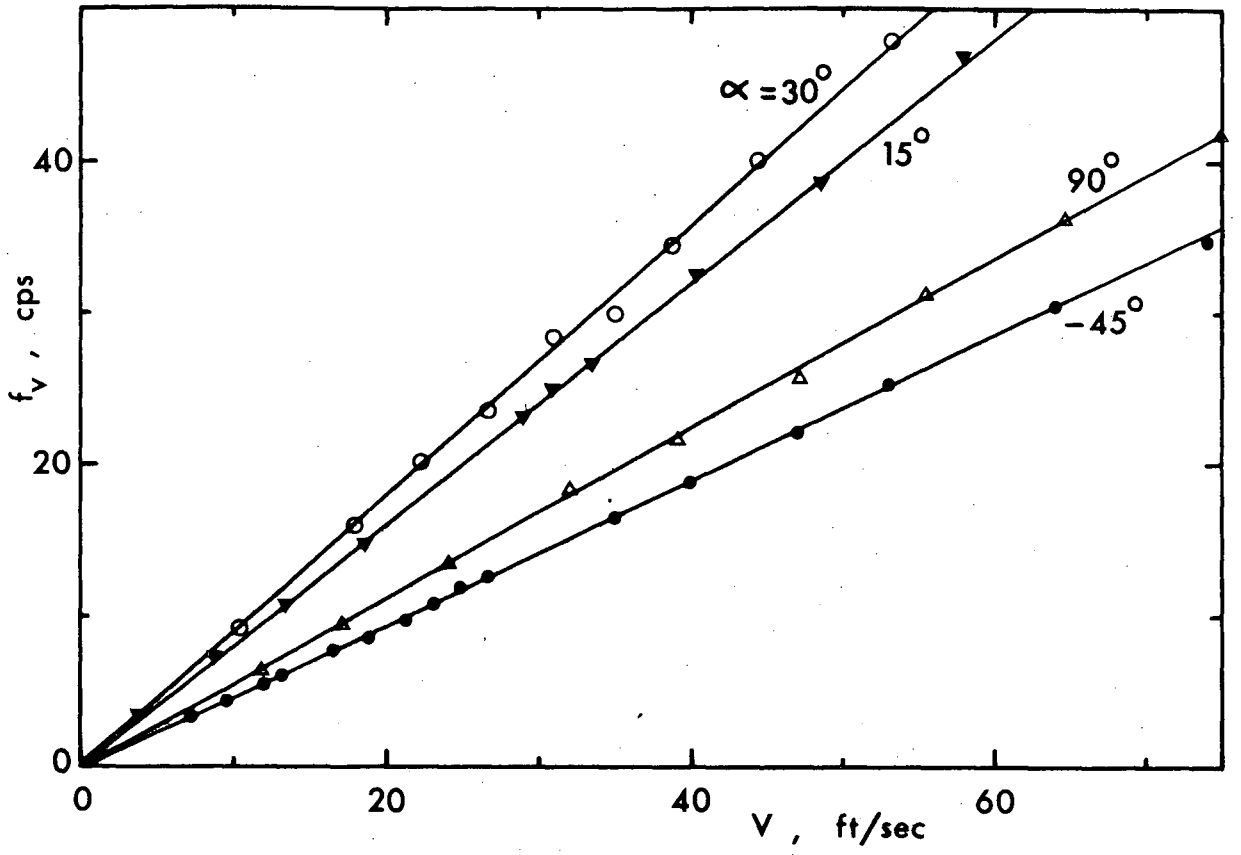

Figure 2-9 Variation of vortex shedding frequency with wind velocity for pressure tap angle model

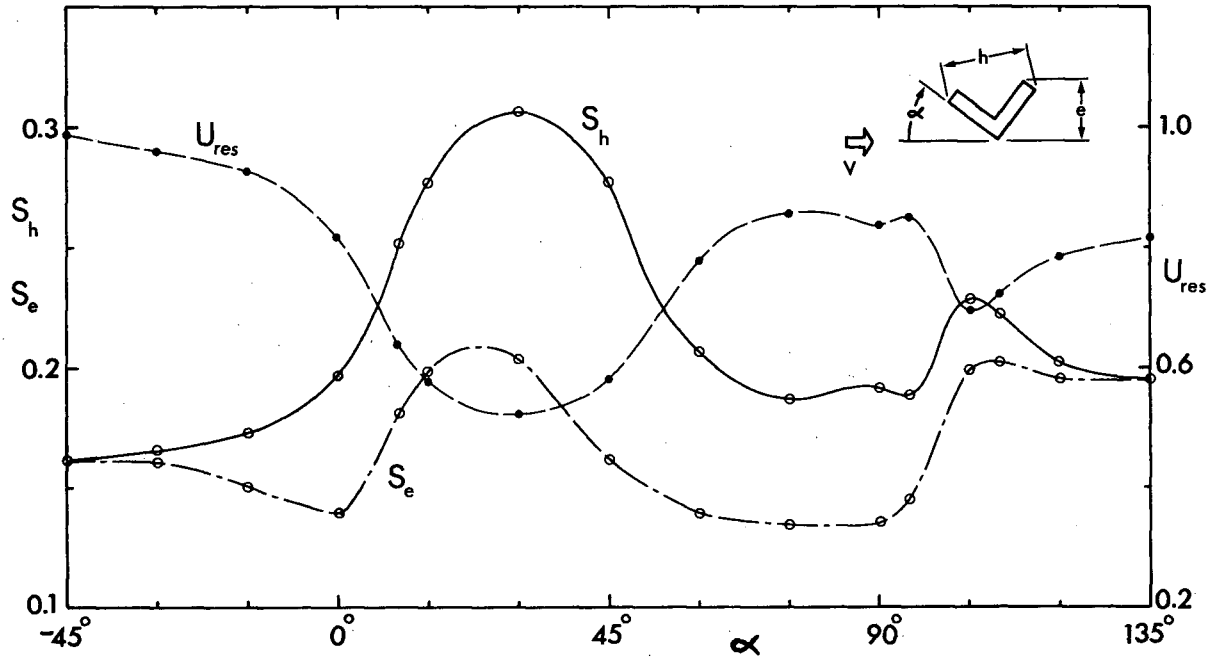

Figure 2-10 Variation of Strouhal number and vortex resonant wind speed with angle of attack for 3 in. angle model

dicates that the Strouhal number is independent of the Reynolds number over the range of 10^4 to $15x10^4$ investigated.

Using this and similar data, the Strouhal number variation with angle of attack for the pressure tap model was obtained (Figure 2-10). Basing the dimensionless frequency parameter on the projected model width e, rather than the constant dimension h, reduces the variation of Strouhal number but does not make it completely independent of orientation. The sudden increase in the Strouhal number near $\alpha = 15°$ and $105°$ is attributed to the reattachment of the flow as explained in the discussion of the balance measurements. This reduces the wake width which, in general, is accompanied by a simultaneous increase in the Strouhal frequency. Therefore, if the wake width is used as the characteristic length, the Strouhal number may have less dependency on model orientation. Roshko's[66] concept of a Universal Strouhal Number, S_*, based on wake width as well as shear layer separation velocity, has considerable merit. Examination of the mean base pressure, wake geometry and shedding frequency data indicated that the angle section will have values of S_* for various angles of attack approximately equal to the accepted result of 0.164.

A comparison of the Strouhal number distributions for the 1, 2 and 3 in. angle models tested in the same wind tunnel (Figure 2-11(a)) indicates the presence of tunnel wall interference effects. The trend is for Strouhal number to increase with blockage. For comparison, the estimated curve for free stream condition is also included (Appendix II).

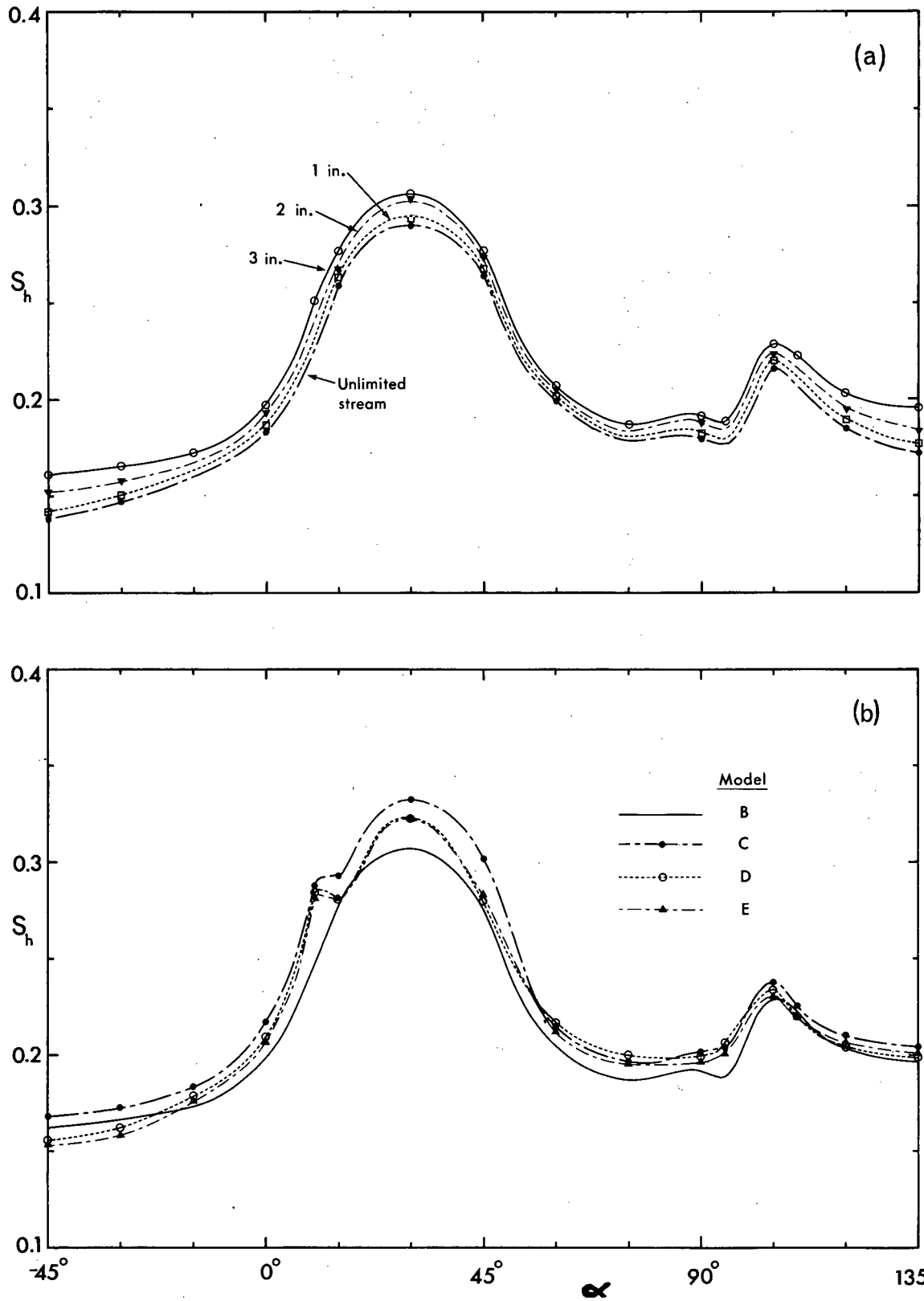

Figure 2-11 Strouhal number distributions for (a) different size angle models (b) various structural angle sections

The corresponding Strouhal number data for the balance models (B,C,D, and E) are shown in Figure 2-11(b). Aerodynamic similarity between the sharp-edged model B and the commercial angle sections is apparent. Since all the angle members are of the same nominal size, 3x3 in., the wall confinement effects would be similar. For angle sections of this width, a correction curve is presented in Appendix II, Figure II-1.

Comparison of the present Strouhal number data with the few results published by Wardlaw[2] shows good agreement. Furthermore, the angle section results follow the trend established by cylinders of different geometric form. The Strouhal numbers for several representative sections are listed below:

	S_{e_F}
(i) angle section at $\alpha = -45°$	0.135
(ii) flat plate normal to flow	0.145
(iii) 90° wedge and angle section at $\alpha = 135°$	0.18
(iv) circular cylinder	0.20
(v) flat plate at $\alpha = 40°$	0.23

The results suggest a tendency for the Strouhal number to increase in magnitude with a decrease in bluffness. Further comparison with other published data[64] provided confirmation as to the reliability of the measurements.

From the Strouhal number results, important information regarding the resonant wind speed (V_{res}), at which vortex induced aeroelastic instability may occur, can be obtained. V_{res} represents the critical wind speed at which the vortex shedding

frequency coincides with the natural frequency of the system. Expressed in nondimensional form, the resonant wind speed can be obtained from the Strouhal number using the expression

$$U_{res} = \frac{1}{2\pi S_h} \tag{2.2}$$

Shown in Figure 2-10 is the variation of U_{res} with α for the 3 in. angle section. It is apparent that an angle member is susceptible to vortex resonance at the lowest velocity near $\alpha = 30°$.

2.4.3 Mean Static Pressure Distributions

The mean static pressure on the surface of the angle model was found to be independent of the Reynolds number over the range 10^4 to 12×10^4. The pressure distribution around the model midspan section is shown in Figure 2-12, for various angles of attack. The results indicate the location of the stagnation and separation points. In addition, the curves provide data on the base pressure coefficient which is useful in the evaluation of the separated shear layer velocity and wind tunnel wall correction. For the same orientations, investigation of the spanwise C_p distribution showed it to be relatively constant, thus substantiating two-dimensionality of the flow.

A comparison of the pressure integrated and balance measured aerodynamic coefficients (Figure 2-13) confirms the above observation. As shown, both lift and drag coefficients are in good agreement over the entire range of angle of attack. The pitching moment measurements show similar trend except for the

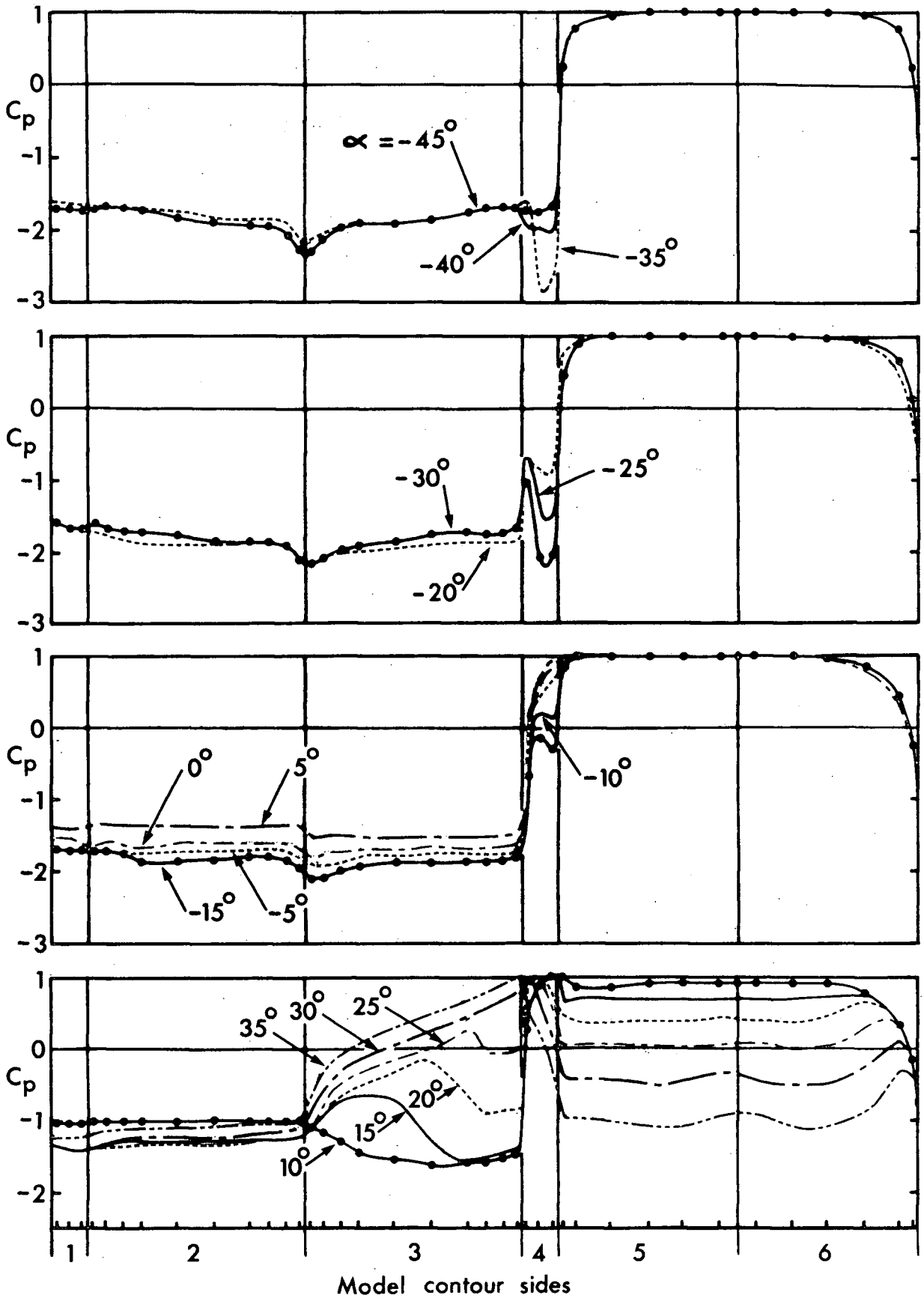

Figure 2-12-i Midspan distributions of mean static pressure coefficient ($-45° \leq \alpha \leq 35°$)

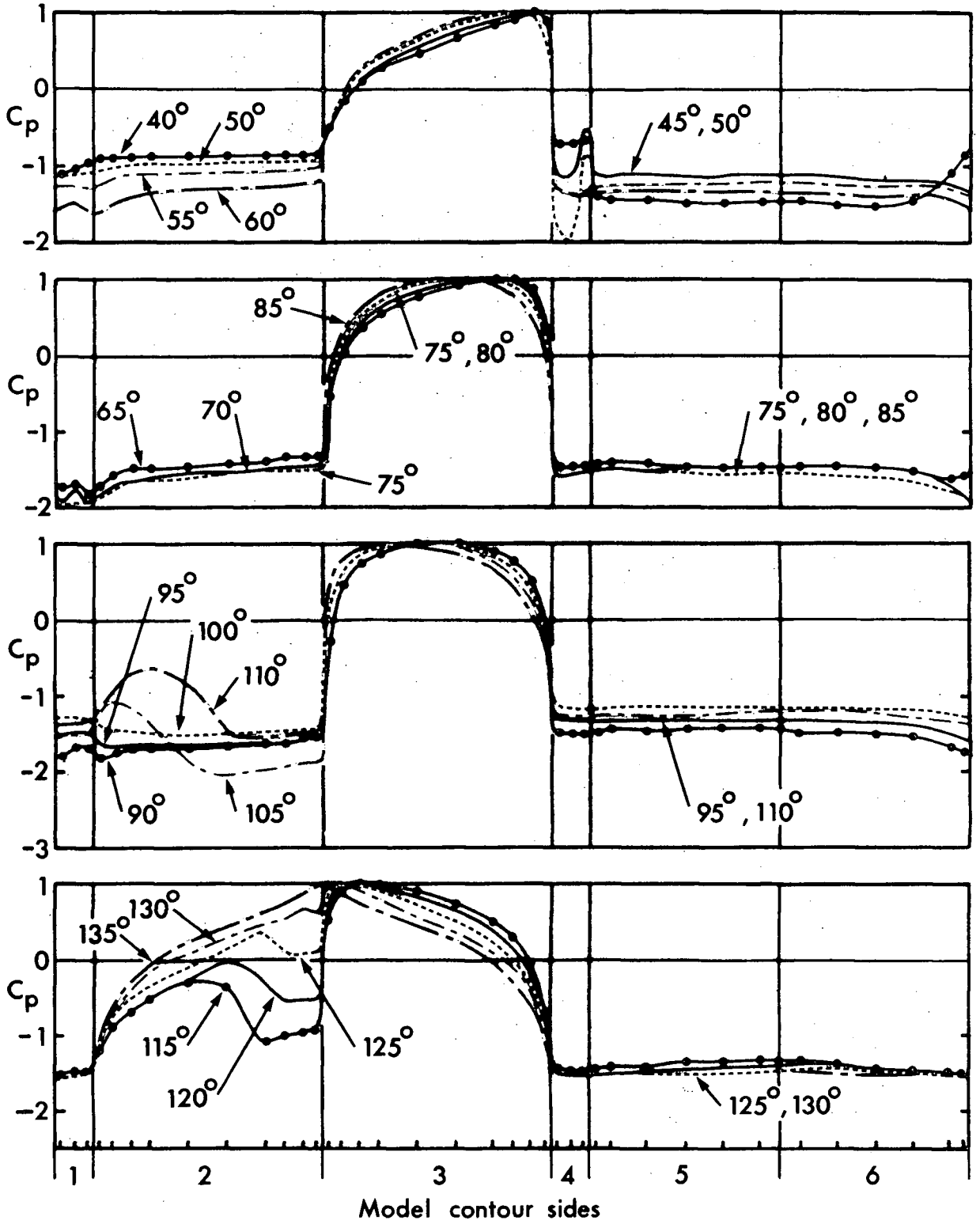

Figure 2-12-ii Midspan distributions of mean static pressure coefficient ($40° \leq \alpha \leq 135°$)

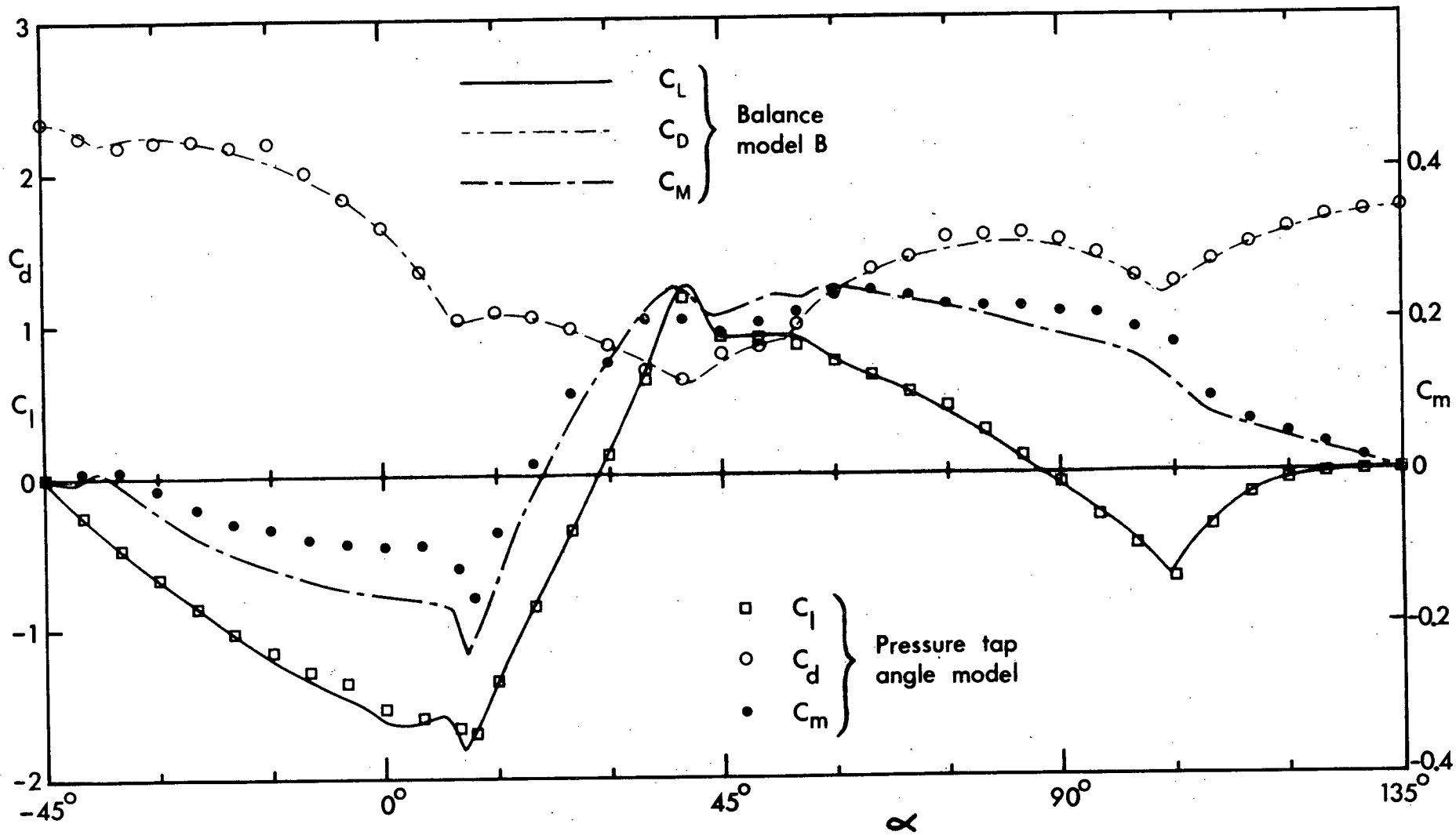

Figure 2-13 Comparison of pressure integrated and balance measured steady aerodynamic coefficients

discrepancy in magnitude over the range $\alpha = \pm 25°$.

2.4.4 Fluctuating Static Pressure Distributions

Oscilloscope traces of typical fluctuating pressure signals from various model taps are illustrated in Figure 2-14. The photographs in (a) show the amplitude modulation of pressures from two midspan and two spanwise taps. The typical phase signals shown in (b) were obtained from various pressure taps as follows:

(i) neighbouring midspan taps from the same side of the model;

(ii) midspan taps from opposite sides of the model;

(iii) spanwise taps from the same side of the model.

Over the range of 26×10^3 to 63×10^3, it was observed that the Reynolds number did not have any significant effect on the average fluctuating pressure coefficient or phase angle.

For various angles of attack, the midspan distributions of the average fluctuating pressure coefficient and modulation ratio are illustrated in Figure 2-15. It is apparent that the amplitude of the fluctuating pressure can reach a magnitude comparable to the mean static pressure level. The maximum $C_{\bar{p}}$ values are of the order of 0.8 in the vicinity of $\alpha = -45°$ and 75° with corresponding modulation ratios between 1.5 and 2.5. At angles of attack of 45° and 135°, the average coefficient diminishes to a level below 0.2 but the modulation ratio remains at approximately 2.0. This variation of fluctuating pressure with model orientation was observed qualitatively as well during the flow visualization experiment by noting the change in the strength of the vortex wake system.

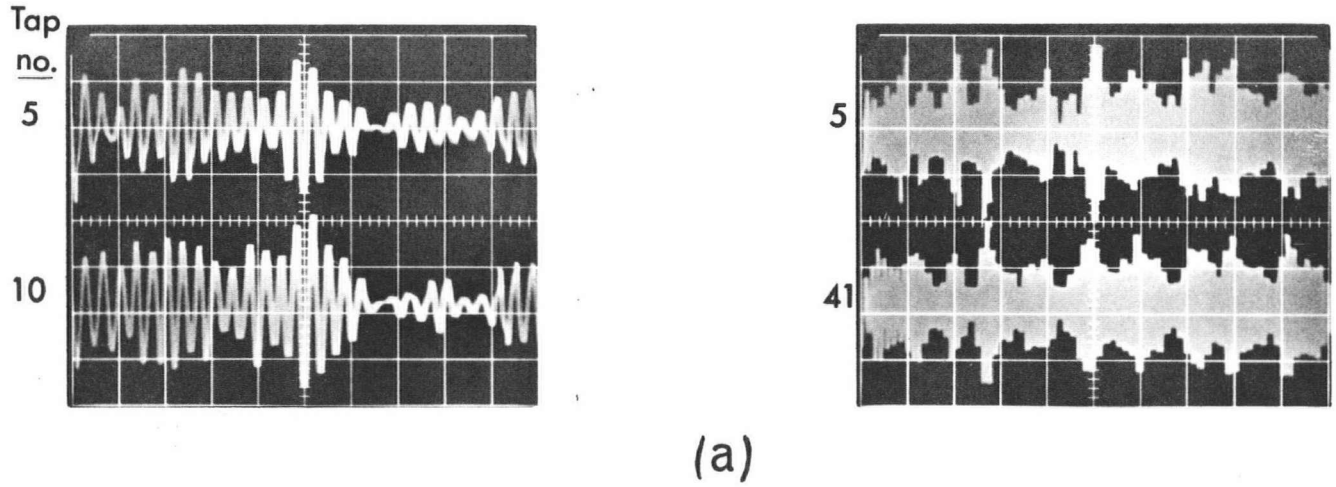

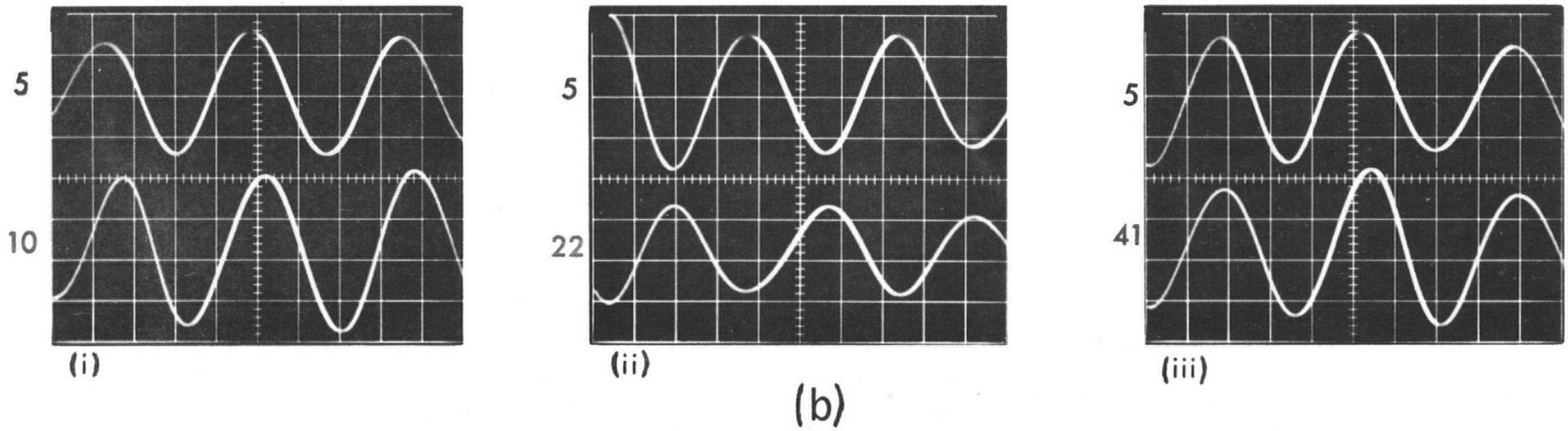

Figure 2-14 Typical fluctuating pressure signals from various model taps indicating (a) random amplitude modulation (b) phase variation

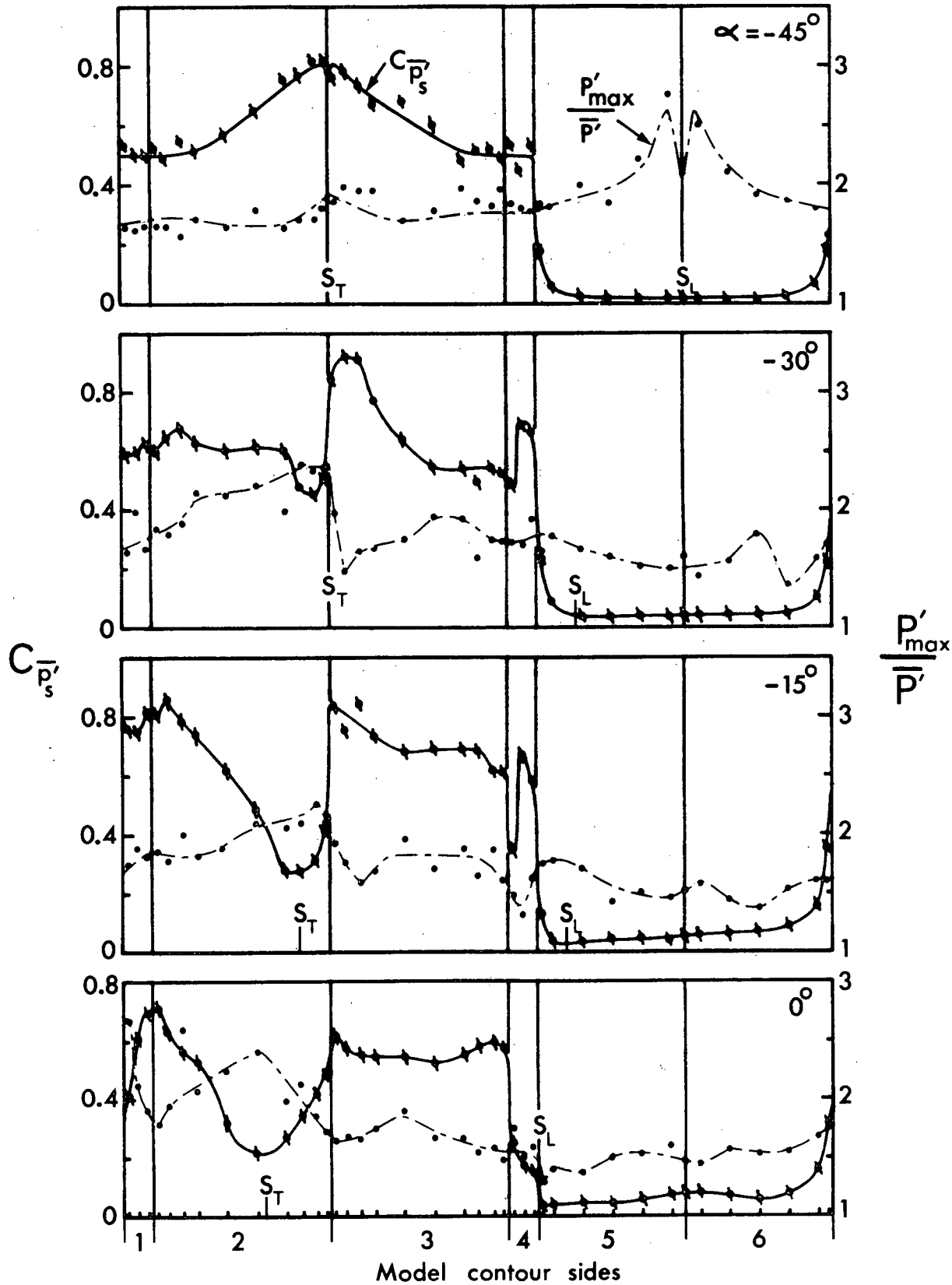

Figure 2-15-i Midspan distributions of fluctuating static pressure coefficient and amplitude modulation ratio ($-45° \leq \alpha \leq 0°$)

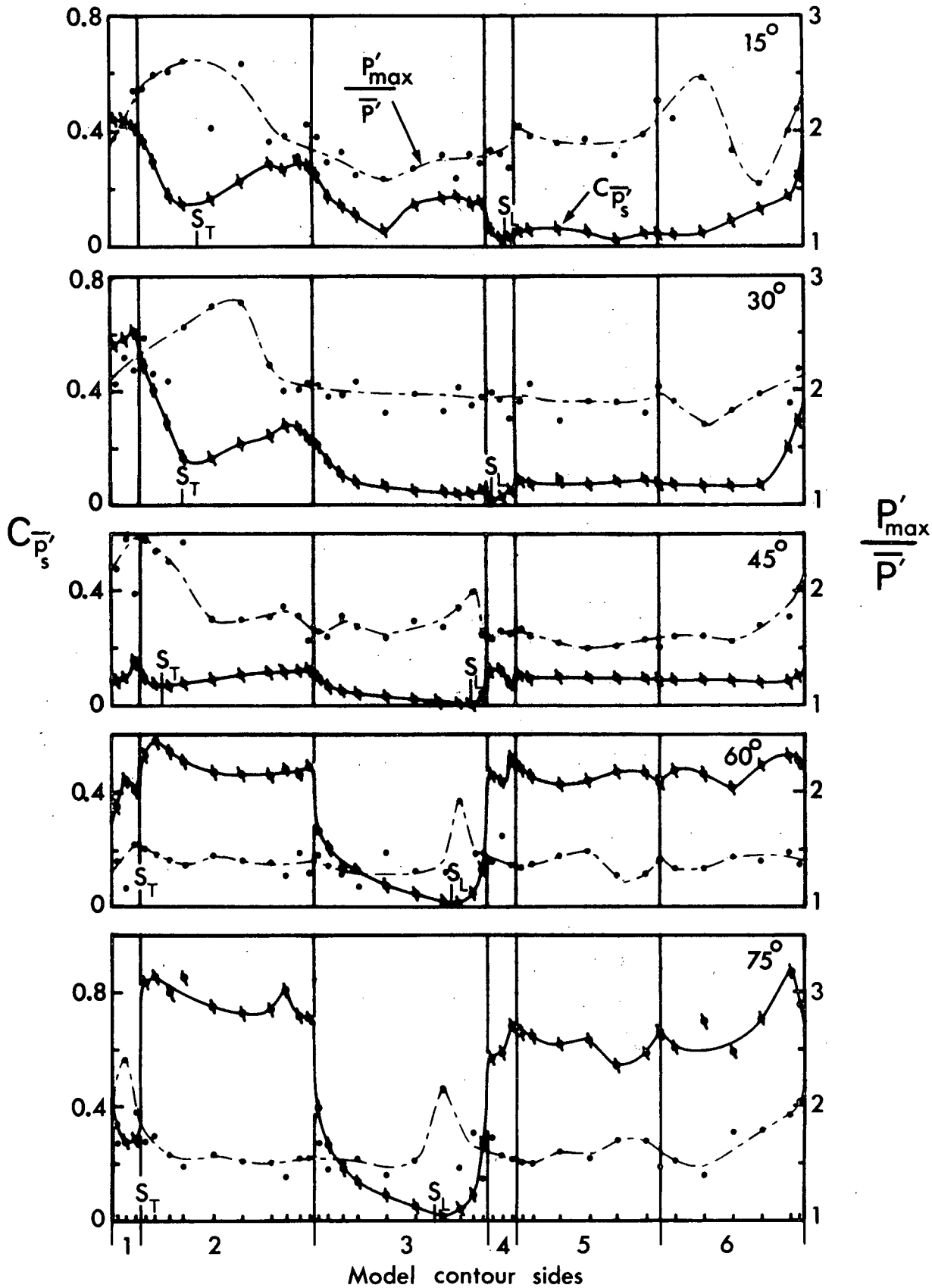

Figure 2-15-ii Midspan distributions of fluctuating static pressure coefficient and amplitude modulation ratio ($15° \leq \alpha \leq 75°$)

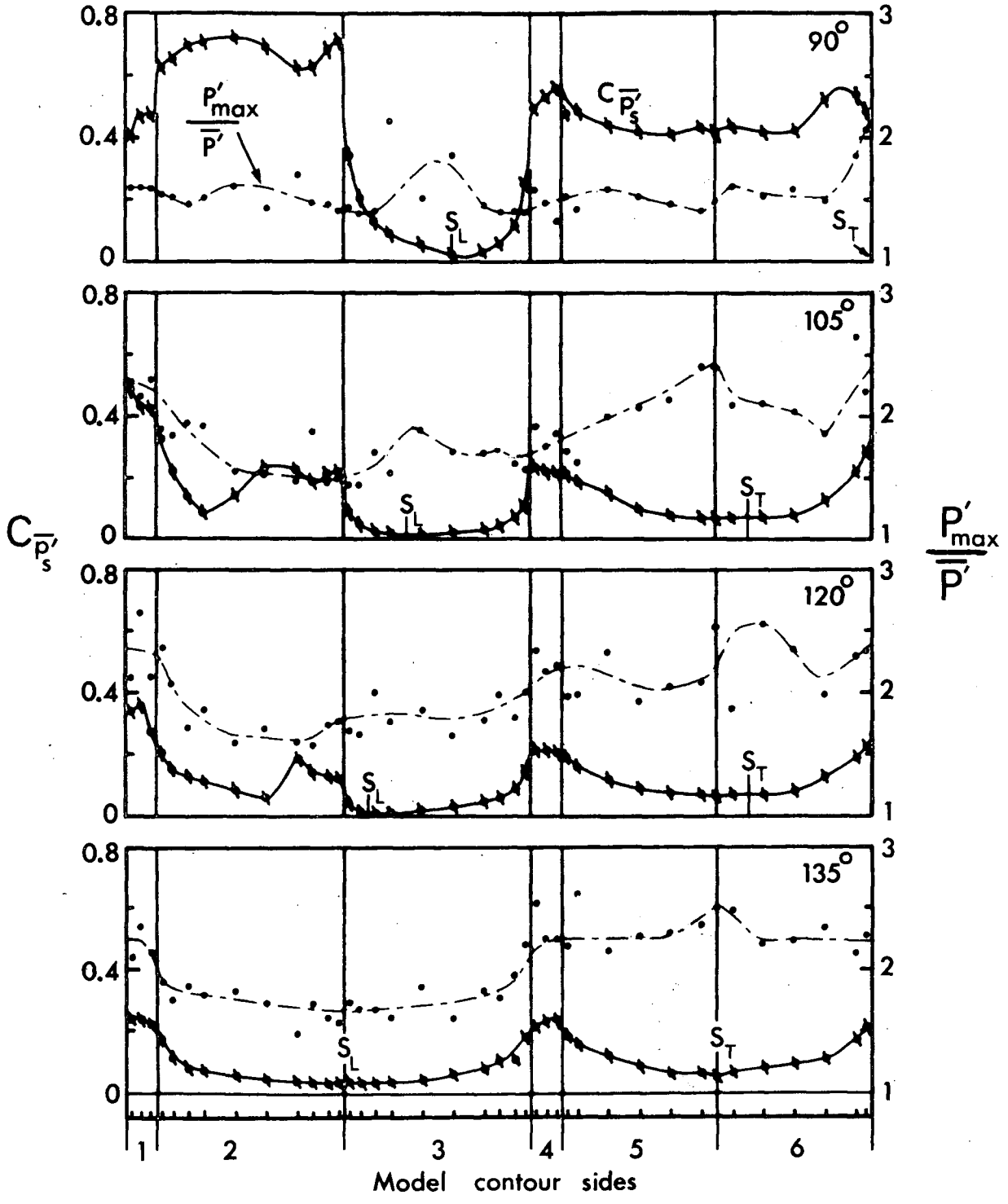

Figure 2-15-iii Midspan distributions of fluctuating static pressure coefficient and amplitude modulation ratio ($90° \leq \alpha \leq 135°$)

For the portion of the body in the wake, the magnitude of the fluctuating pressure is comparatively larger than that near the forward stagnation point, S_L. A similar reduction in $C_{\bar{p}'}$ occurs in the vicinity of the rear "stagnation" region marked S_T. It seems reasonable that this tendency of vanishing $C_{\bar{p}'}$ near the two stagnation areas is due to the cancellation of the pressure fluctuations, from the two sides of the wake system, which are 180° out of phase. However, this effect is less complete at the rear of the body because of irregularities in the wake. Quantitative observations indicated the second harmonic component of the pressure fluctuations to be less than 20% of the fundamental frequency value.

The seemingly random amplitude modulation of the pressure fluctuations is attributed to the general instability of the separated shear layers and associated vortices. Much of the vorticity generated at the body is dissipated immediately behind the cylinder through turbulence. Even the vortices, forming the Kármán vortex street, are of different strengths and tend to lose their individuality as the distance behind the body increases.

From the sample phase data in Figure 2-14, it is observed that the pressure fluctuations on opposite sides of the model contour exhibit the familiar 180° phase difference. On the other hand, pressure signals from neighbouring taps on the same side are not necessarily in phase as frequently reported in literature, but may have phase differences as large as 50° to 100° (Figure 2-16). These phase variations are attributed to the adjustment of the flow field around the model due to the shedding of a vortex downstream and formation of the next vortex core. Recent measure-

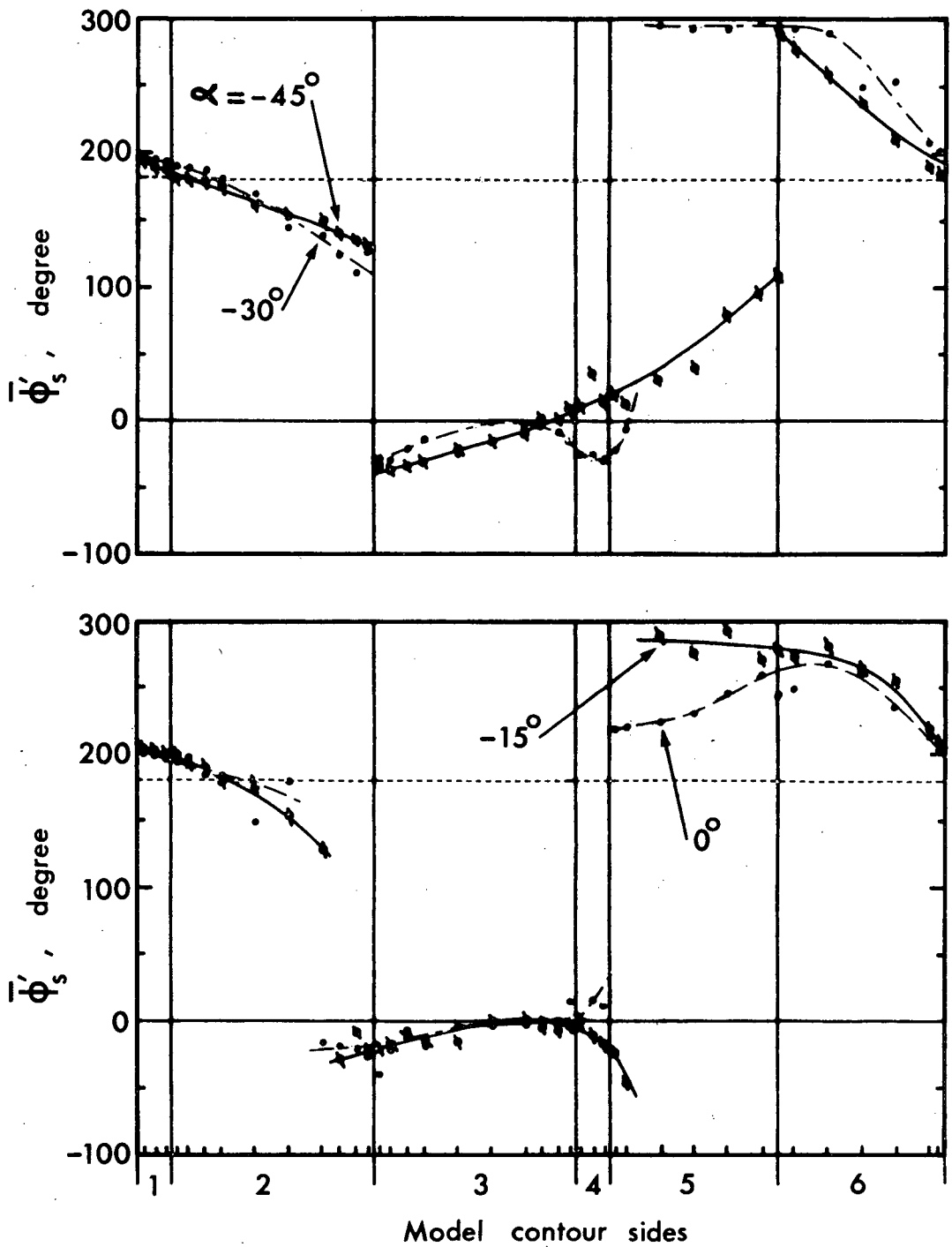

Figure 2-16-i Phase variation of midspan fluctuating pressure ($-45° \leq \alpha \leq 0°$)

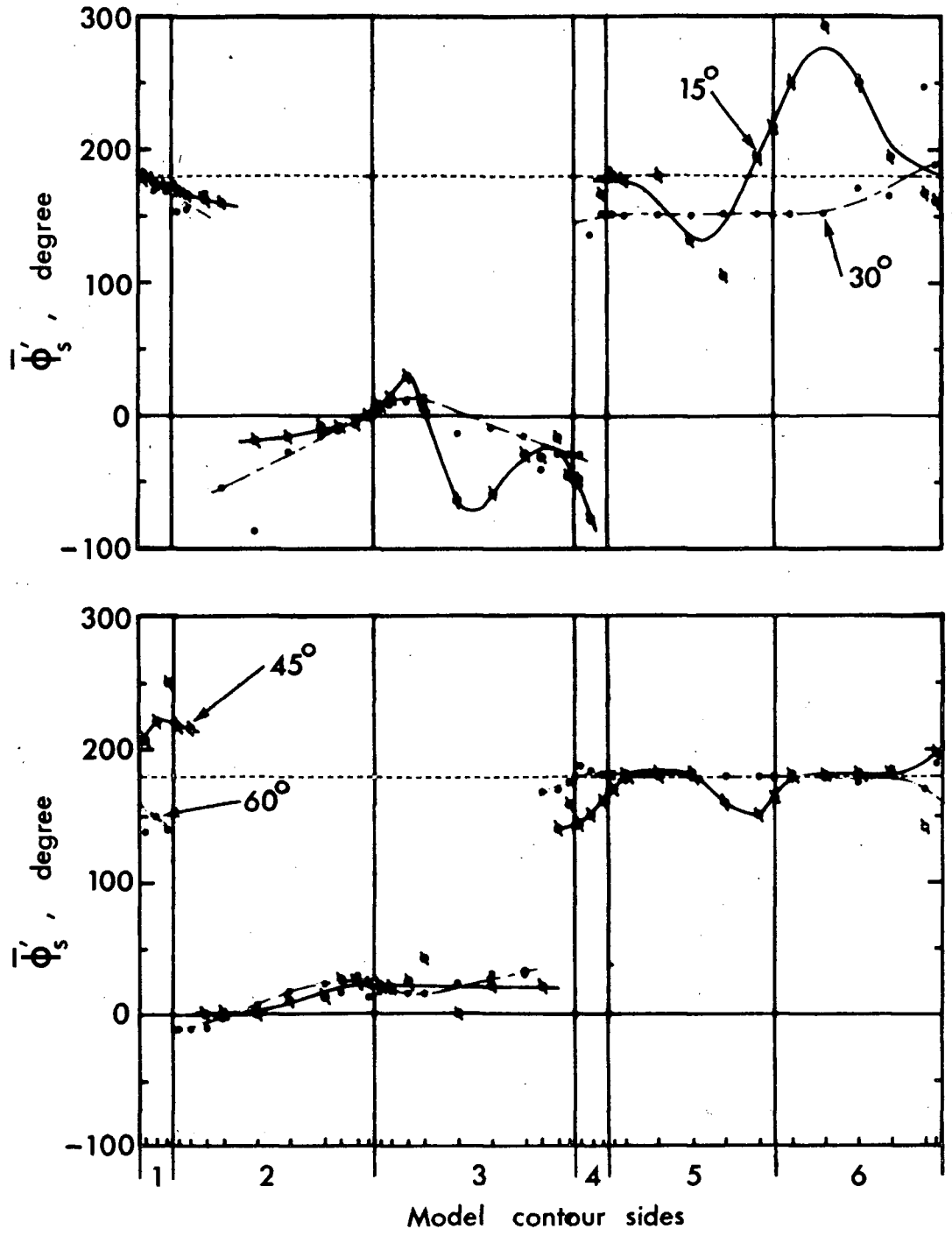

Figure 2-16-ii Phase variation of midspan fluctuating pressure ($-15° \leq \alpha \leq 60°$)

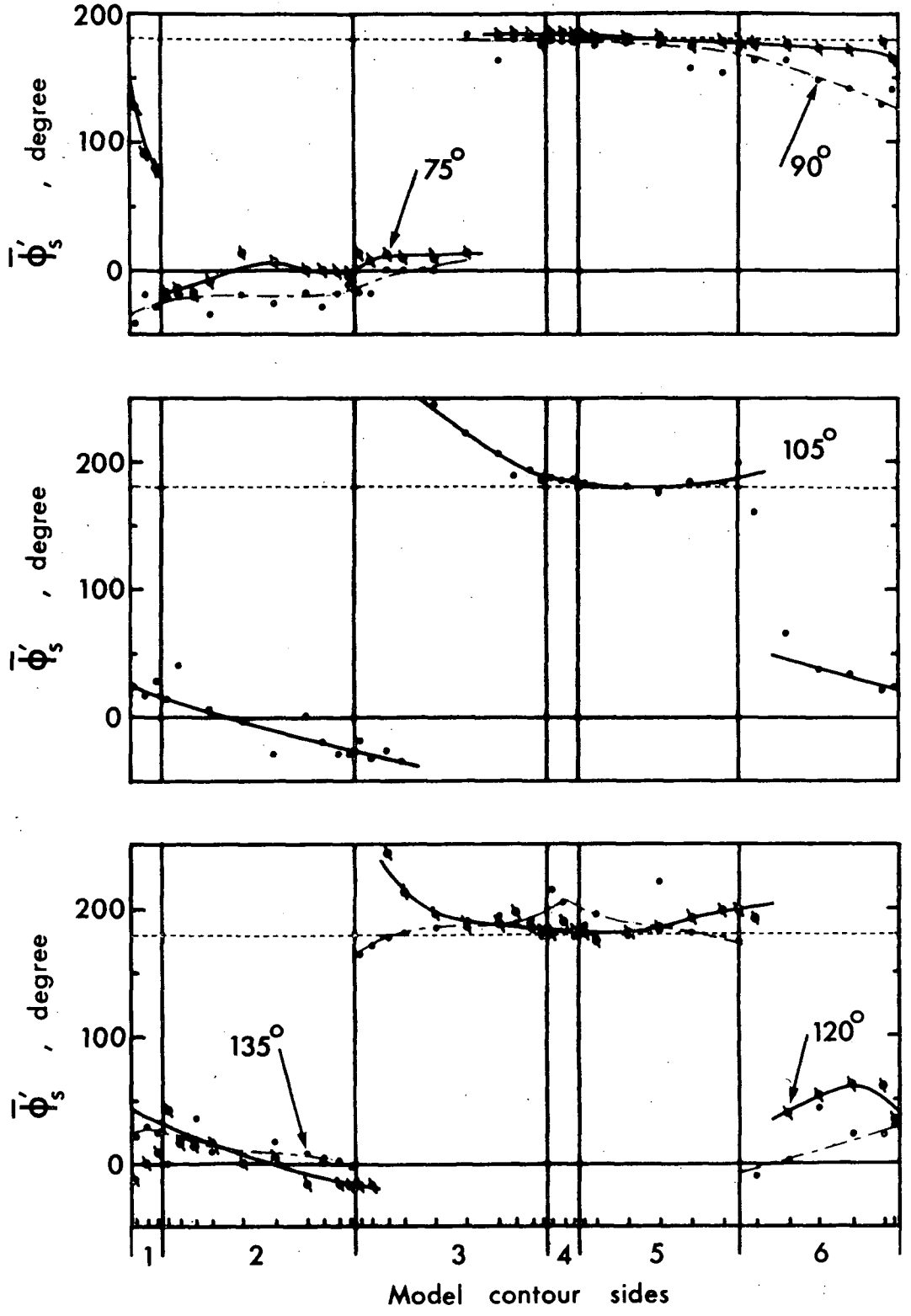

Figure 2-16-iii Phase variation of midspan fluctuating pressure ($75° \leq \alpha \leq 135°$)

ments by Wiland[35] on elliptic cylinders indicated a similar phase phenomenon.

The spanwise variations of the fluctuating pressure, shown in Figure 2-17, suggest reasonably uniform pressure coefficient along the model length. However, the scatter and inconsistency in phase data, particularly at some angles of attack, are too large to establish any definite trend. It seems reasonable to assume on the basis of the work reported by Vickery,[40] Prendergast[46] and Feng[47] that spanwise correlation of the flow exists over only a finite length of the model. For stationary circular cylinders the correlation length is typically of the order of two to three cylinder diameters with increased two-dimensionality during cylinder motion. As reported by Vickery, the correlation length improves for sharp-edged bodies and is of the order of five to six diameters for a stationary square member in a smooth stream. However, under turbulent flow conditions, the spanwise correlation suffers substantial reduction. As illustrated in Figure 2-14(a), the amplitude modulations of the pressure fluctuations on the stationary angle model are in phase around the contour and along the length of the model. Similar observations have been reported by other investigators.[31,33,35]

2.4.5 Fluctuating Lift, Drag and Moment Coefficients

The midspan fluctuating pressure distribution was integrated numerically to obtain the fluctuating lift, drag and pitching moment experienced by the stationary angle section (Figure 2-18). The pitching moment is about the c.g. axis. Two data points are plotted for each coefficient to indicate the effect of the measured phase difference at the midspan taps. Both calculations, however, take into account the 180° phase between the

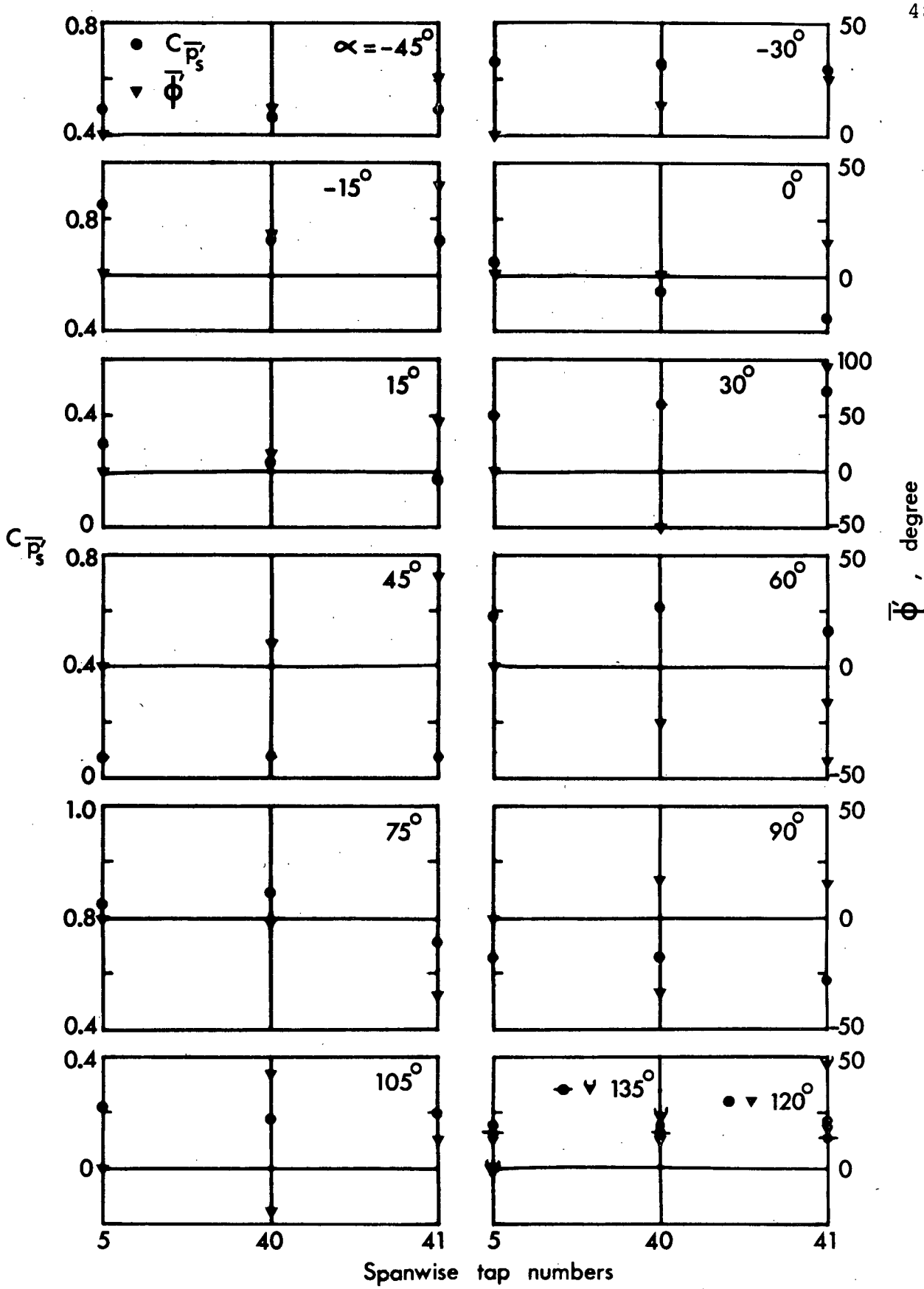

Figure 2-17 Spanwise variation of fluctuating pressure coefficient and phase

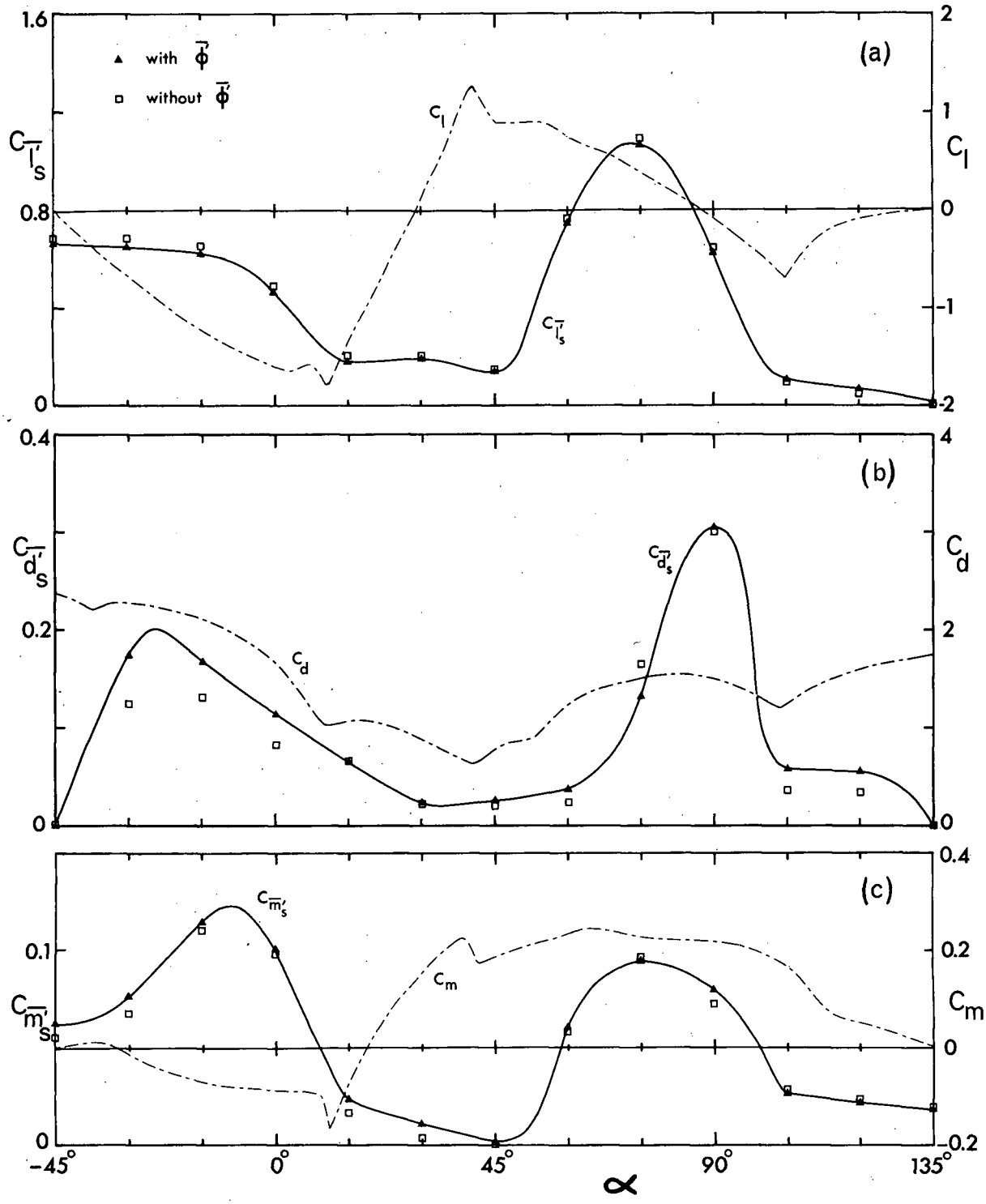

Figure 2-18 Comparison of fluctuating and steady aerodynamic coefficients

fluctuating pressures from the two sides of the model. Since the research programme was not aimed at studying the spanwise variations, this effect is not included in the above results. For comparison, the distributions of the static sectional coefficients from Figure 2-13 are included.

Examination of the fluctuating forces and moment coefficients indicates that:

(i) $C_{\bar{l}_s}$ is of the same order as C_l;

(ii) $C_{\bar{d}_s}$ is approximately 1/10 of C_d;

(iii) $C_{\bar{m}_s}$ is about 1/2 of C_m.

The fluctuating aerodynamic coefficients show large variation with model orientation reaching minimum values near $\alpha = 45°$ and 135°. This trend was also suggested by the fluctuating pressure distributions. In general, the effect of the phase is to change the above coefficients by less than ±10%. Thus, accurate determination of the phase angle along the sides of the model contour is less significant in the final evaluation of the coefficients. Study of the fluctuating pressure amplitude and phase distributions at each angle of attack reveals that the large phase differences occur over regions with near minimum $C_{\bar{p}}$ values, thus contributing little to the final summation.

2.4.6 Wake Geometry

Using the techniques described in section 2.3.5, wake geometry data was obtained for the 1 in. dynamic and 3 in. pressure tap models. All tests were performed at $N_R = 59{,}500$ except for one additional examination of the lateral vortex

spacing for the pressure tap angle model at N_R = 26,800 with α = 135°. Within the range of Reynolds number investigated, no significant change in wake geometry was observed.

Figure 2-19 shows the lateral variations of the fluctuating pressure amplitude at various x-stations for two typical angles of attack. As expected, the fluctuating pressure distributions are similar on both sides of the wake for symmetrically oriented models. The wake centreline is then coincident with the x-axis. However, for the models at other angles of attack the wake is unsymmetrical with the peaks of the pressure curves higher on the side for which the point of separation is most rearward. The experimental results by Fage and Johansen[67] showed that vorticity is shed from the upper and lower surfaces of an asymmetric model at the same rate. Therefore, the presence of the higher pressure peaks on one side of the wake may be explained by the fact that the corresponding vortex travels relatively shorter distance and hence suffers less dissipation and dispersion.

From lateral pressure distribution results, similar to those in Figure 2-19, the decay of the peak pressure amplitude in the downstream direction was obtained as shown in Figure 2-20. The curves indicate an approximate inverse proportionality between pressure and downstream distance which agrees with the analytical prediction given by Schaefer and Eskinazi's[68] vortex street model. Experimental measurements with circular and elliptic cylinders by Ferguson[33] and Wiland,[35] respectively, indicate similar pressure decay curves.

Taking the peaks of the lateral pressure distributions as the positions of the two vortex rows, Figure 2-21 shows the stream-

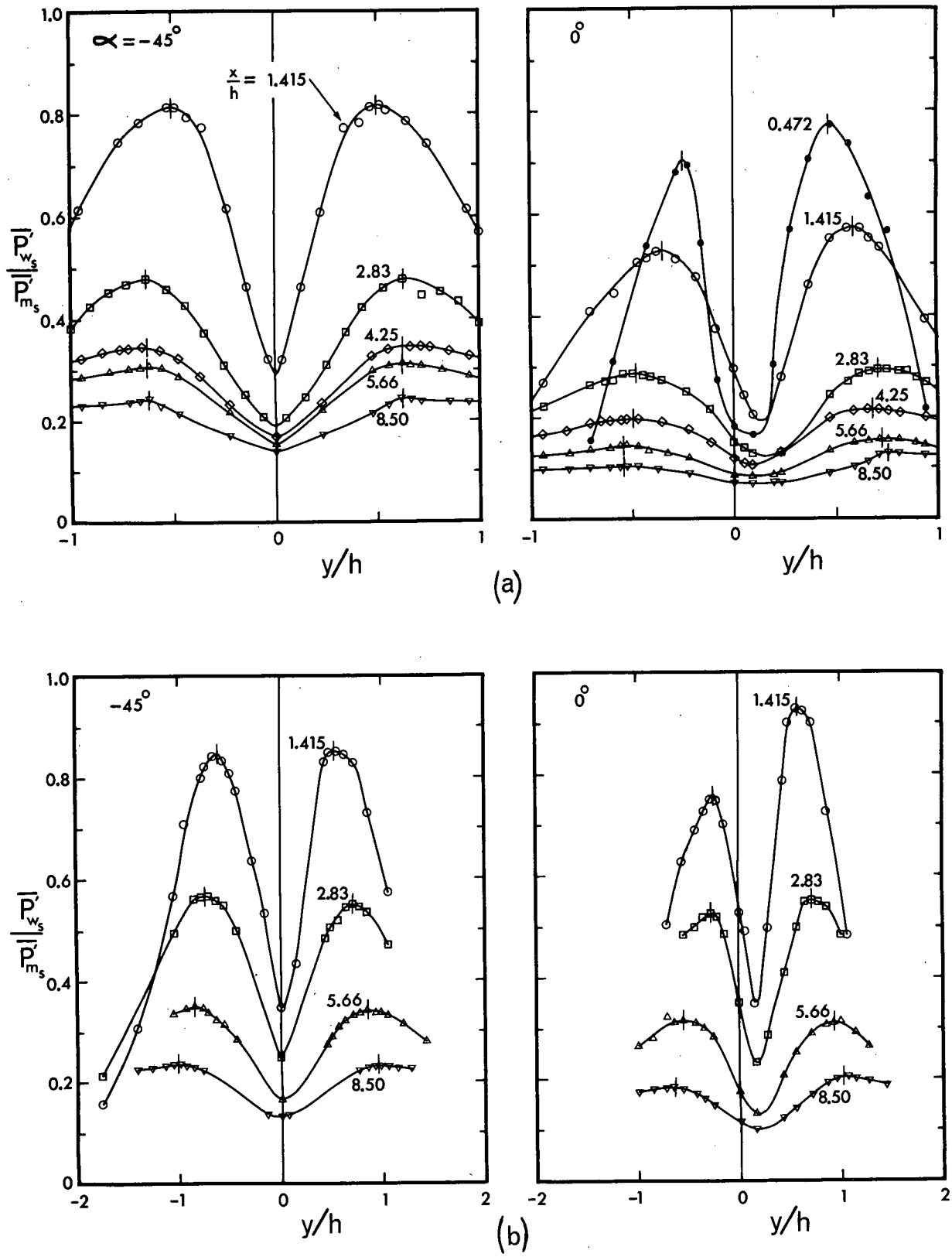

Figure 2-19 Lateral variation of fluctuating pressure amplitude in the wake of (a) 3 in. angle model (b) 1 in. angle model

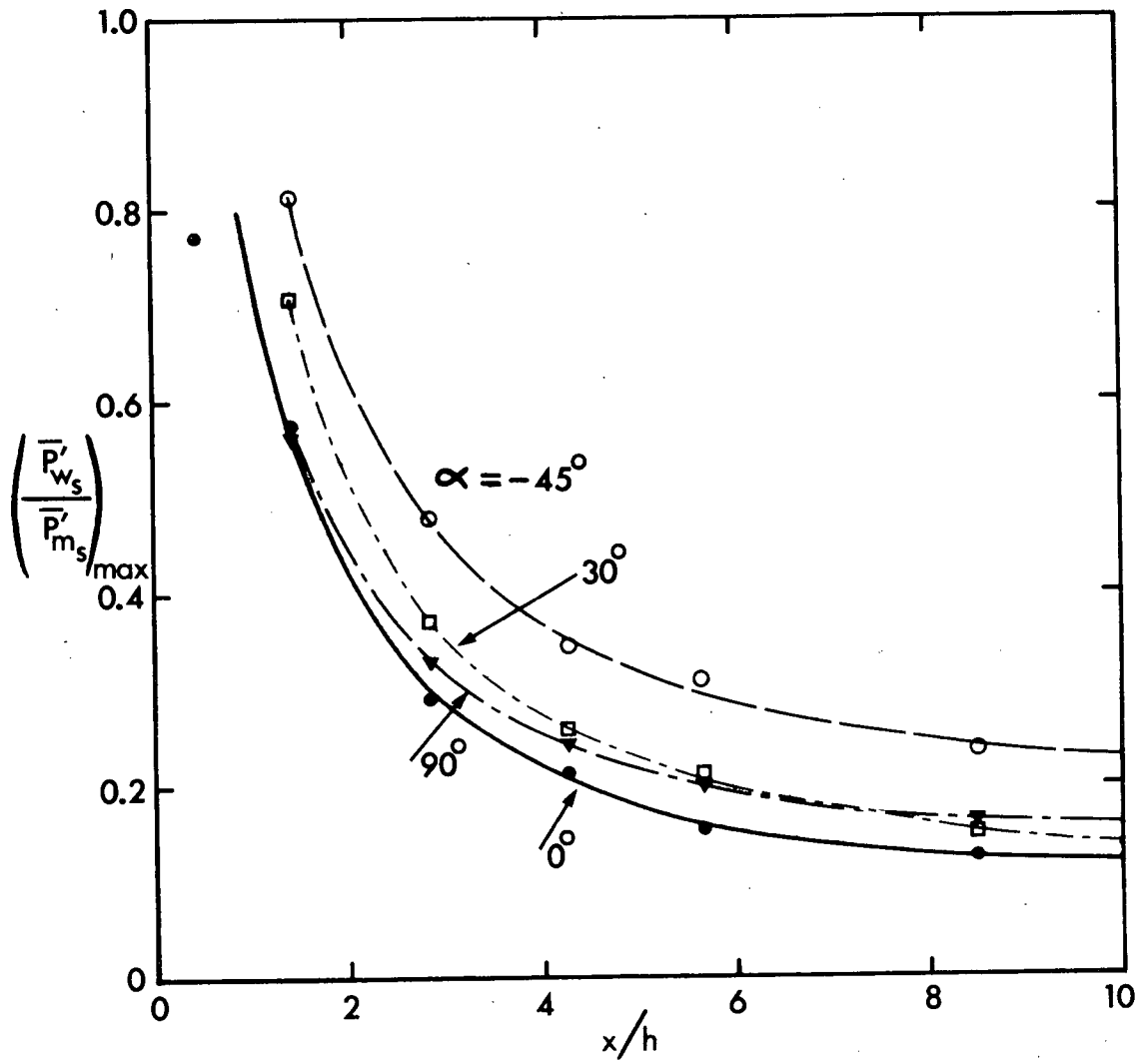

Figure 2-20 Variation of peak fluctuating pressure with downstream coordinate

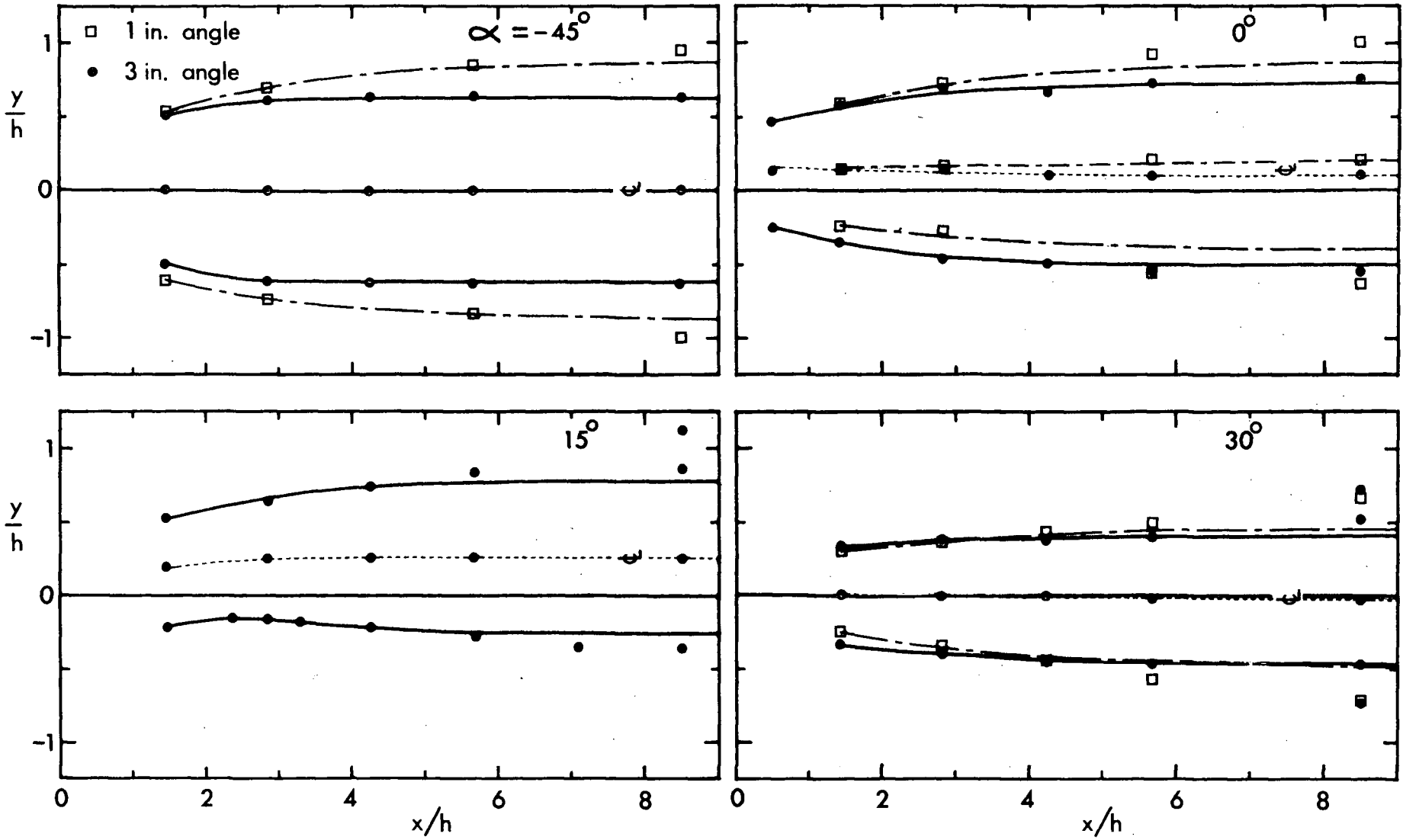

Figure 2-21-i Lateral position of vortex rows behind 1 in. and 3 in. angle models ($-45° \leq \alpha \leq 30°$)

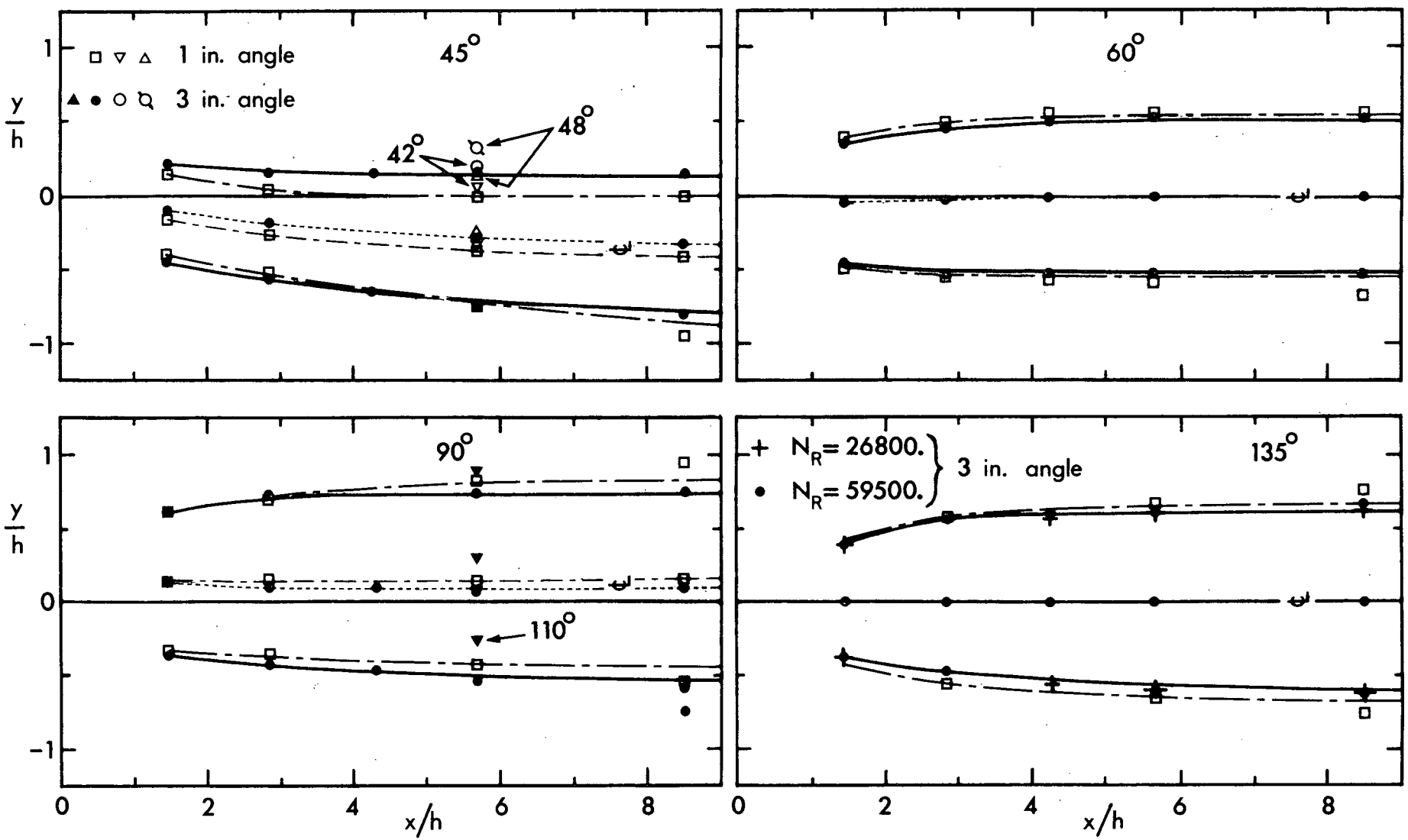

Figure 2-21-ii Lateral positions of vortex rows behind 1 in. and 3 in. angle models ($45° \leq \alpha \leq 135°$)

wise variation of the wake data for both the 1 in. and 3 in. angle models at various angles of attack. However, as pointed out by Hooker[69] the maximum velocity fluctuations and, therefore, pressure fluctuations, do not occur along the path of the vortex centres as some experimenters have asserted but rather develop in the neighbourhood of the edge of the core farthest from the street centreline. Hence, the actual positions of the vortex centres lie inward of the pressure boundaries by an amount equal to the radius of the vortex cores. Using the mathematical model of an isolated viscous vortex, Schaefer and Eskinazi were able to arrive at an expression for correcting the experimental measurements. For the angle models, this gives a correction which increases with x from virtually zero at the model to less than 4% at a distance of $x/h = 10$. It is apparent, however, that at large x/h this correction is not adequate as it does not account for turbulence or wake instability which may influence the expansion of the vortex cores or the position of their centres. This observation is in agreement with the experimental measurements[70,71] which show that the vortices do not flow downstream indefinitely in parallel rows but always move away from the centreline with increasing x even when an intermediate sequence of vortices have some uniformity of configuration.

From Figure 2-21, the distribution of the transverse separation of the vortex rows is plotted in Figure 2-22 for the 1 in. and 3 in. models. The increase of the lateral spacing in the downstream direction, tending to some uniform value, is indicated. It is shown that the parameter b/h is also dependent on model orientation.

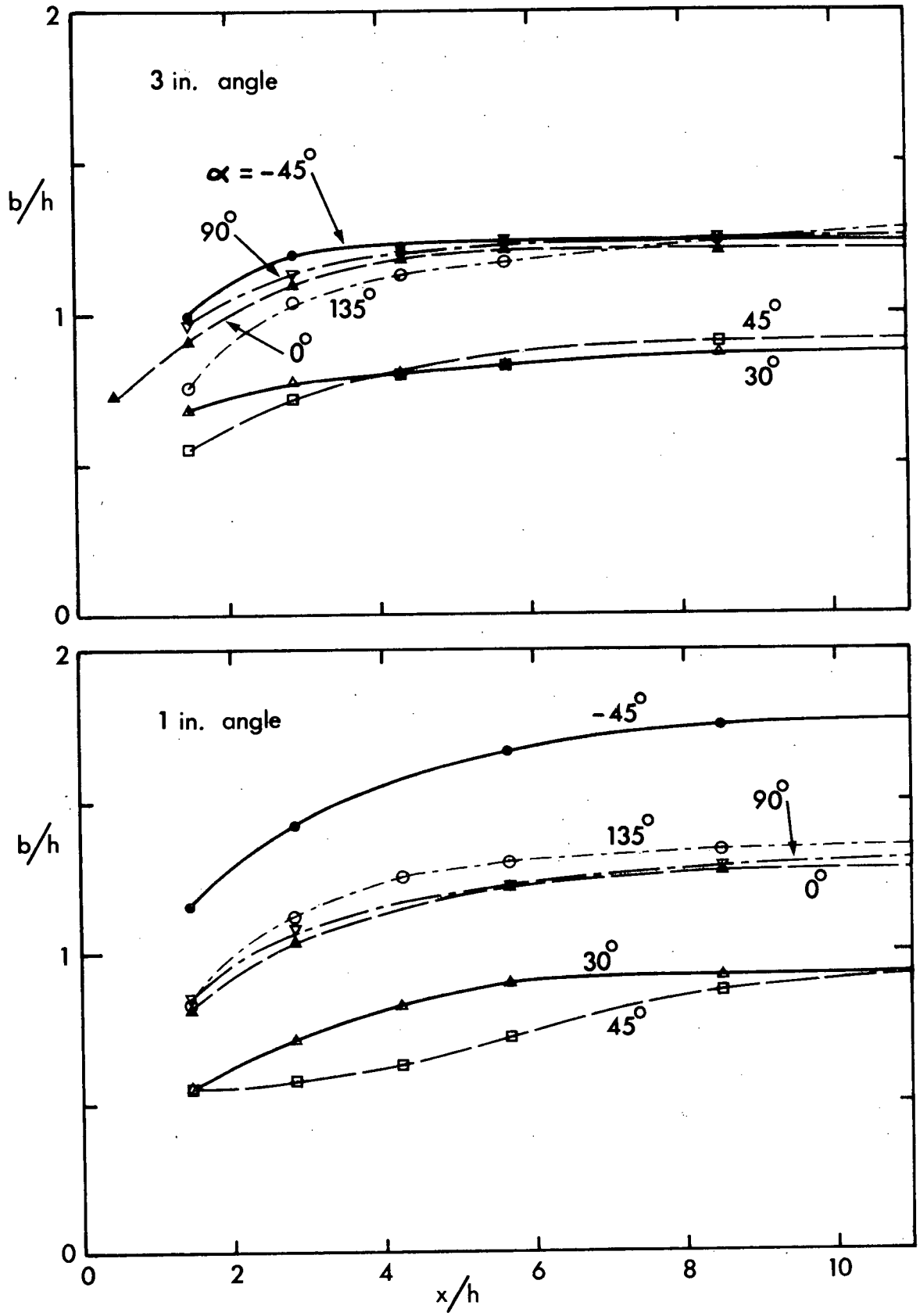

Figure 2-22 Variation of lateral vortex spacing for 1 in. and 3 in. angle models

From the results, it is apparent that wind tunnel interference effects do exist, as indicated by the relative confinement of the wake for the larger model. A discussion of wall influence on wake geometry is presented in Appendix II.

Results on phase angle distribution in the wake for the pressure tap model are presented in Figure 2-23. The longitudinal phase variation appears to become linear far downstream indicating that the vortices have reached a uniform streaming velocity and, thereby, constant longitudinal spacing. The limited length of the tunnel test section and clarity of the fluctuating pressure signals restricted the longitudinal measurements to $x/h \doteq 13$. Using the fact that a phase difference of 360° exists between the fluctuating pressure signals associated with consecutive vortices in one row, the corresponding longitudinal spacing was obtained as shown in Figure 2-24(a). The curves indicate that the spacing of the vortices increases rapidly behind the body and approaches a constant value at large x/h. It is apparent that the parameter a/h is also a function of angle of attack. The dimensionless vortex velocity curves shown in Figure 2-24(b) exhibit a similar trend as the longitudinal spacing since the two variables are directly related by the Strouhal number [equation(2.1)].

Combining Figures 2-22 and 2-24(a), distribution of the classical wake geometry parameter, b/a, for both models at various angles of attack, is summarized in Figure 2-25. With increasing x, the general trend is for b/a to reach a maximum in the vicinity of $x/h \doteq 2.5$ and then decrease quite rapidly to attain some limiting value. According to Kármán,[6] b/a should

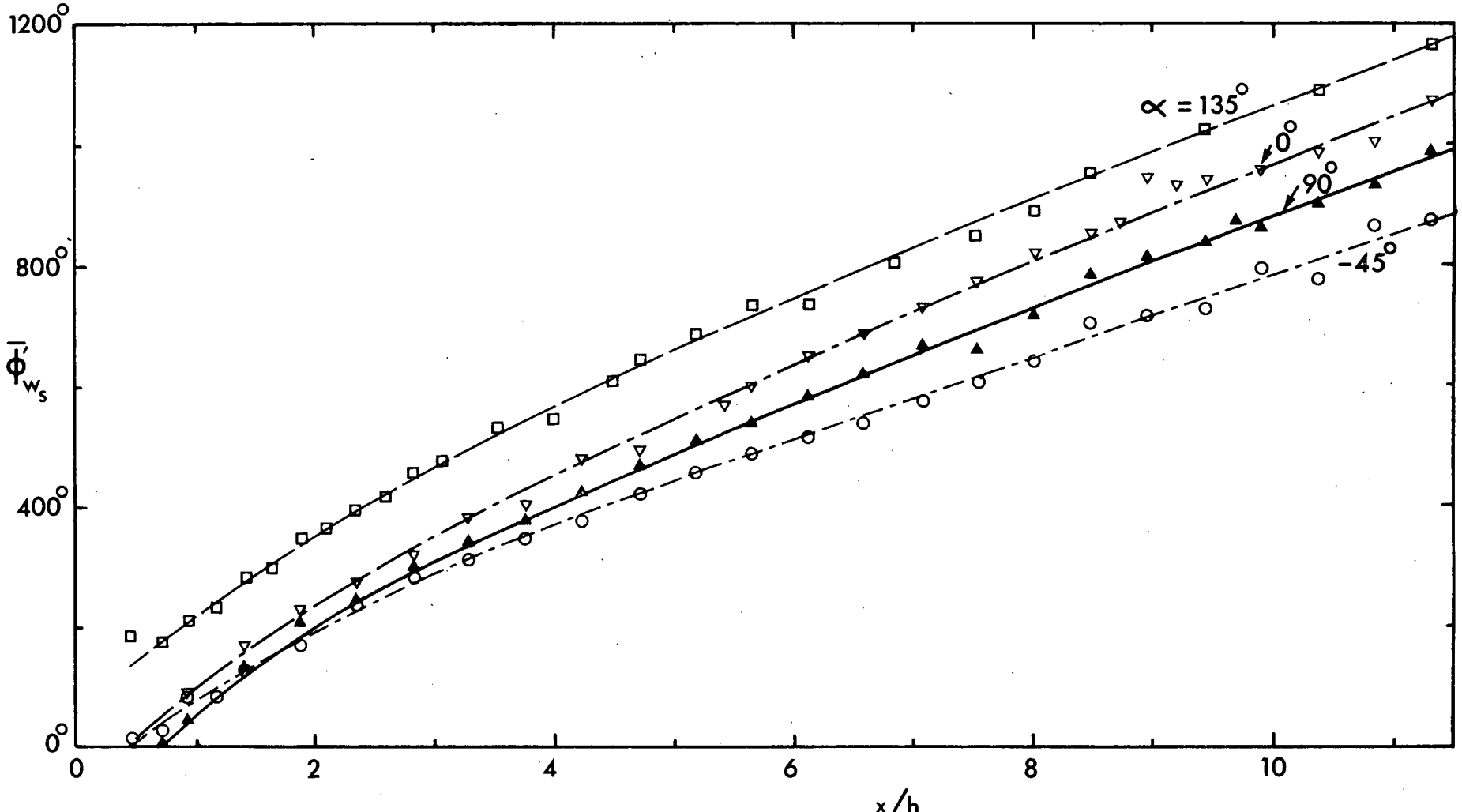

Figure 2-23 Longitudinal variation of phase angle in wake of stationary 3 in. angle model

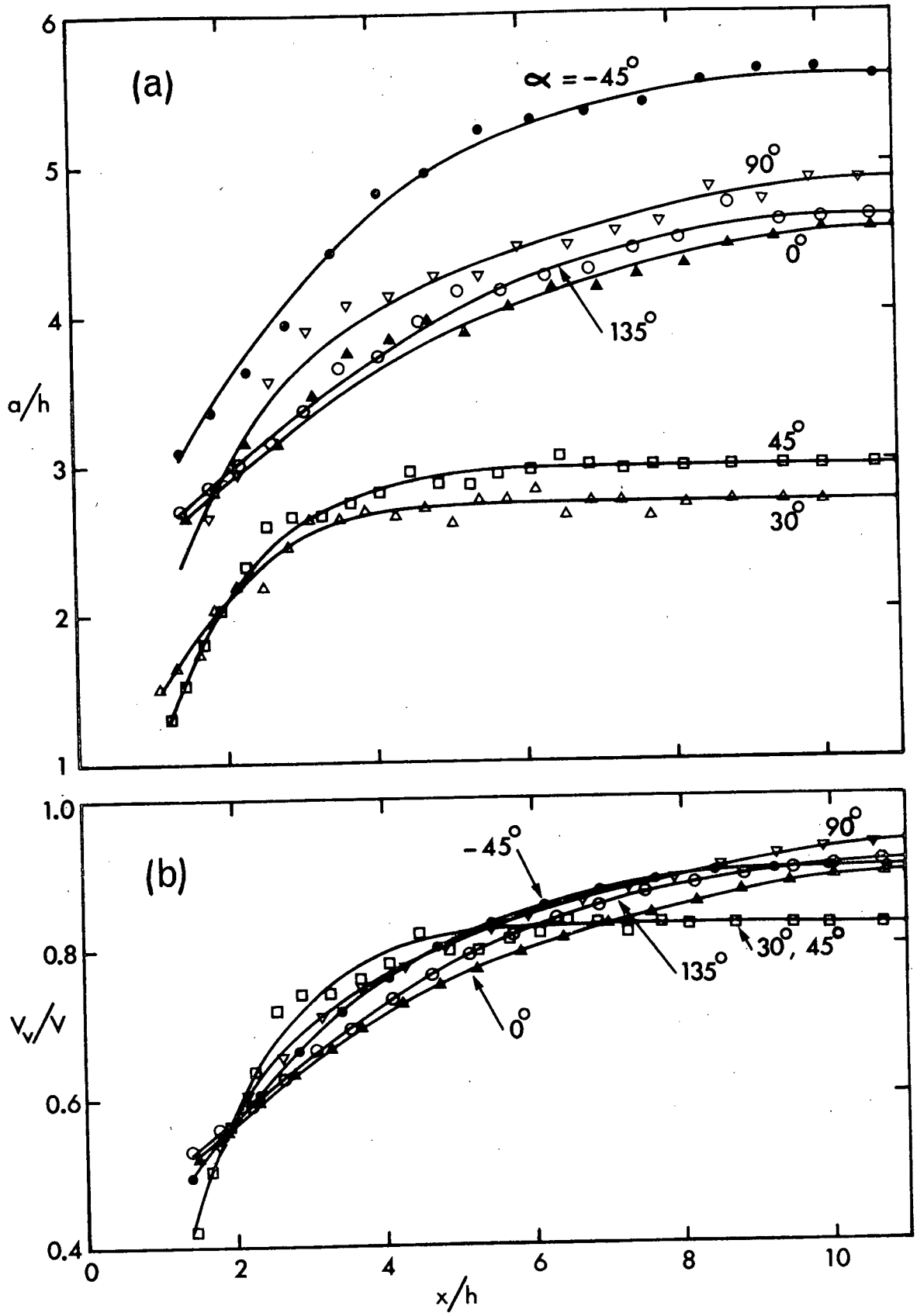

Figure 2-24 Streamwise variation of (a) longitudinal vortex spacing (b) vortex velocity

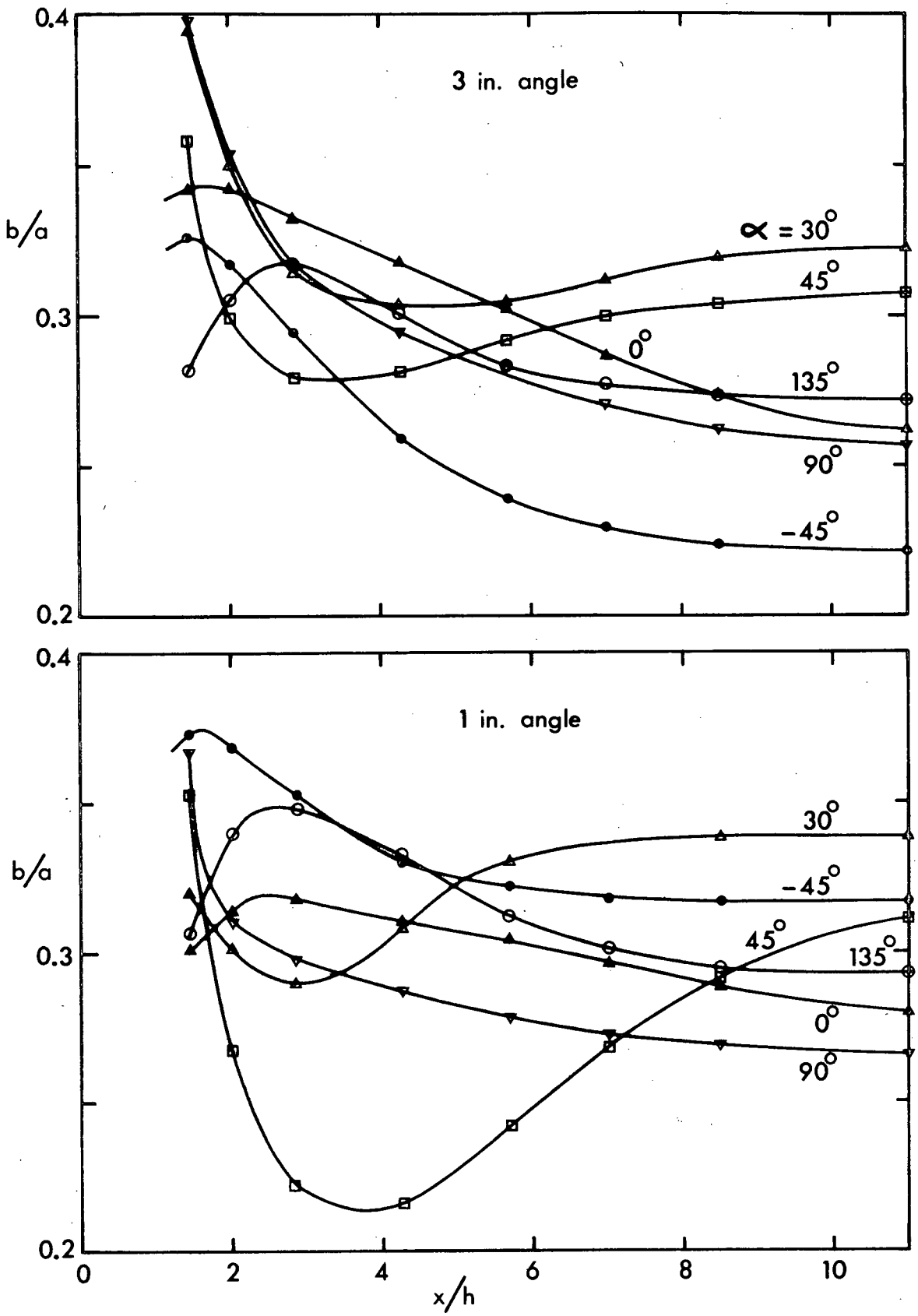

Figure 2-25 Longitudinal distributions of wake geometry ratio for 1 in. and 3 in. angle models

be approximately equal to 0.36 behind the obstacle and then diminish with downstream distance to the classical value of 0.281. However, for some orientations of the angle model an increase in b/a with x was observed. Bénard[5] as well has presented data indicating a similar reversal of the trend.

The constant values of the wake geometry variables at large distances downstream of the model, referred to as "near infinity," are plotted in Figure 2-26. The graphs clearly indicate the dependence of wake geometry on model orientation. Two curves for each of the lateral and longitudinal spacings are shown with either the maximum or projected height of the model as the non-dimensionalizing length. Note that the use of e does not significantly reduce the variation of the wake parameter with angle of attack. It is of interest to observe that the distribution of $(b/a)_\infty$ is in the vicinity of Kármán's stability value of 0.281.

Wake geometry data for an angle section have not been reported in literature. However, numerous publications on wake characteristics behind obstacles of simpler shape are available and have been listed in Table 2-1. The results for the angle model at $\alpha = -45°$ have reasonable similarity with the flat plate characteristics, and the data at $\alpha = 135°$ compares with that for a circular cylinder. However, such similarity between the bodies cannot be generalized due to the complex geometry of the angle section.

As a final summary of the experimental results for the stationary angle section, a comparison of the Strouhal number, wake geometry and drag coefficient variations with model orientation are presented in Figure 2-27. It is interesting to note

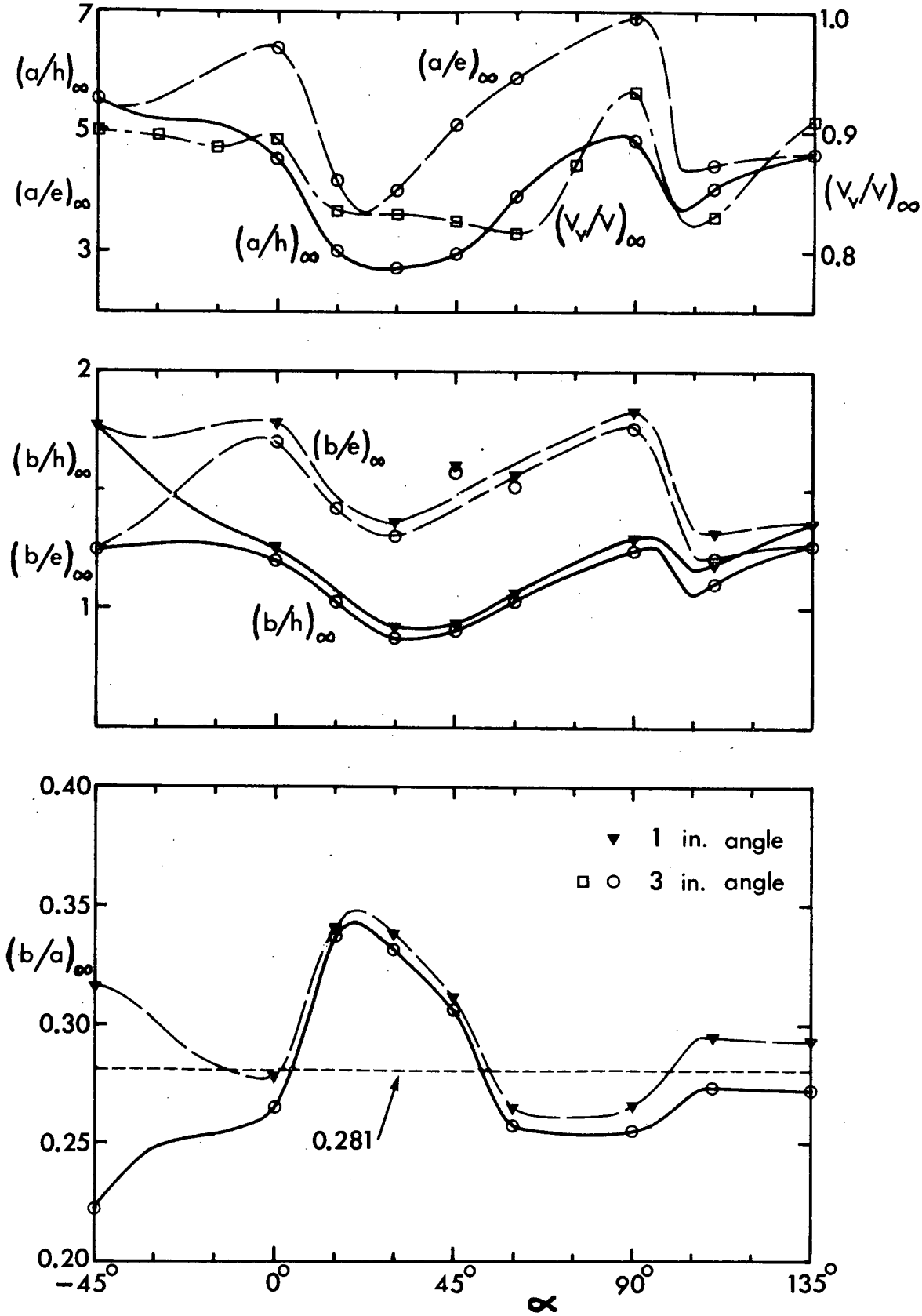

Figure 2-26 Distributions of the 'near infinity' values of the wake survey parameters for 1 in. and 3 in. angle models

TABLE 2-1

Wake Geometry Parameters for Various Bodies

body	investigator	$(a/e)_\infty$	$(b/e)_\infty$	$(b/a)_\infty$	$(u/V)_\infty$	$(V_v/V)_\infty$
circular cylinder	Bénard (E)	4.68-6.43		0.15-0.49 average≐0.32		
	Kármán (E)	4.3	1.2	0.28	0.14	
	Fage and Johansen (E)	4.27		0.23		0.80
	Rosenhead and Schwabe (E)	≐4.8	≐1.6	≐0.32	0.225	
	Schaefer and Eskinazi (E)		1.3-1.8	0.24-0.28		
	Ferguson (E)			0.32		0.82
normal flat plate	Kármán (E)	5.50	1.7	0.31	0.20	
	Heisenberg (T)	5.45	1.54	0.283	0.229	
	Fage and Johansen (E)	5.25				0.77
angle section	present data (E) $\alpha = -45°$	5.58	1.77	0.32		0.77
	$\alpha = 135°$	4.64	1.36	0.29		0.79

(E) experiment (T) theory

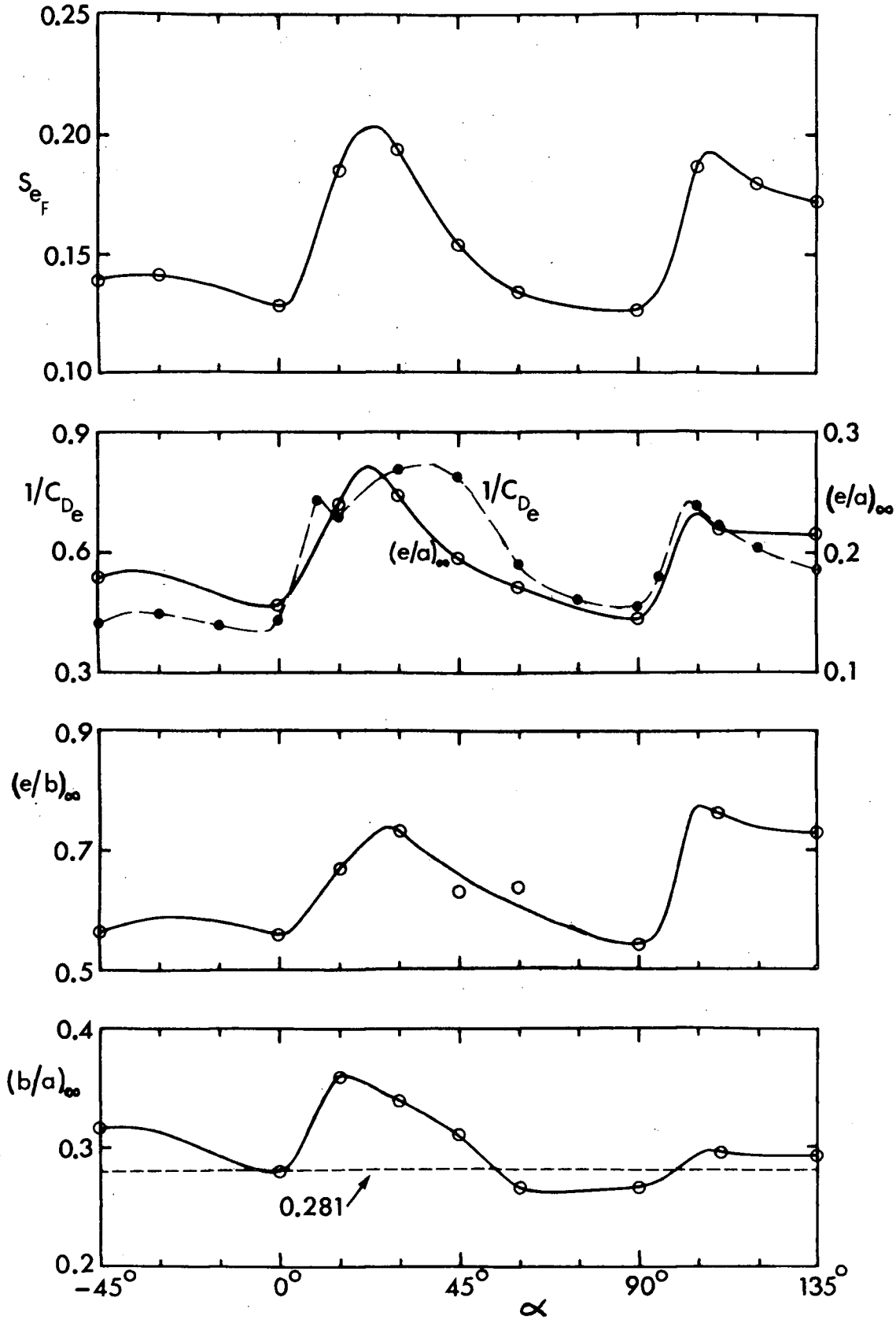

Figure 2-27 Comparison of Strouhal number, wake geometry and drag coefficient for angle section

the similarity of the distributions. All curves tend to peak near $\alpha = 25°$, diminish to almost constant levels between $\alpha = 60°$ and $90°$, and increase rapidly at $\alpha = 100°$ to attain near uniform values over the remaining range. This suggests significant relationship between the wake geometry and body aerodynamic characterics. Introduction of the Universal Strouhal Number, and representation of Strouhal number as a function of drag coefficient by several investigators may be attributed to similar observations of the wake-body interaction.

2.5 Concluding Remarks

Based on the experimental results the following general remarks can be made concerning the aerodynamics of stationary angle sections:

(i) The distributions of the steady lift, drag and pitching moment coefficients obtained from balance measurements for the sharp-edged angle models and the commercial structural angles are in good agreement. Significant variations in the aerodynamic forces and moment with model orientation suggest the possibility of galloping aeroelastic instability. The pressure integrated, steady aerodynamic coefficients compare well with the balance results, thus indicating essentially two-dimensional condition of the model and mean flow.

(ii) The sharp-edged and structural angle models exhibit comparable Strouhal number distributions. The Strouhal

number varies significantly with model orientation but is essentially independent of Reynolds number over the range 10^4 to $15x10^4$. Basing the Strouhal number on projected model width reduces its dependency on angle of attack only slightly. The nondimensional resonant wind speed, being inversely related to the Strouhal number, is a function of model attitude having a minimum near $\alpha = 30°$.

(iii) The pressure fluctuations on the surface of the model change with angle of attack but are independent of Reynolds number over the range $26x10^3$ to $63x10^3$ investigated. The variation of the pressure coefficient around the contour of the section is significant with a minimum value near the forward stagnation point and peak level close to the points of separation. The random modulation of the fluctuating pressure signal can be as large as 2.5 indicating substantial peak pressures.

The fluctuating pressure data confirms the familiar 180° phase difference between the two apparent sides of the model contour. In addition, however, phase differences as large as 50° to 100° may exist between neighbouring taps on each side of the angle section. Fortunately, the effect of these large phase angles on the integrated unsteady force and moment coefficients is less than 10%.

(iv) The spanwise distribution of the fluctuating pressure coefficient is reasonably uniform over the length of

the model examined. However, variation in phase is present which would affect the correlation of the fluctuating forces along the model. This lack of two-dimensionality will aid in reducing possible vortex induced vibrations.

(v) The lateral and longitudinal spacings, together with the vortex velocity increase rapidly behind the body and gradually attain constant values at a large distance downstream ($x/h>6$). As expected, each parameter is a function of the attitude of the angle section. However, it is independent of Reynolds number in the range 26×10^3 to 60×10^3 investigated.

The dependence of the 'near infinity' values of the wake geometry parameters on the orientation of the angle section is similar to that of the Strouhal number and drag coefficient. This variational similarity substantiates the existence of a relationship between the wake geometry and aerodynamic characteristics. The wake survey results for the angle section mounted at $\alpha = -45°$ and $135°$ are comparable to those for a normal flat plate and a circular cylinder, respectively. The distribution of the vortex spacing ratio around Kármán's stability value of 0.281 is of interest.

(vi) Any design criterion to minimize vortex induced vibrations of angle section beams should consider the nature of the forcing function, natural frequency and inherent structural damping. From the stationary angle model investigation of the Strouhal number and aerodynamic

characteristics, it is possible to suggest guide lines for the first two considerations. Any orientations in the ranges $-45° \leq \alpha \leq 10°$ and $50° \leq \alpha \leq 100°$ should be avoided since the magnitude of the unsteady forces ($C_{\bar{l}_s}'$, $C_{\bar{d}_s}'$, $C_{\bar{m}_s}'$) are near maximum. On the other hand, the resonant wind speed curve indicates that angles of attack near 30° should not be used in order to avoid the onset of vortex vibrations. Hence, the use of angle beams in open engineering structures should involve sufficient damping or high natural frequency to prevent possible structural failure due to vortex resonance.

Moreover, the angle section as a bluff cylinder may experience oscillations of a galloping nature. This is indicated by the distributions of the steady lift, drag and pitching moment which exhibit large variations over the complete range of model orientation. In the following chapter the quasi-steady theory incorporating the steady aerodynamic data is employed to predict the occurrence of the galloping instability.

3. DYNAMICS OF AN ANGLE SECTION

3.1 Preliminary Remarks

As indicated in the introduction, bluff cylinders are susceptible to two distinct forms of instability, vortex resonance and galloping, with the vibrations occurring, predominately, in one degree of freedom. The extent of the coupling depends on the relative position of elastic and inertial axes. Therefore, to study the dynamics and associated aerodynamics of an angle section, the wind tunnel models were mounted on a support system providing plunging and/or torsional degree(s) of freedom. Of particular interest were the wind speed and angle of attack ranges conducive to model vibration, and the effect of the resonant motion on the important aerodynamic and wake parameters. In addition, it was desirable to introduce certain appropriate analytical models to predict the dynamics of the system.

Experimentally, the frequency of the coupled motion, and the types and ranges of instabilities were found to be similar to those in the single degree of freedom. Furthermore, the phase phenomenon between the plunging and torsional modes confirmed the concept of two distinct families of coupled vibrations, one predominantly plunging and the other torsion, as reported by Kosko[1] and Wardlaw.[2] Therefore, it was possible to obtain pertinent information about critical orientations, wind speeds and the characteristic features of the instabilities by studying, both experimentally and theoretically, the plunging and torsional degrees of freedom, separately.

In general, the instability may be a combined effect of both vortex resonance and galloping excitation. This situation was observed for the plunging degree of freedom at several orientations and damping levels. A judicious choice of damping or model size was required in such instances to isolate the two phenomena, thus permitting separate study of each form of instability. Based on this consideration, the experimental investigation was divided into two portions; vortex resonance, and galloping oscillations. However, for the torsional degree of freedom, no galloping was observed over the wide ranges of wind speed and model orientation investigated, thus suggesting that a structural angle section is not likely to exhibit this form of instability in torsion unless very low damping or relatively high wind speed is encountered. This observation is substantiated by a theoretical analysis based on the nonlinear, quasi-steady approach. Of greater importance is the violent, vortex resonant type of instability which was observed and investigated with the angle models at various damping levels and model orientations.

Since quasi-steady galloping theory for the plunging case[17] is well established, more attention is directed towards the development of an analogous theory for the torsional mode. The problem is somewhat complicated due to the fact that the nonlinear forcing function (moment) depends on the instantaneous angular position as well as the velocity. Sisto[14] and Ii,[19] analyzing the problem of stall-flutter, eliminated this complication by assuming a mean moment distribution as a function of

the instantaneous angle of attack α which in turn was chosen to satisfy the downwash at the three-quarter chord point. This empirical approach parallels the classical flutter theory. However, since the flow fields during stall and classical flutter are quite different, there is some doubt as to the significance of the three-quarter chord point in stall flutter analysis. A modified theory for the galloping instability of bluff cylinders is presented.

This chapter outlines the important aspects of the vortex resonant and quasi-steady galloping theories with application to the specific configuration under investigation. A description of the additional instrumentation and experimental procedure is presented, followed by a comparison and discussion of the analytical and experimental results. A concluding section summarizes the useful information concerning angle sections under dynamical condition.

3.2 Experimental Arrangement

3.2.1 Model Mounting System

The investigations into the dynamic instability of an angle section were conducted by mounting the angle models, previously described, on a suitably designed support system shown schematically in Figure 3-1. The mounting arrangement providing plunging and torsional degrees of freedom was essentially composed of a lateral air bearing system[49] and cross-spring pivots. The system of journal air-bearings located on a frame encircling the tunnel test section gave the model a plunging degree of freedom normal to the wind direction. The crossed

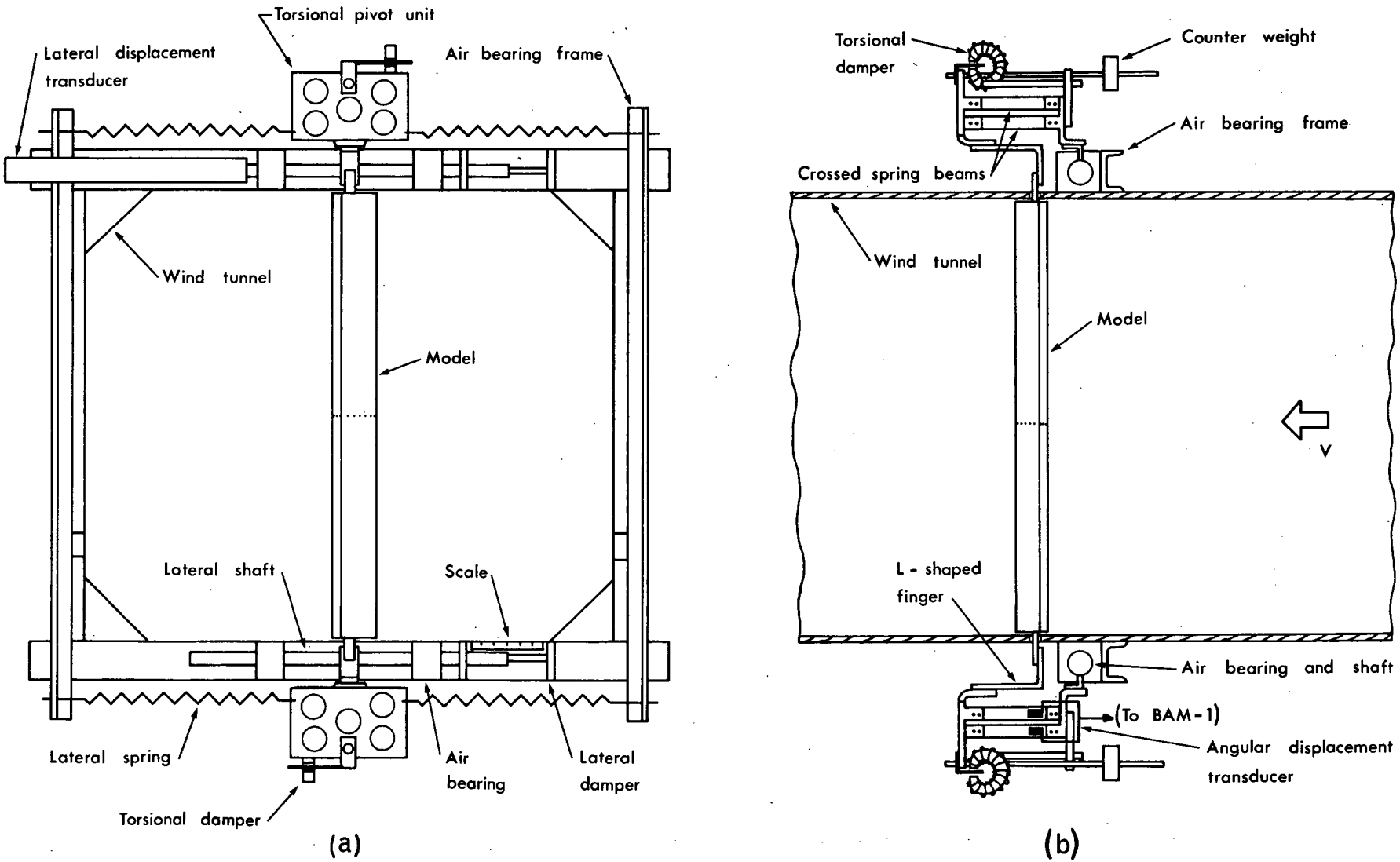

Figure 3-1 Details of model support system with plunging and torsional degrees of freedom (a) plunging arrangement (b) torsional assembly

beam pivot units, providing rotational stiffness for the torsional mode, were fixed to the lateral air bearing shafts by suitable brackets and held transversely by the lateral coil springs to make the two vibrational systems independent. The model was fastened to the free ends of the pivot units by two L-shaped fingers. Lateral and angular displacements of the model were detected by air-core transformer and strain-gauge bridge transducers, respectively. Variable damping was introduced independently into each degree of freedom system through electromagnetic eddy-current dampers. To permit investigation of the model dynamics in the individual degrees of freedom, clamps were provided to eliminate the unwanted mode. Details of the lateral air bearing system and auxiliary instrumentation designed by Smith have been reported in the literature.[49,50] However, since the cross-spring pivot units were designed particularly for the present research programme a brief summary of the pertinent constructional details is provided.

Basically, the pivots consist of two pairs of uniform, crossed thin-metal strips rigidly fixed at their ends to the two parts between which relative angular movement is required. It is significant that this device introduces a minimum of inherent damping, and for small movement (<15°), the axis of rotation remains essentially stationary at the intersection of the undeflected crossed strips.[72] Theoretical investigations in the design of cross-spring pivots have been presented by Eastman,[73] Haringx,[74] Wittrick[75,76] and others. Young[77] conducted an experimental investigation and arrived at several empirical

relationships for the design characteristics. Based on the theoretical development by Wittrick[76] and the experimental information given by Young, a workable assembly was arrived at for supporting the angle models with a torsional degree of freedom. The two beams, connected to suitable end brackets, crossed orthogonally at 87.3% (i.e., $1/2(1+\sqrt{5}/3)$) of the distance from the moving end. This cross over position was selected because of its superior performance characteristics as pointed out by Wittrick. The thin metal beams, made from blue tempered spring steel, have a free working length of 2.80 in. The particular cross-sectional dimensions, 0.030x0.500 in., were selected from consideration of rigidity and stiffness. A counter weight (Figure 3-1(b)) was added to produce a pivot assembly for which the overall centre of gravity of the oscillating components of the pivot coincided with the inertial axis of the model.

3.2.2 Instrumentation and Test Procedures

The lateral and angular displacements of the angle models were recorded using the instrumentation layout shown in Figure 3-2. The top air bearing shaft was of sufficient length to project into the lateral displacement transducer.[49] With a 10 kc sinusoidal signal, the interference of the aluminum shaft with the magnetic coupling between the co-axial cylindrical coils gave rise to an amplitude modulated output proportional to the model displacement. A full wave rectifier and RC filter circuit was used for demodulating the high-frequency carrier. The torsional displacement of the oscillating model was measured using a strain-gauge type of transducer incorporated in the

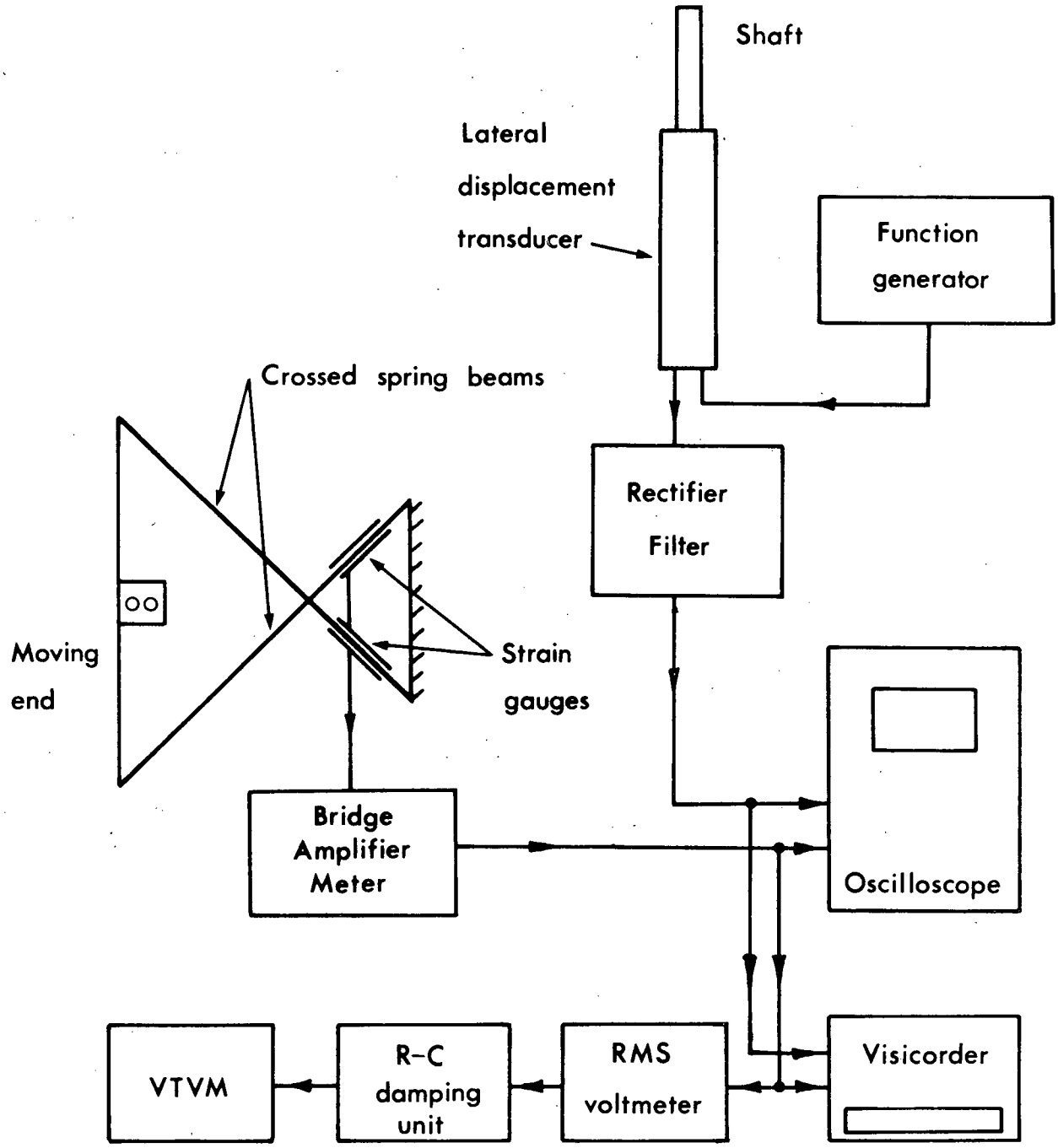

Figure 3-2 Instrumentation layout for plunging and torsional displacement measurements

lower cross-spring pivot unit. Metallic foil strain gauges, bonded to the beams and connected to form a 4-arm Wheatstone bridge circuit in conjunction with an Ellis Bridge-Amplifier-Meter, produced an electrical signal corresponding to the angular displacement. The model displacement signals were recorded either on a storage oscilloscope or Visicorder. When amplitude modulation of the response signals occurred, maximum and minimum as well as mean (using the rms voltmeter circuit) displacements were recorded.

Controlled damping, in addition to that inherent with the individual oscillating support systems, was introduced by means of electromagnetic dampers, which dissipated energy through eddy currents. The amount of magnetic damping was proportional to the input d.c. current. For the lateral system, the dampers designed by Smith[49] were employed with the aluminum mounting shafts being used as the dissipative medium. Analogous, horseshoe shaped dampers with thin copper strips intersecting the magnetic field in the gaps were constructed for the torsional assembly. A variable a.c. current source was incorporated in each damper arrangement to erase the undesirable residual magnetism induced in the iron cores of the electromagnets. Using the standard technique of logarithmic decrement, the electromagnetic dampers were calibrated over a range of d.c. current using suitable streamlined models[50] in place of the angle section. The viscous nature of the magnetic damping was indicated by the linearity of the logarithmic decrement curves from which the values of the damping coefficients were determined. To introduce

further damping during the torsion experiments, the horseshoe electromagnets were replaced by permanent magnets (Cinaudagraph Corp., Type 6.30540) with approximate field strength of 5225 Gauss each. The magnitude of the damping was varied by placing aluminum strips of various thicknesses into the gap between the poles.

From the Strouhal number data given in Figure 2-11 and using equation (2.1), the approximate wind speeds for vortex resonance of the 1 in. and 3 in. angle models were calculated. The model orientation, system natural frequency and model size were the parameters affecting the resonant velocities. Extensive plunging and torsional amplitude measurements were conducted around the fundamental resonant conditions with increasing and decreasing wind speeds for various model attitudes and damping levels. No detectable sub- or higher- harmonic resonance was observed during any of the amplitude tests.

The wake and aerodynamic characteristics associated with an angle section experiencing vortex excited motion were obtained using the procedure described in Chapter 2 (section 2.3). A combination of the instrument layouts shown in Figures 2-4 and 3-2 was used for measuring the frequencies of vortex shedding and cylinder oscillation. Corresponding phase data between the pressure and displacement signals was obtained over the wind speed ranges for which the cylinder and vortex shedding frequencies coincided. The signals were averaged on Visicorder charts. Investigations of the wake geometry, as well as the amplitude and phase of the fluctuating surface pressures for the oscillating model were conducted at wind speeds corresponding to peak reson-

ance. Due to the dynamical condition of the angle section, the vortex velocity was calculated using the modified formula

$$\frac{V_v}{V} = \left(\frac{f_v/f_n}{V/V_{res}}\right) S_h\left(\frac{a}{h}\right) \qquad (3.1)$$

The final results were compared with the corresponding values for the stationary model.

For the galloping instability, investigation of the model dynamics at various angles of attack and damping levels was conducted over the wind speed range 0-70 ft/sec. If oscillations occurred, further intensive study was conducted for increasing and decreasing wind speeds with the model starting from rest or from the existing displacement. Depending on the oscillator characteristics at some orientations, the model required an initial displacement to start oscillating after which it would attain a larger, stable amplitude. The time taken for galloping oscillations to build-up from a predetermined initial displacement to 95% of the final stable amplitude was obtained by displaying the signal on a storage oscilloscope. This gave an indication of the severity of the instability.

3.3 Response of an Angle Section with Combined Plunging and Torsional Degrees of Freedom

The model amplitude data (Figure 3-3) was obtained for the 3 in. dynamic angle model mounted at $\alpha_o = -45°$ and with the axis of rotation of the torsional system coinciding with shear centre of the angle section. The plunging and torsional spring stiffnesses were selected to provide a frequency ratio

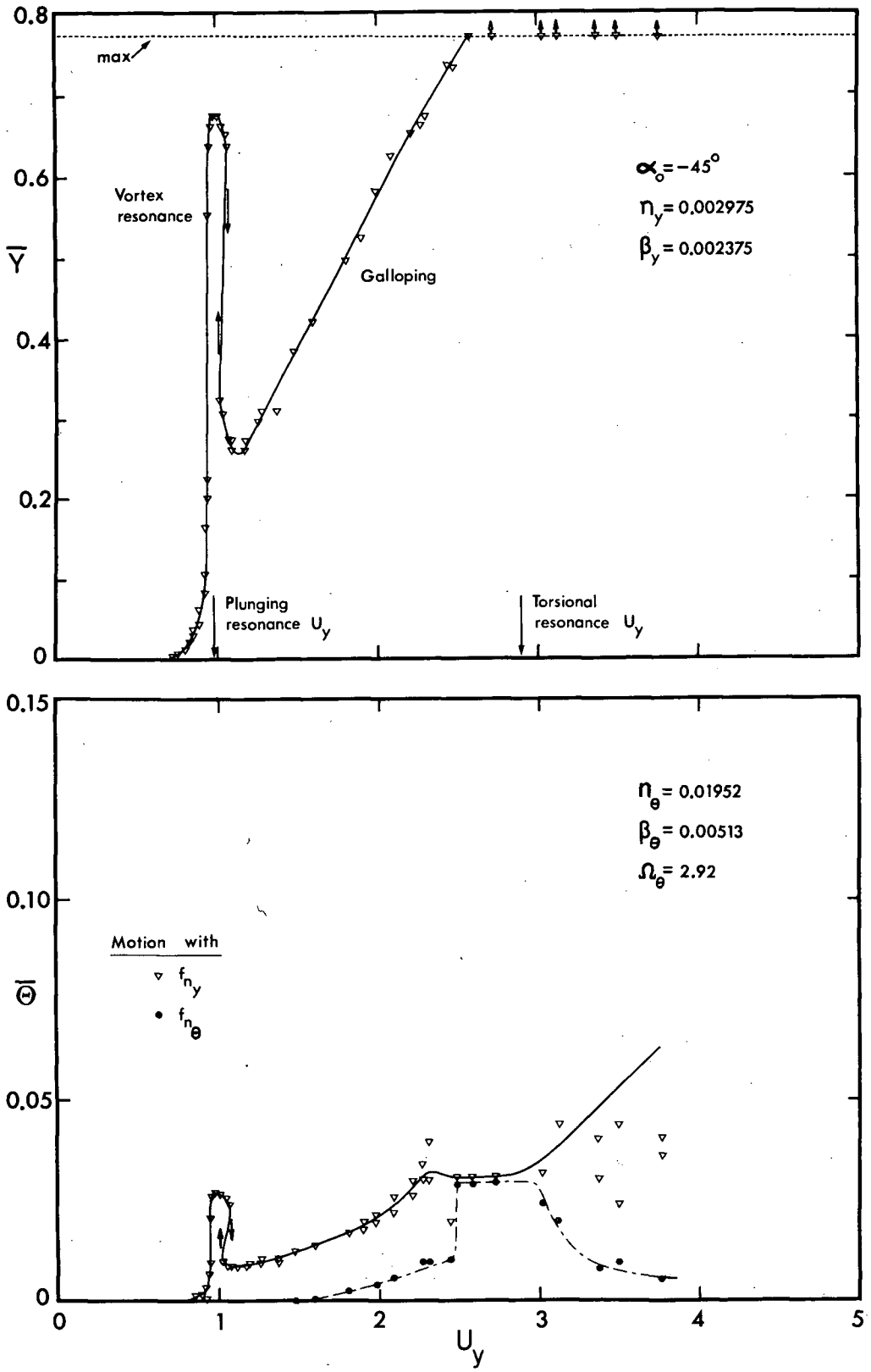

Figure 3-3-i Displacement measurements for angle model at α_o = -45° with combined plunging and torsional degrees of freedom (plunging galloping initiated below torsional resonance)

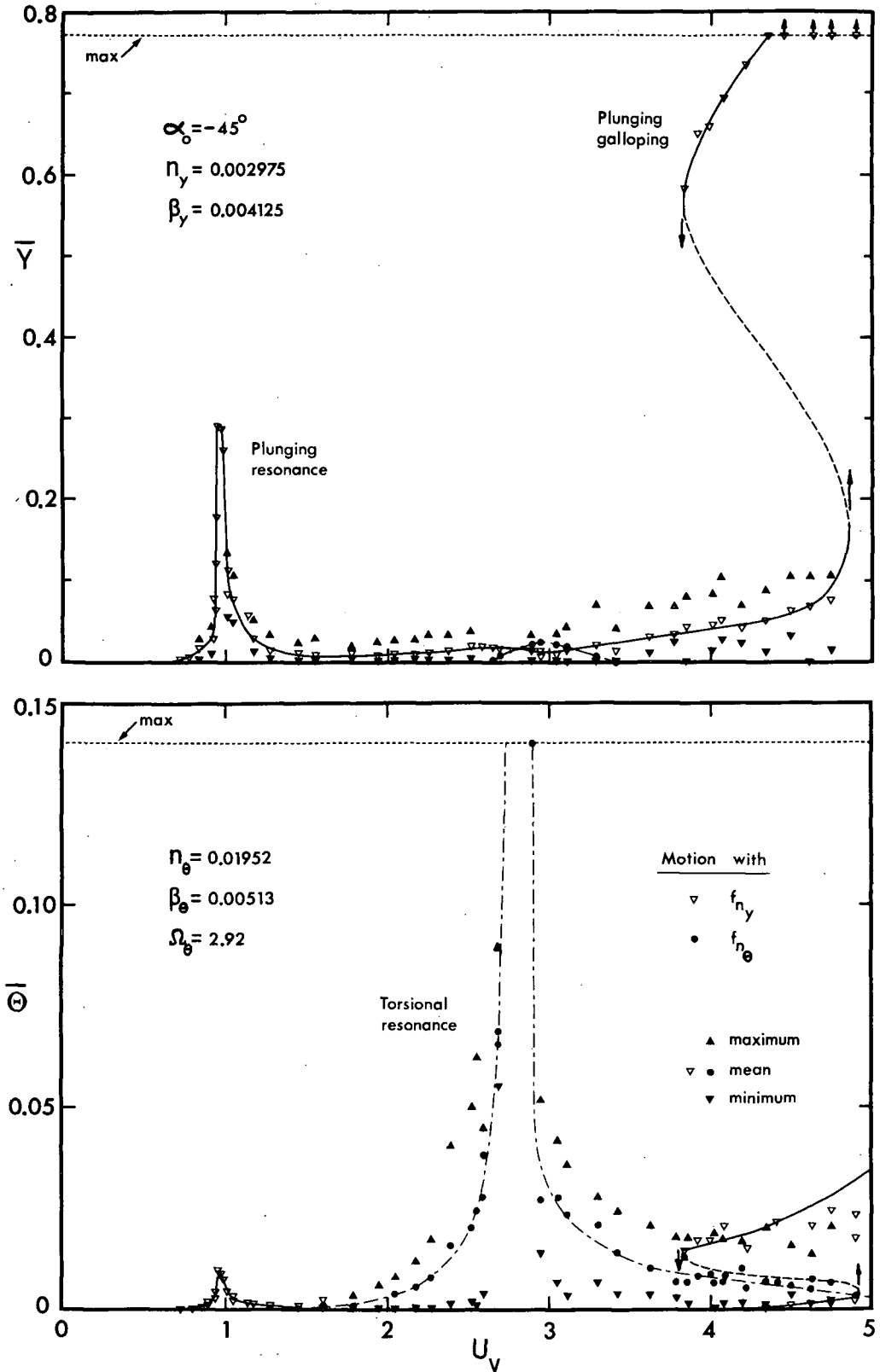

Figure 3-3-ii Displacement measurements for angle model at α_o = -45° with combined plunging and torsional degrees of freedom (plunging galloping initiated about torsional resonance)

representative of typical structural angle beams, ($\omega_{n_\theta}/\omega_{n_y} = 2.92$). Two damping levels for the plunging system were considered so as to initiate lateral galloping oscillations at wind speeds below and above the torsional resonant condition. This permitted a study of the galloping motion effects on the torsional resonance. The maximum damping obtainable with the torsional electromagnetic dampers was not sufficient to restrict the violent, torsional vortex resonance to the limit of the supporting system (dotted line at $\bar{\theta} = 0.14$ in Figure 3-3-ii). Both the induced and natural frequency displacement components for the plunging and torsional oscillations are plotted. The presence of amplitude modulation, exhibited at particular wind speeds, is indicated by the maximum, mean and minimum displacement values.

It is of interest to note that the response of the angle section over discrete wind speed ranges can be categorized by the type of instability and predominant degree of freedom as follows:

(i) vortex excited plunging;

(ii) galloping induced plunging;

(iii) vortex excited torsion.

No occurrence of natural galloping instability in the torsional mode of vibration was observed over the wind speed range investigated. The separation of the plunging and torsional resonant conditions, a result of the difference in the natural frequency values, is similar to the vibrational characteristics of continuous angle beams[2] except in that case many discrete ranges of wind speed may be obtained because of the infinite number of principal frequencies. To better understand the nature of the

instability of the rigid angle section, the amplitudes in the individual modes of vibration were measured. The tests were performed by clamping the torsional and lateral systems consecutively, thus obtaining plunging and torsional amplitude data as shown in Figures 3-4 and 3-5. The lateral and torsional damping levels were identical to the values used for the two degree of freedom investigation.

The results indicate that, although the elastic and inertial axes for the section do not coincide, the coupled motion is at the natural frequencies f_{n_y} and f_{n_θ} of the single degrees of freedom. This is due to the fact that the ratio $m\sigma^2/\bar{I}_o$ is comparatively small for an angle section, thus reducing the coupling effect.

Comparison of the response data reveals that the coupled system exhibits plunging motion which is almost identical to that for the single degree of freedom. On the other hand, the torsional amplitude depends on the relative position of the plunging galloping instability. For the higher damping level (Figure 3-3-ii), the torsional resonant displacements are similar to those in Figure 3-5, characterized by a sharp peak and significant amplitude modulation. However, at the lower damping (Figure 3-3-i), the torsional results do not resemble the normal resonant curve due to the presence of the plunging, galloping motion. The resonant peak is substantially reduced in magnitude and the modulation characteristic is virtually non-existent. The induced $\bar{\Theta}$ curves near $U_y = 1$ are a result of the lateral resonant condition. For higher wind speeds, the lateral gallop-

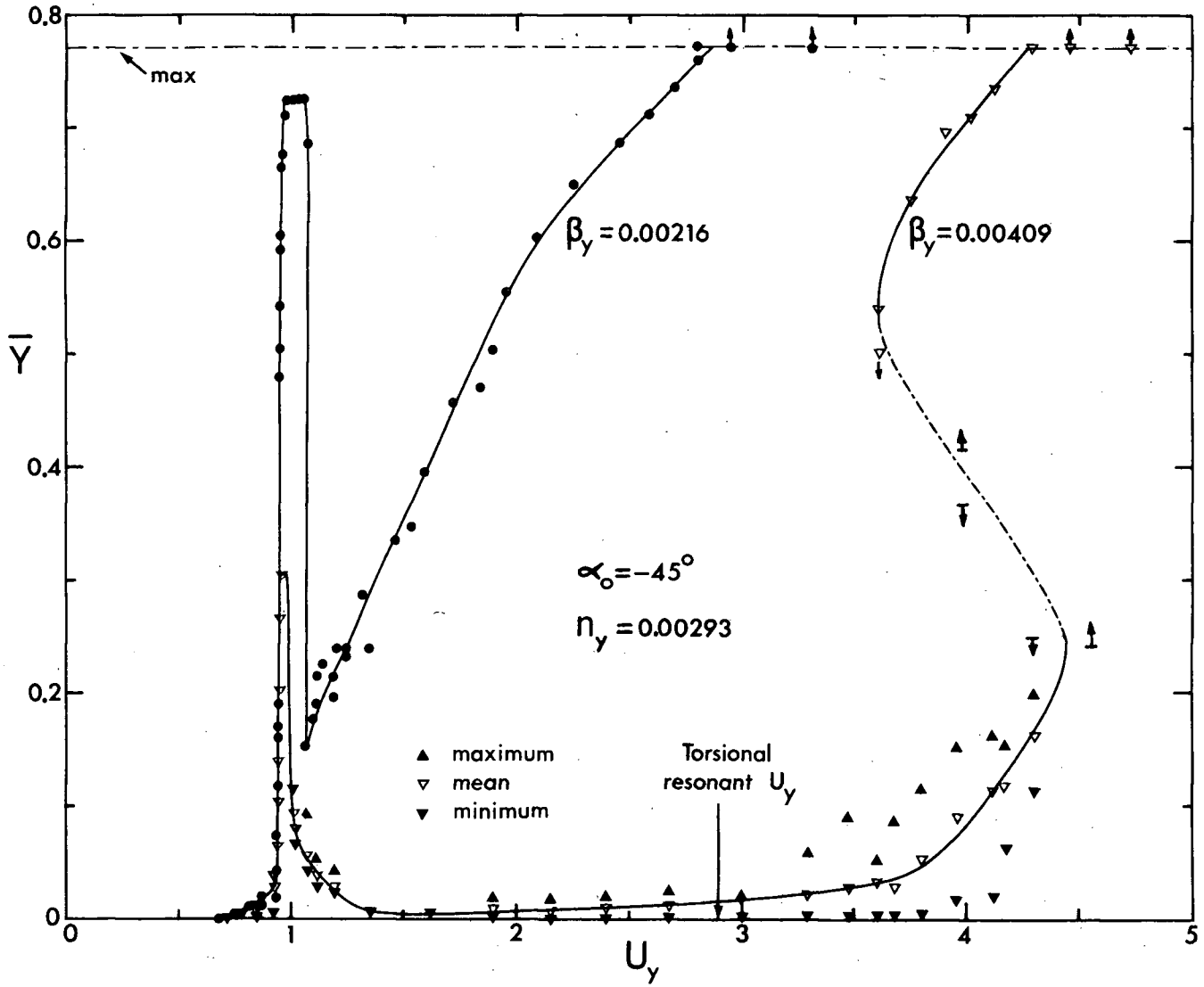

Figure 3-4 Response of angle model at $\alpha_o = -45°$ with plunging degree of freedom only

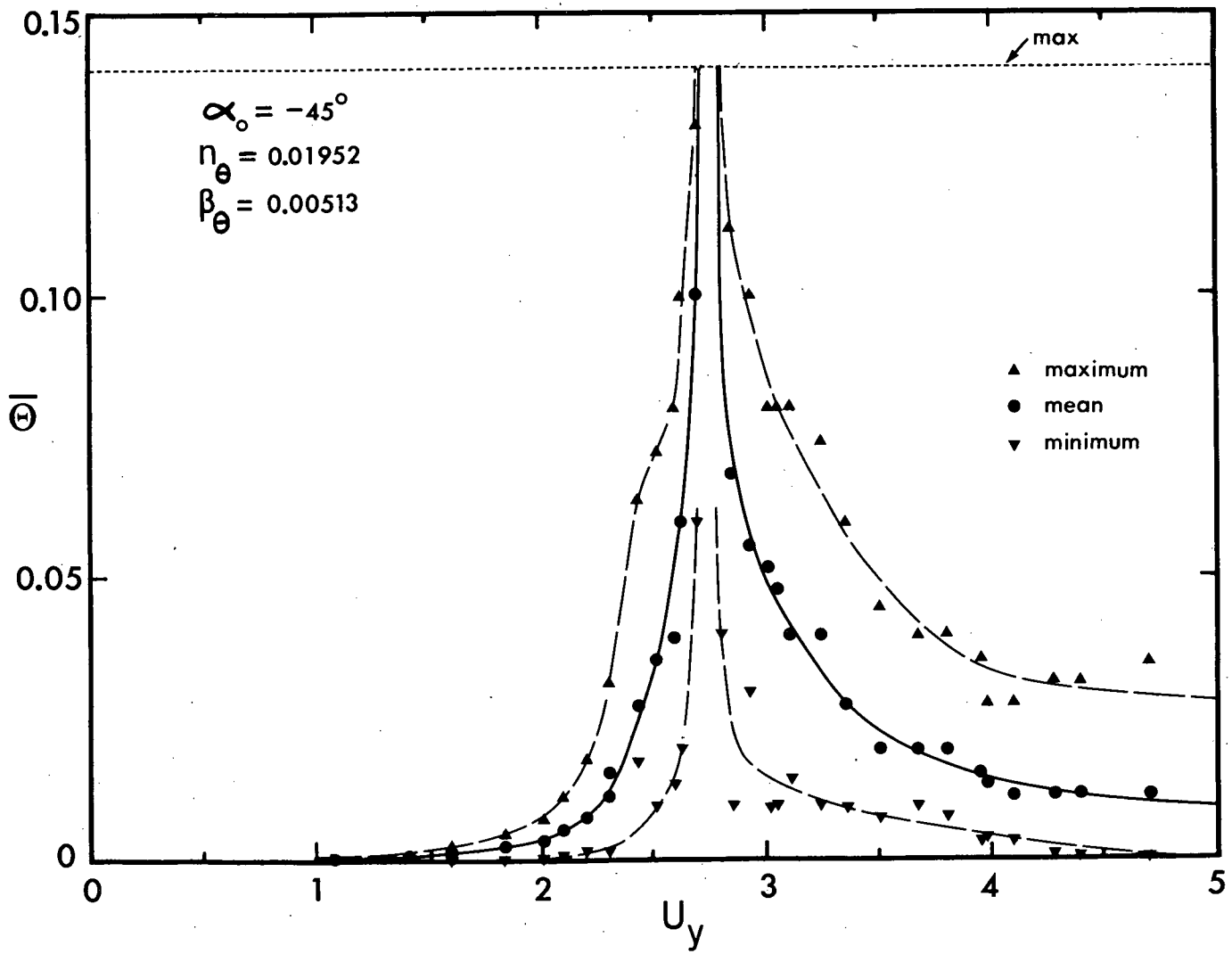

Figure 3-5 Response curve for angle model at $\alpha_o = -45°$ with torsional degree of freedom only and rotational axis at shear centre

ing instability produces a torsional motion of frequency f_{n_y} which increases in magnitude proportional to the plunging displacement. However, for the lower damping case, the induced amplitude is controlled by the natural torsional frequency until the range of vortex resonance is exceeded. Unfortunately, the plunging oscillation rose to the maximum allowable displacement of the air-bearing support system during the range of torsional resonance. Therefore, the torsional curves for $U_y > 2.5$ represent only the anticipated values for unrestricted galloping mode. Similar induced plunging motion of frequency f_{n_θ} is observed at the higher damping level during the torsional resonance.

A comment concerning the phase of the coupled motion is appropriate here. It was observed that the lateral and torsional displacements of the same frequency were in phase for the plunging resonant and galloping oscillations, while at torsional resonance the modes were 180° out of phase. This suggests the presence of virtual centres of rotation, denoted as hinge points. For the former case, the results in Figure 3-3-i indicate that the virtual centre of rotation is located far downstream at approximately $x/h = 30$. On the other hand, the latter case (Figure 3-3-ii) corresponds to a hinge point located just forward of the inertial axis. Thereby, depending on the predominant mode, the coupled oscillations can be considered as rotational motion about two different centres. The first corresponds to essentially plunging motion, while the other represents torsion. Thus, the present measurements confirm the existence of the two families of virtual hinge points predicted by Kosko[1] and observed by Wardlaw[2] for an

angle section beam. Garland[78] has presented similar theoretical and experimental results for a cantilever, extended-channel beam.

It is of interest to note, that the experimental results reported by Wardlaw on the dynamics of an angle beam are compatible, in general, with the trends obtained from the present investigations. The resonant vibrations can be predicted from the Strouhal data, with only a few exceptions. In addition, Wardlaw's measurements reveal that the oscillations at many angles of attack are predominantly resonant in nature rather than galloping. Nevertheless, at certain orientations, the oscillations over discrete wind velocity ranges appeared to exhibit galloping characteristics.

In summary, the response of an angle section with combined plunging and torsion indicates that the oscillations occur essentially in one of the two degrees of freedom. The measurements of frequency and phase further substantiate this observation. Thereby, the type of instability, relative amplitude and the corresponding critical wind speed can be determined by studying the system dynamics in the individual degrees of freedom. In what follows, this approach is adopted to understand the nature of the vortex resonant and galloping instabilities.

3.4 Theoretical Development

Derivation of the governing plunging and torsional equations of motion and their solutions are given in Appendix IV with a summary of the basic relations provided here. Assuming linear spring and viscous damping and expressing the applied

aerodynamic force F_y or moment M_θ in coefficient form, the equations of motion can be written as

$$m\ddot{y} + r_y\dot{y} + k_y y = \tfrac{1}{2}\rho V^2 h \ell C_{F_y}(y,\dot{y};t) \qquad (3.2)$$

$$I\ddot{\theta} + r_\theta\dot{\theta} + k_\theta\theta = \tfrac{1}{2}\rho V^2 h^2 \ell C_{M_\theta}(\theta,\dot{\theta};t) \qquad (3.3)$$

Evaluation of these equations during particular types of aerodynamic excitations forms the subject of this analysis.

3.4.1 Vortex Resonance

Since the plunging and torsional equations are similar in form, only the plunging analysis is presented. Assuming a sinusoidal forcing function, equation (3.2), in nondimensional form, becomes

$$\Omega_v^2\ddot{Y} + 2\beta_y\Omega_v\dot{Y} + Y = \eta_y U^2 C_{\bar{l}'} \sin\tau_v \qquad (3.4)$$

giving the steady-state solution as

$$\bar{Y} = \eta_y C_{\bar{l}'} \frac{U^2}{\sqrt{(1-\Omega_v^2)^2 + (2\beta_y\Omega_v)^2}} \qquad (3.5)$$

Evaluation of (3.5) gives the familiar resonance curves with damping coefficient as the distribution parameter. For the peak amplitude ($\Omega_v = 1.0$), equation (3.5) reduces to

$$\bar{Y}_{max} = \tfrac{1}{2}\frac{\eta_y}{\beta_y} C_{\bar{l}'} U_{res}^2 \qquad (3.6)$$

Parkinson et al[79] considered a slightly different approach to obtain a solution of the form

$$\bar{Y}_{max} = \frac{\omega_{n_y}}{\omega_{c_y}} \frac{n_y U^2}{2 \beta_y} C_{\bar{l}'} \sin \Phi_{AF} \tag{3.7}$$

which incorporates the experimentally observed vortex shedding phenomenon through the variables Φ_{AF} and $\omega_{n_y}/\omega_{c_y}$.

3.4.2 Galloping Instability

Using the quasi-steady approach,[17] which assumes no aerodynamic hysteresis effects in the force and moment characteristics and the vortex shedding frequency to be far removed from the cylinder values, the governing differential equations of motion (3.2) and (3.3) can be put in the nondimensional form

$$\ddot{Y} + Y = \mu_y f_y(\dot{Y}) \tag{3.8}$$

$$\ddot{\Theta} + \Theta = \mu_\theta f_\theta(\Theta, \dot{\Theta}) \tag{3.9}$$

where the variables μ_y and μ_θ are modified mass and moment of inertia parameters, respectively. The function $f_y(\dot{Y})$, incorporating the aerodynamic and viscous forces, is represented as a polynomial in $\dot{Y}$ using the steady lift and drag results. Similarly, $f_\theta(\Theta, \dot{\Theta})$ is a polynomial related to the steady pitching moment with an assumption that the contourlines of $C_{M_\theta}(\Theta, \dot{\Theta})$ are linear and parallel. For a system in air, both μ_y and μ_θ $<< 1$ making equations (3.8) and (3.9) amenable to quasi-linear solution techniques.

3.4.2.1 Singularities and Stability in the Small

Analytically, the condition of stability of the motion in the small can be determined[80] by investigating the singularities in the phase plane. For the plunging system, equation (3.8) can be reduced to

$$\begin{aligned} \dot{Y} &= Z \\ \dot{Z} &= -Y + \mu_y f_y(Z) \end{aligned} \tag{3.10}$$

giving

$$\frac{dZ}{dY} = \frac{-Y + \mu_y f_y(Z)}{Z} \tag{3.11}$$

It is apparent that the only singularity for the system is located at the origin of the phase plane. Similarly, the torsional equation (3.9) becomes

$$\begin{aligned} \dot{\Theta} &= X \\ \dot{X} &= -\Theta + \mu_\theta f_\theta(\Theta, X) \end{aligned} \tag{3.12}$$

giving

$$\frac{dX}{d\Theta} = \frac{-\Theta + \mu_\theta f_\theta(\Theta, X)}{X} \tag{3.13}$$

The singularities of (3.13) are located on the Θ axis at the points given by the roots of the polynomial equation

$$\Theta n_\theta U^2 \left\{ -\left(a_1 c + \frac{1}{n_\theta U^2}\right) + a_2 c^2 \Theta - a_3 c^3 \Theta^2 + \cdots + (-1)^N a_N c^N \Theta^{N-1} \right\} = 0 \tag{3.14}$$

Again the origin represents one of the singularities. The remaining roots of the equation, being relatively large, do not affect the condition of stability unless the torsional disturbances are severe.

The nature of the singular points and the phase trajectories in their vicinity can be studied through a linear analysis of the system using the characteristic roots

$$(\lambda_y)_{1,2} = \frac{\mu_y}{2}(U - U_o) \pm \sqrt{\left[\frac{\mu_y}{2}(U - U_o)\right]^2 - 1} \qquad (3.15)$$

for the plunging system (3.9), and

$$(\lambda_\theta)_{1,2} = \frac{\mu_\theta}{2}(Us - U_o) \pm \sqrt{\left[\frac{\mu_\theta}{2}(Us - U_o)\right]^2 - (1 + \mu_\theta U^2 c)} \qquad (3.16)$$

for the torsional relation (3.11).

Since μ_y and μ_θ << 1, the roots are complex conjugates indicating the singularity at the origin to be either a centre or a focus depending on the magnitude of the real part. For the particular case when $U = U_o$ or U_o/s, the singular point is a centre. These critical values represent the initial wind velocities for the onset of the instability. All other values of U give rise to a focus, whose stability, based on the sign of the real part, is determined by the criterion

plunging:	$U < U_o$	stable	(3.17)
	$U > U_o$	unstable	
torsion:	$U < U_o/s$	stable	(3.18)
	$U > U_o/s$	unstable	

These conditions are based on the assumption that U_o and U_o/s are positive. However, it is possible for them to be negative as governed by the sign of the coefficient a_1, which designates the slope of the aerodynamic force or moment curve at the origin, and on the sign of the torsional parameter s. The

system is called a "soft" oscillator if a_1 or $a_1 \cdot s$ is positive because for sufficiently large value of U (greater than the critical velocity), the model will oscillate from rest in presence of an arbitrarily small disturbance. On the other hand, when it is negative, the system is denoted as a "hard" oscillator since no vibration will commence from rest. However, sustained oscillation may occur if an initial disturbance exceeding some required minimum value is provided. This criterion is analogous to the concept of negative and positive aerodynamic damping used by many investigators.

Thus, from the stability analysis in the small, pertinent information about the critical angles of attack and wind speeds can be obtained by examining the stationary aerodynamic force and moment distributions given in Chapter 2, Figure 2-8. For the angle section in plunging, stability can be studied using Den Hartog's[9] criterion

$$\frac{dC_L}{d\alpha} + C_D \begin{cases} > 0 & \text{stable} \\ < 0 & \text{unstable} \end{cases} \qquad (3.19)$$

which incorporates the steady lift and drag coefficients. It is apparent that, if the lift curve has sufficiently large negative slope, the angle section may be self-excited. For the torsional motion, such a simple relation is not available, hence direct study of the system parameters is required. In the range $-45° \leq \alpha_o \leq 45°$, s is positive but becomes negative for $\alpha_o > 45°$. Therefore, the sign of $a_1 \cdot s$ depends on a_1. As C_{M_θ} is proportional to $-C_M$, the system will behave as a soft oscillator in the range $-45° \leq \alpha_o \leq 45°$ if the slope of C_M plot is negative. Likewise, for

$\alpha_o > 45°$, an angle section is a soft oscillator if the slope of the moment curve is positive. Thus, as illustrated in Figure 2-8(c), a structural angle member may oscillate from rest in a torsional mode for $-45° \leq \alpha_o \leq 10°$ and $40° \leq \alpha_o \leq 60°$.

3.4.2.2 Limit Cycles and Build-up Time

The galloping motion and its stability in the large can be studied using the method of Variation of Parameters. For the plunging system, the solution can be written as

$$\begin{aligned} \dot{\bar{Y}} &= -\bar{Y}\,\delta_y(\bar{Y}) \\ \dot{\phi} &= 0 \end{aligned} \tag{3.20}$$

where $\delta_y(\bar{Y})$ is a polynomial related to $f_y(\dot{Y})$. For the torsional mode, however, $\dot{\phi}$ does not reduce to zero as in the plunging case but becomes a function of Θ and U giving the solution as

$$\begin{aligned} \dot{\bar{\Theta}} &= -\bar{\Theta}\,\delta_\theta(\bar{\Theta}) \\ 1 + \dot{\phi} &= 1 - K_\theta \end{aligned} \tag{3.21}$$

where $\delta_\theta(\bar{\Theta})$ and K_θ are polynomials related to $f_\theta(\Theta,\dot{\Theta})$. The term $(1-K_\theta)$ represents a reduced frequency parameter.

The amplitude of the sustained motion is evaluated by setting $\dot{\bar{Y}} = \dot{\bar{\Theta}} = 0$, and obtaining the real positive roots, $\bar{Y}_j$ or $\bar{\Theta}_j$, of the algebraic equations

$$\delta_y(\bar{Y}) = 0 \tag{3.22}$$

$$\delta_\theta(\bar{\Theta}) = 0 \tag{3.23}$$

The nature of the response is determined by Lyapunov's Stability criterion

$$\text{plunging:} \quad \left.\frac{\partial \dot{\bar{Y}}}{\partial \bar{Y}}\right|_{\bar{Y}=\bar{Y}_j} \begin{cases} < 0 & \text{stable} \\ > 0 & \text{unstable} \end{cases} \tag{3.24}$$

$$\text{torsion:} \quad \left.\frac{\partial \dot{\bar{\Theta}}}{\partial \bar{\Theta}}\right|_{\bar{\Theta}=\bar{\Theta}_j} \begin{cases} < 0 & \text{stable} \\ > 0 & \text{unstable} \end{cases} \tag{3.25}$$

or, in the light of (3.20) and (3.21)

$$\text{plunging:} \quad \left.\frac{\partial \delta_y}{\partial \bar{Y}}\right|_{\bar{Y}=\bar{Y}_j} \begin{cases} > 0 & \text{stable} \\ < 0 & \text{unstable} \end{cases} \tag{3.26}$$

$$\text{torsion:} \quad \left.\frac{\partial \delta_\theta}{\partial \bar{\Theta}}\right|_{\bar{\Theta}=\bar{\Theta}_j} \begin{cases} > 0 & \text{stable} \\ < 0 & \text{unstable} \end{cases} \tag{3.27}$$

The time of amplitude build-up is readily obtained from (3.20) and (3.21) by evaluating the integrals

$$\text{plunging:} \quad \tau = \int_{\bar{Y}_o}^{\hat{Y}_j} -\frac{d\bar{Y}}{\bar{Y}\,\delta_y(\bar{Y})} \tag{3.28}$$

$$\text{torsion:} \quad \tau = \int_{\bar{\Theta}_o}^{\hat{\Theta}_j} -\frac{d\bar{\Theta}}{\bar{\Theta}\,\delta_\theta(\bar{\Theta})} \tag{3.29}$$

where $\bar{Y}_o$, $\bar{\Theta}_o$ represent small initial displacements and $\hat{Y}_j$, $\hat{\Theta}_j$ are some prescribed fractions (say 95%) of the $\bar{Y}_j$, $\bar{\Theta}_j$ values, respectively.

3.5 Results and Discussion

3.5.1 Vortex Resonance

3.5.1.1 Model Amplitude - Velocity Measurements

Shown in Figure 3-6 are typical lateral and torsional displacement signals obtained for wind speeds corresponding to peak vortex resonance. The signals indicate the sinusoidal wave-

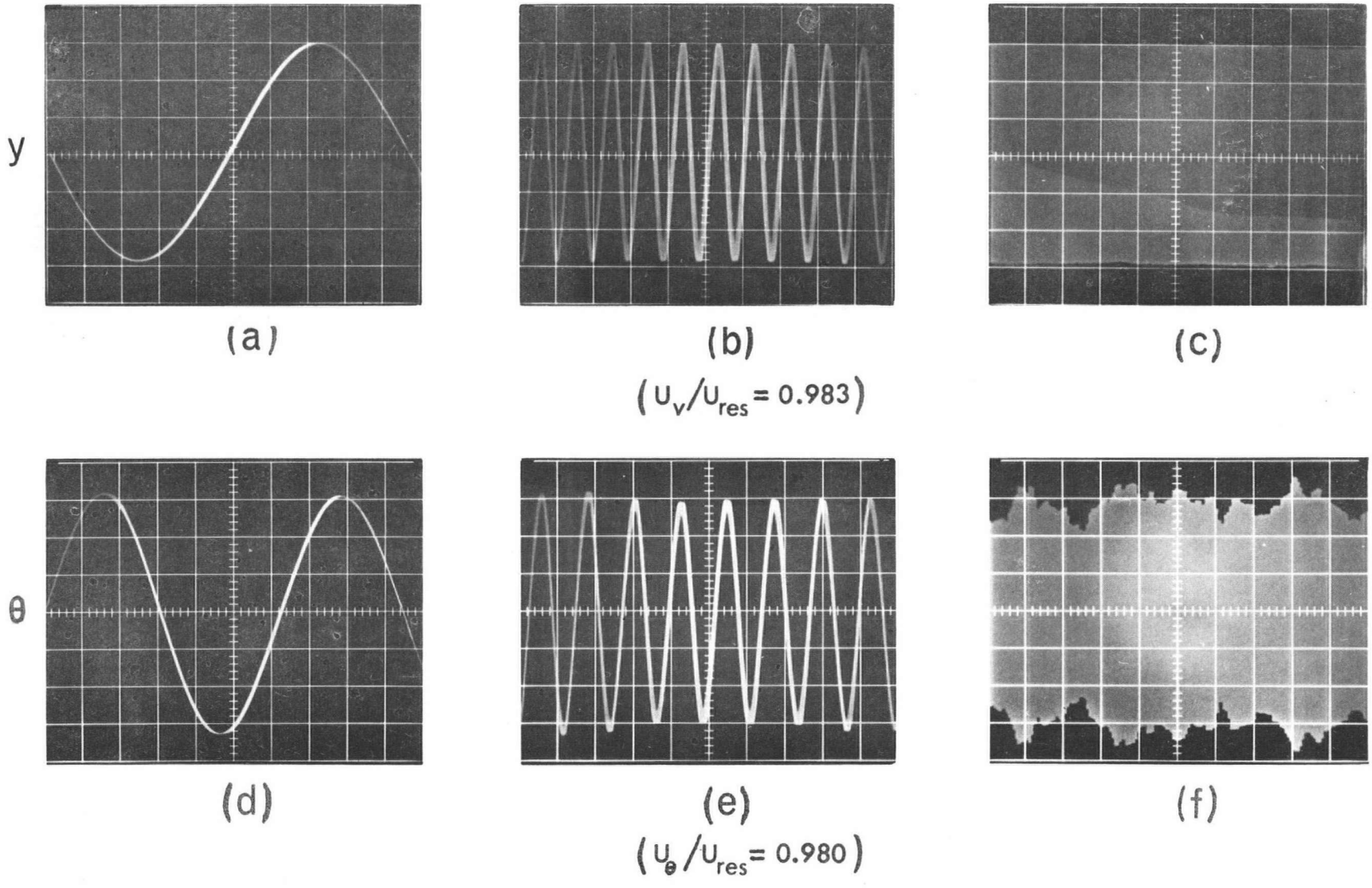

Figure 3-6 Typical displacement signals for angle model experiencing vortex excited plunging or torsional motion

form and constant frequency of the displacements. The plunging steady-state amplitude is uniform at peak resonance with some slight variations occurring only at wind speeds above and below resonance. On the other hand, the torsional motion exhibits substantial random, amplitude modulation (Figure 3-6(f)), which may attain a definite frequency at other wind speeds as illustrated in Figure 3-7(a) and (b). When further above the resonant wind velocity (Figure 3-7(c)), the torsional displacement again shows considerable random modulation. Thus, in presenting results for the torsional mode, it is important to record the maximum as well as the mean amplitudes of oscillation, since the peak displacement may be many times the average level.

Vortex resonance amplitude results for the 1 in. and 3 in. angle models at various orientations, damping levels and support conditions are summarized in Figures 3-8 through 3-11. The horizontal dotted lines at $\overline{Y} = 0.70$ and $\overline{\Theta} = 0.14$ indicate the limits of the mounting systems. Figure 3-8 illustrates the plunging amplitude-velocity results at the symmetrical angle of attack of -45°. The plots indicate the presence of combined vortex resonance and galloping excitation, and the effect of damping on the two types of instability. An increase in damping or decrease in model size (i.e., mass parameter) effectively shifts the entire galloping curve to the right on the velocity axis together with a reduction in vortex resonant amplitude. For the lower damping levels, the amplitude became very large exceeding the limiting displacement attainable with the lateral system. Of course, the angle section exhibits

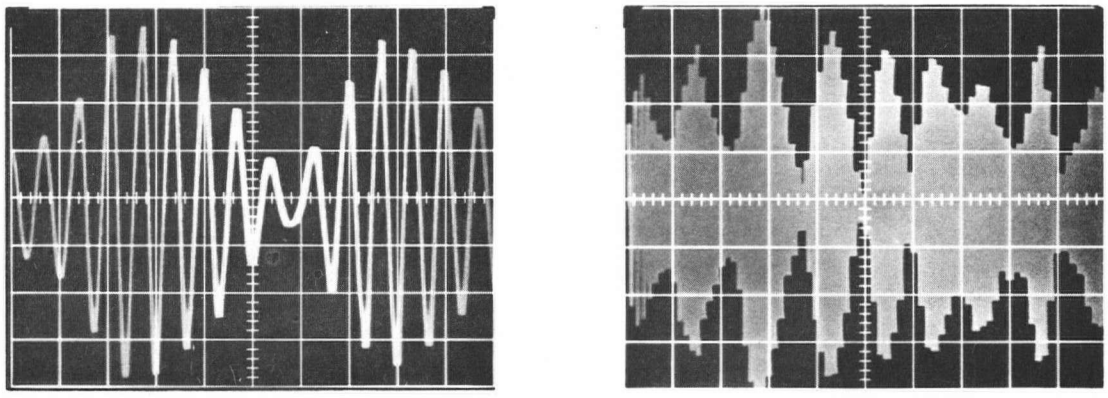

(a)

$(U_\theta/U_{res}=0.840)$

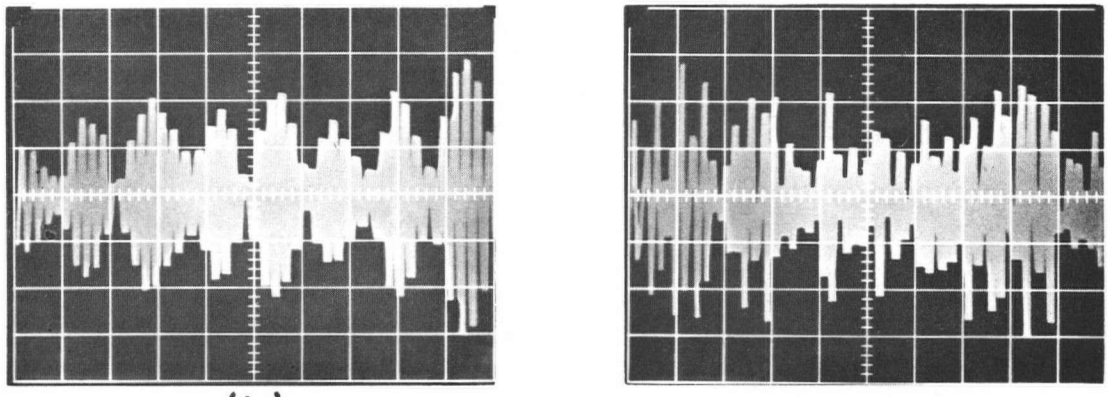

(b)

$(U_\theta/U_{res}=1.16)$

(c)

$(U_\theta/U_{res}=1.45)$

Figure 3-7 Typical torsional displacement signals for angle model experiencing vortex excited motion at various wind speeds near resonance

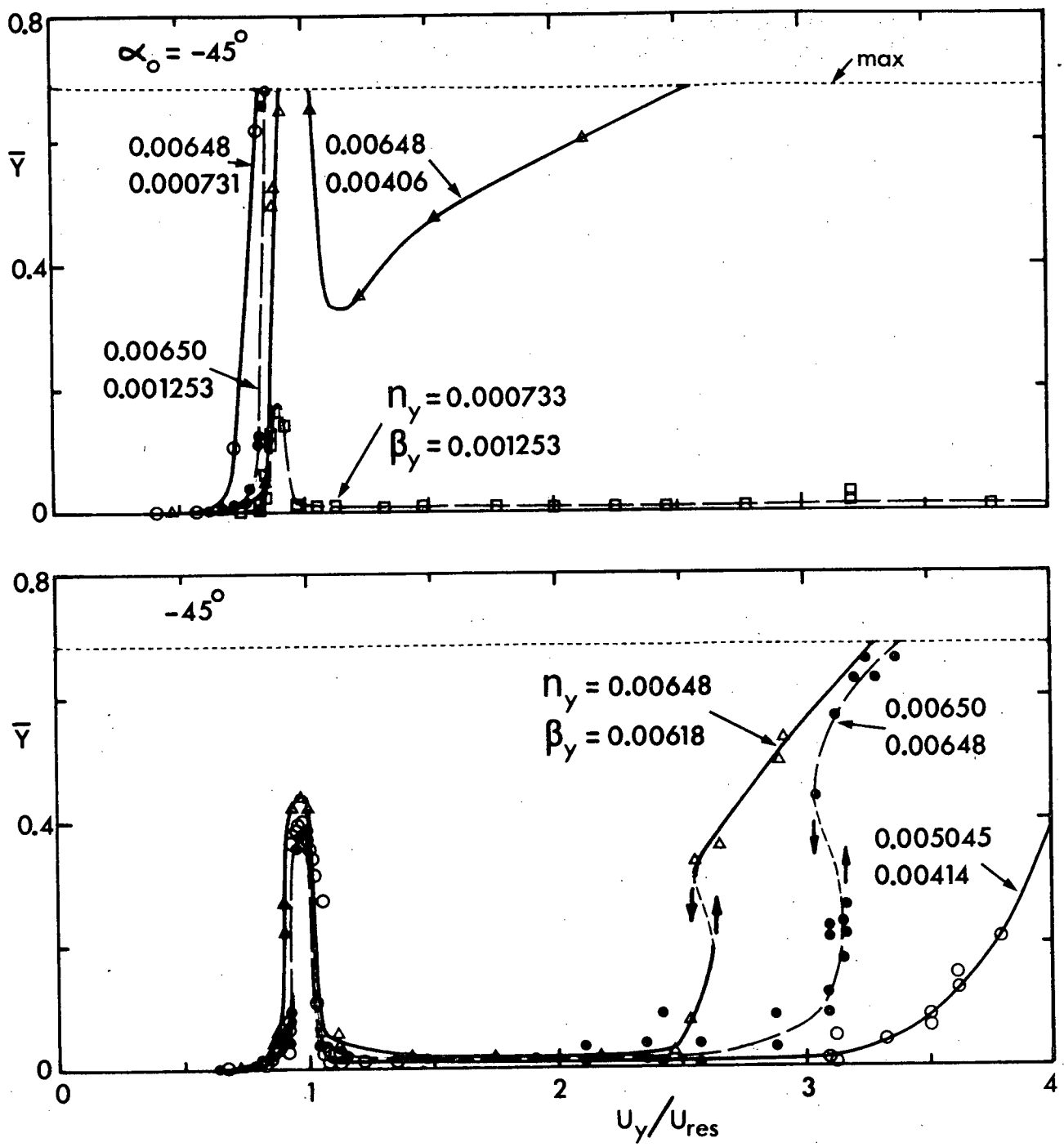

Figure 3-8 Separation of vortex resonance and galloping type of oscillation by choice of damping or mass parameter for $\alpha_o = -45°$

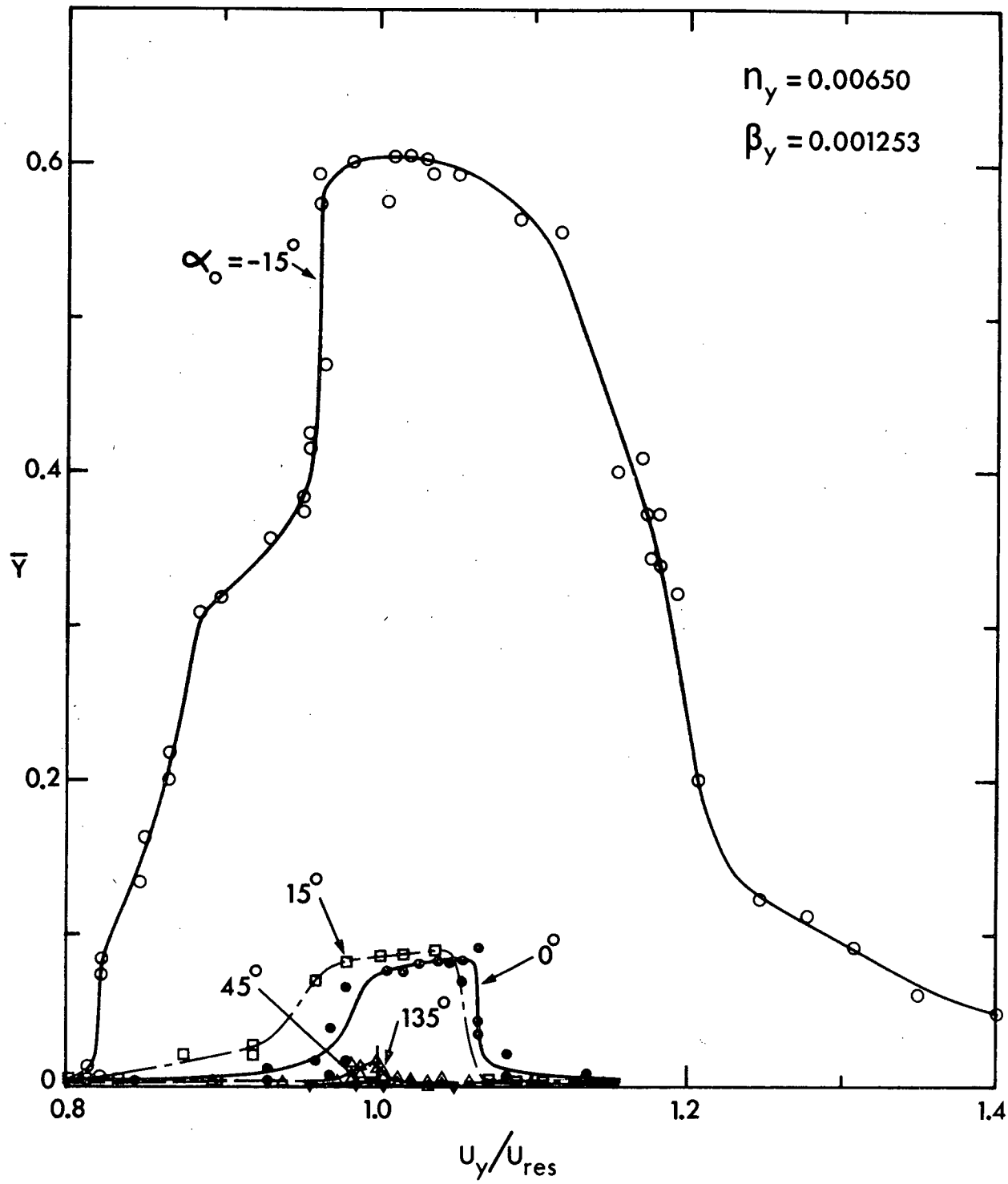

Figure 3-9 Plunging resonant curves for 3 in. angle model at various orientations

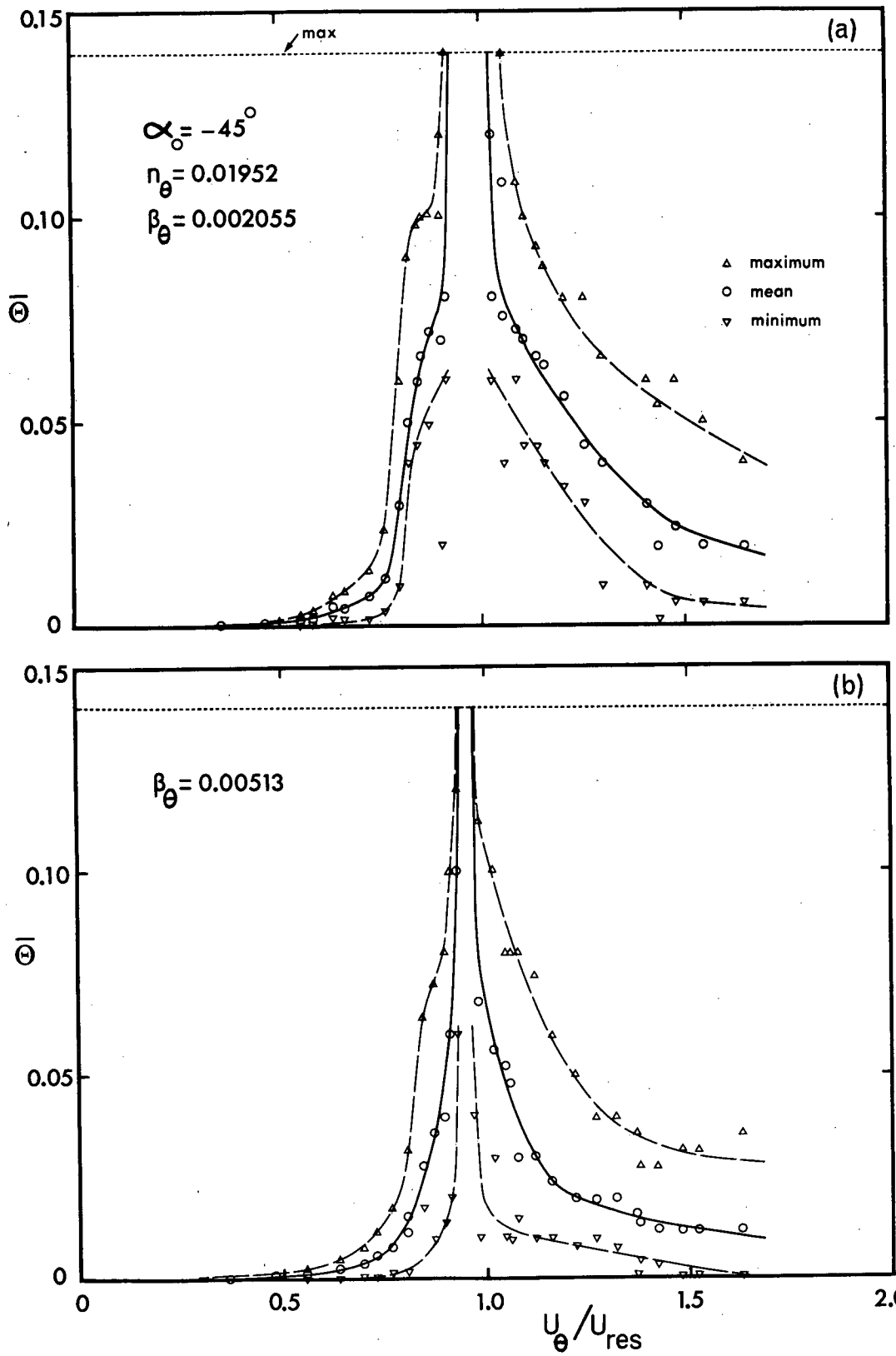

Figure 3-10 Torsional resonant curves for 3 in. angle model at α_o = -45° with axis of rotation at shear centre

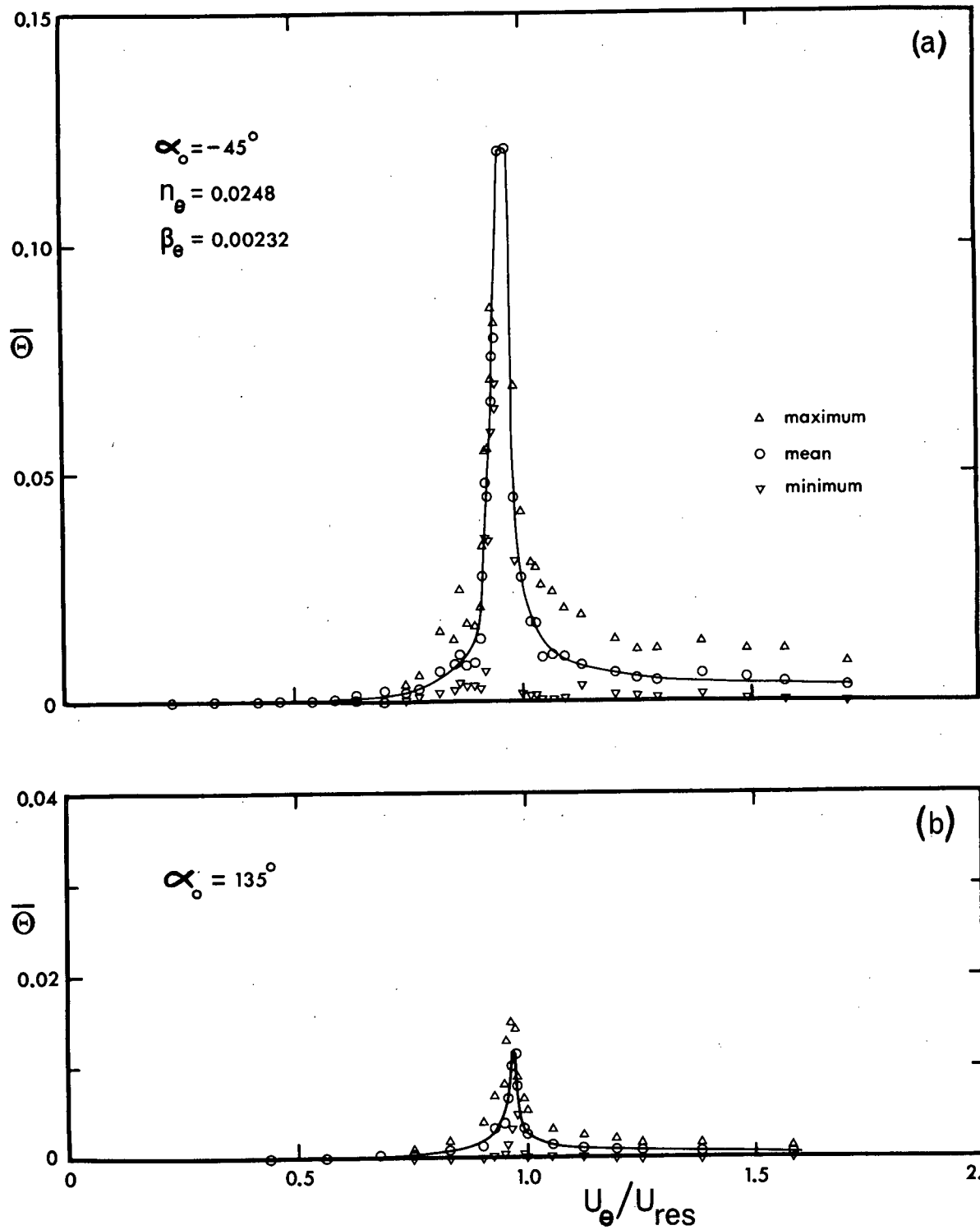

Figure 3-11 Torsional resonant curves for 3 in. angle model at $\alpha_o = -45°$ and 135° with axis of rotation at centre of gravity

vortex resonance at other orientations as well (Figure 3-9) but the results show the peak displacements in these cases may be small even at low damping. Being directly related to the forcing function, the peak amplitudes vary with attitude in a manner similar to the unsteady aerodynamic characteristics for the stationary model (Figure 2-18(a)).

Besides the modulation characteristic, the torsional amplitude-velocity results in Figures 3-10 and 3-11 indicate the severity of the resonant condition at $\alpha_o = -45°$ with the presence of a significantly sharp peak even at moderate damping levels. Furthermore, the displacement curves may be spread over a relatively large velocity range as compared to the plunging case, suggesting a possibility for the torsional resonance to be critical. From the data given in Figure 3-10, it is apparent that the torsional displacement decreases with increased damping, which is typical of a resonant condition. Transfer of the axis of rotation from the shear center (Figure 3-10) to the centre of gravity (Figure 3-11(a)) has considerable influence on the dynamics of the system. The substantial decrease in amplitude is a direct consequence of a reduction in the fluctuating moment coefficient accompanying such a transfer. The occurrence of the small amplitude oscillations at $\alpha_o = 135°$ (Figure 3-11(b)) is associated with a similar variation of the unsteady forcing function with angle of attack as observed during the stationary model measurements (Figure 2-18(c)).

The influence of the mass and damping parameters on the vortex resonance can be summarized in the form of a stability diagram.[22] Figures 3-12 and 3-13 illustrate such plots for the

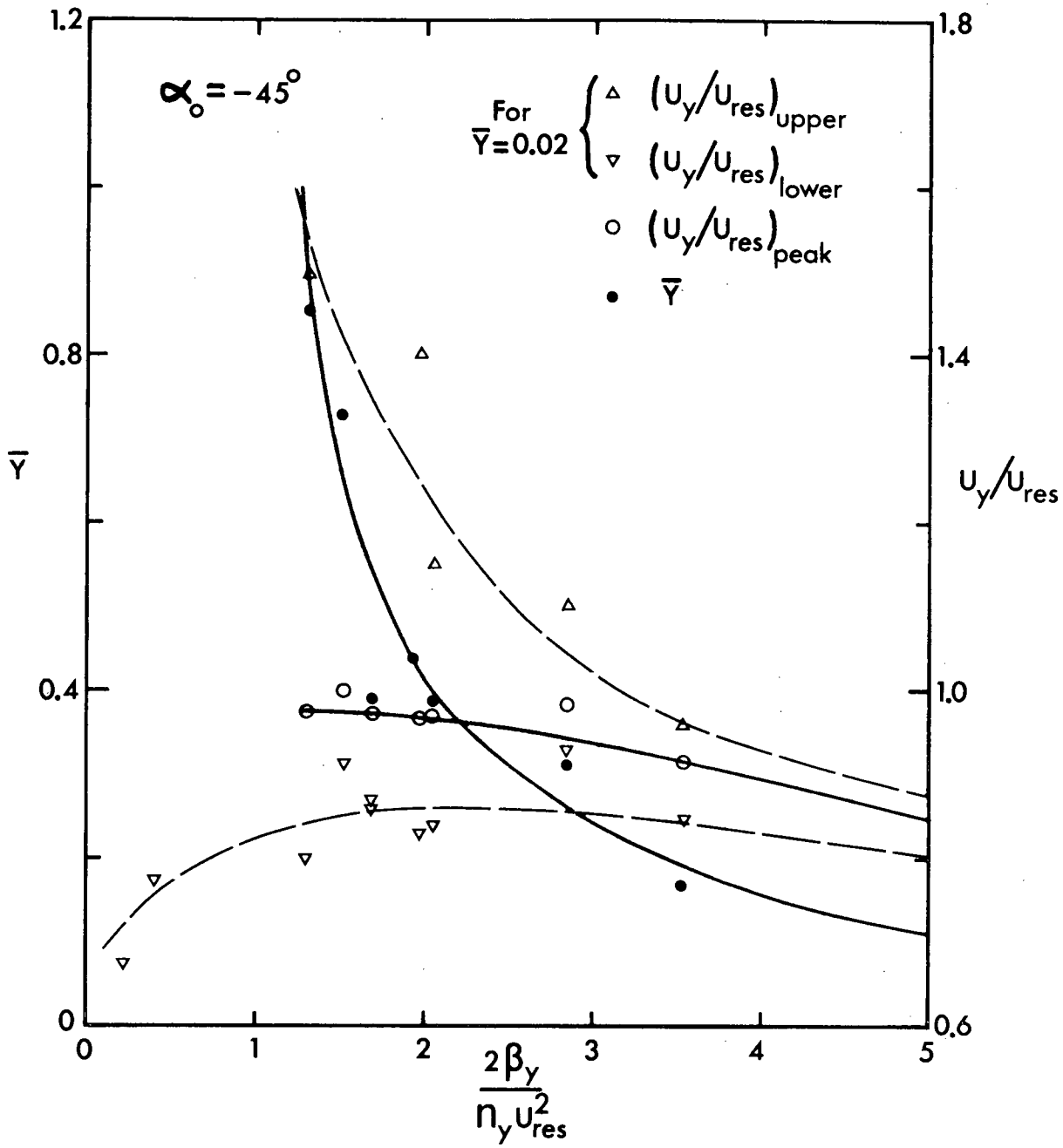

Figure 3-12 Stability diagram for 3 in. angle model experiencing vortex excited plunging motion at $\alpha_o = -45°$

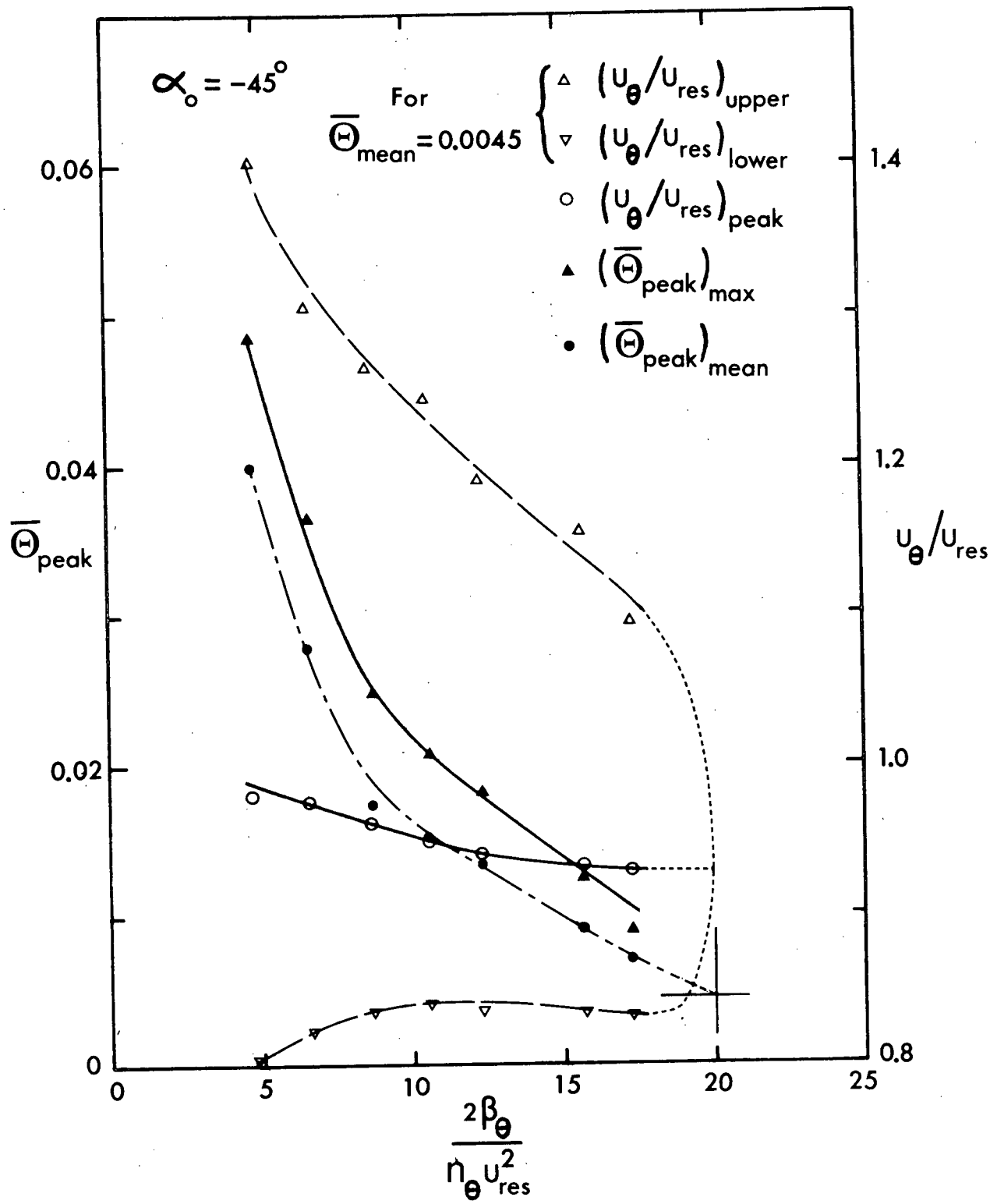

Figure 3-13 Stability diagram for 3 in. angle model experiencing vortex excited torsional motion at $\alpha_o = -45°$ with axis of rotation at shear centre

3 in. angle section at $\alpha_o = -45°$ for the plunging and torsional degrees of freedom, respectively. The graphs show the variation of the peak amplitude and corresponding wind speed, as well as the upper and lower velocity bounds for some limiting, permissible displacement. Reduction of the instability domain with increasing damping or decreasing mass parameter is apparent. As the mass parameter is directly proportional to the model size, a smaller angle section will effectively reduce the resonant vibrations. The dotted portions of the curves in Figure 3-13 extended to $2\beta_\theta/n_\theta U_{res}^2 = 20$ were obtained by projecting the mean peak displacement to $\bar{\Theta} = 0.0045$ representing the value for which the velocity bounds were determined. Furthermore, the upper and lower limits should meet at the resonant peak velocity. Hence, for values of $2\beta_\theta/n_\theta U_{res}^2 > 20$, torsional resonance will be virtually non-existent. It should be noted, however, that a substantial amount of damping is required to reach this condition. For the given set of data, a β_θ value greater than 8% of the critical damping was necessary with an inertia parameter of 0.01 which is representative of 3 in. structural aluminum angles. Thus, the investigation suggests that the torsional mode is likely to be critical and may lead to failure of the structure.

3.5.1.2 Surface Pressure and Wake Characteristics Associated with Oscillating Angle Model

To understand the influence of the resonant motion on the fundamental parameters, such as the shedding properties of the vortices, resulting unsteady surface pressures and wake geometry, measurements were conducted with the pressure tap

angle model at $\alpha_o = -45°$ over the wind speed range conducive to this form of instability.

Figures 3-14 and 3-15 present these results for the plunging and torsional degrees of freedom, respectively. For the plunging case, the graph illustrates the phenomenon of vortex capture where the frequency of the shedding vortices is controlled by the cylinder oscillations over a finite range of wind velocity around the resonant value. Above and below this capture region the vortex frequency tends to follow the Strouhal value obtained from stationary model tests. The cylinder frequency generally remains close to the natural frequency of the undamped system. For the torsional mode, however, the vortex formation dominates the cylinder frequency over a large velocity range with the frequencies closely following the Strouhal curve. This torsional phenomenon, in contrast to vortex capture, is denoted as vortex control. However, for $U/U_{res} > 1.2$, there develops a division of the cylinder frequency into two branches each having distinctly different periods of oscillation. Branch 1, following the vortex shedding frequency, corresponds to small amplitude displacements occurring during motion build-up or decay. For the large amplitudes, the frequency of oscillations approaches the torsional natural frequency, f_{n_θ}, thus momentarily destroying the phenomenon of vortex control. It appears that vortex shedding initiates the torsional vibrations which build up with the input of energy, but larger amplitudes cause loss of vortex control leading finally to the diminishing of the oscillations. This explains the highly modulated displacement signals obtained

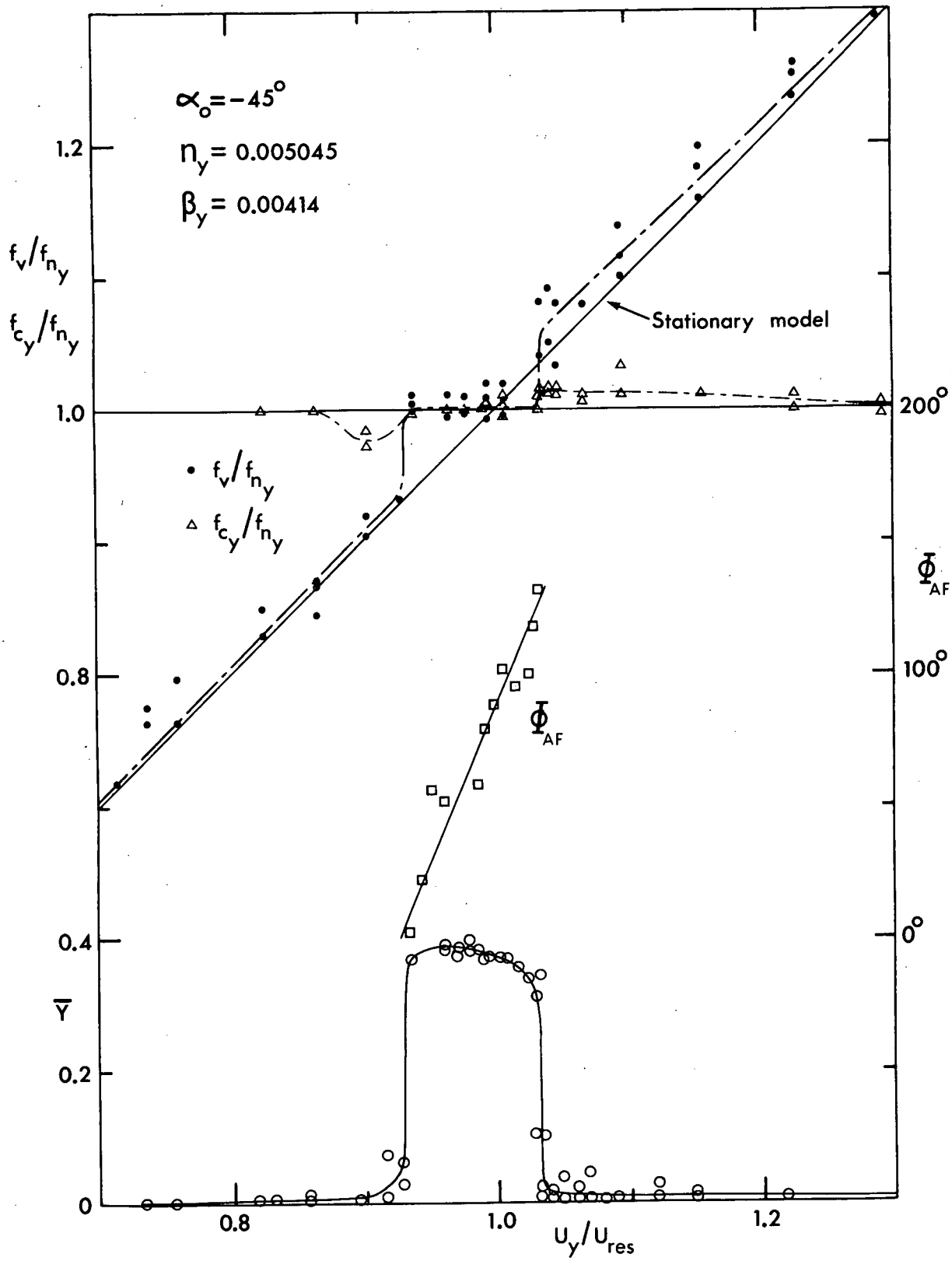

Figure 3-14 Variation of cylinder and vortex shedding frequencies, phase, and displacement amplitude near resonance (α_o = -45°)

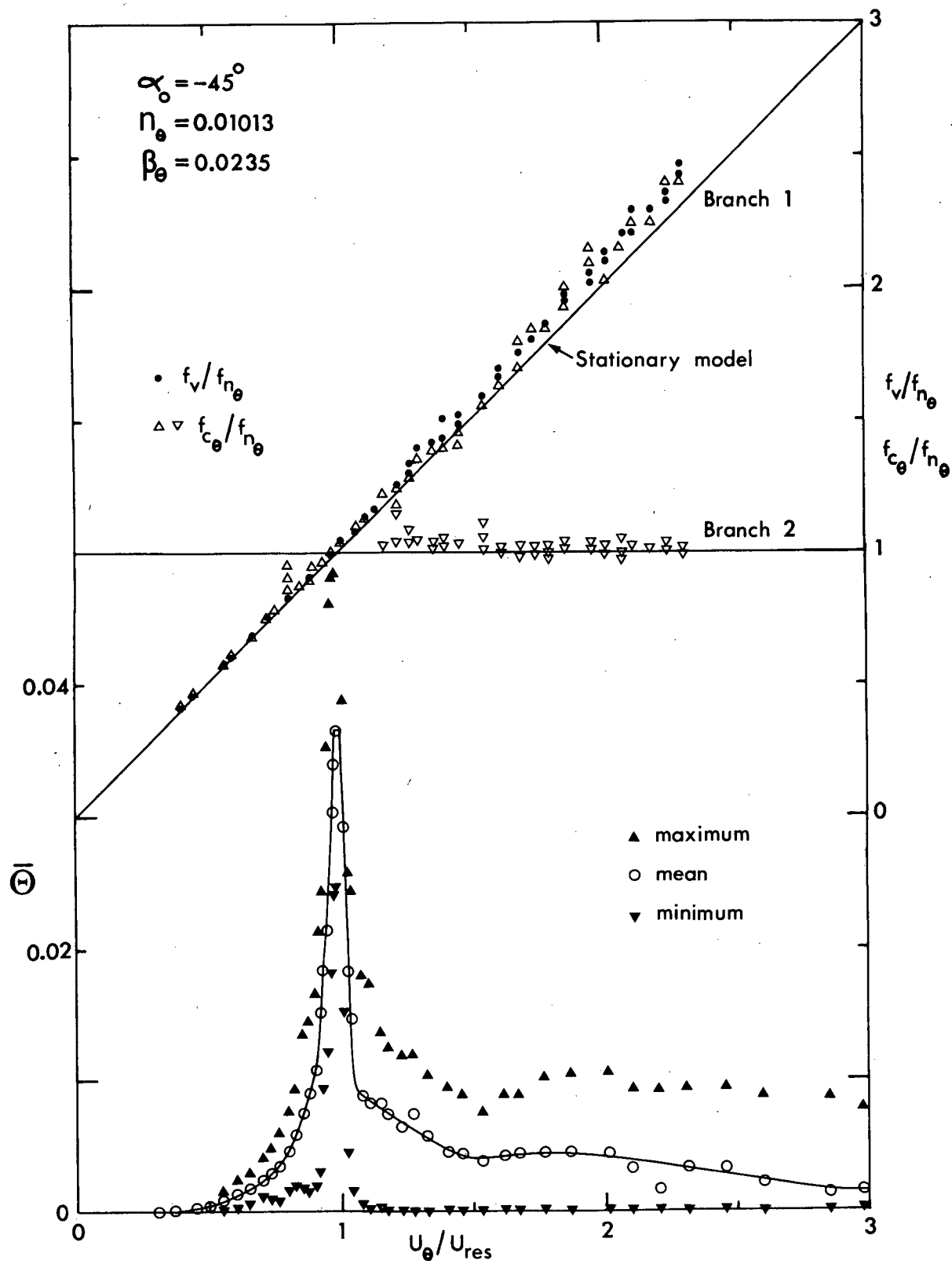

Figure 3-15-i Variation of cylinder and vortex shedding characteristics with wind speed for $\alpha_o = -45°$ (torsional amplitude, and frequency results)

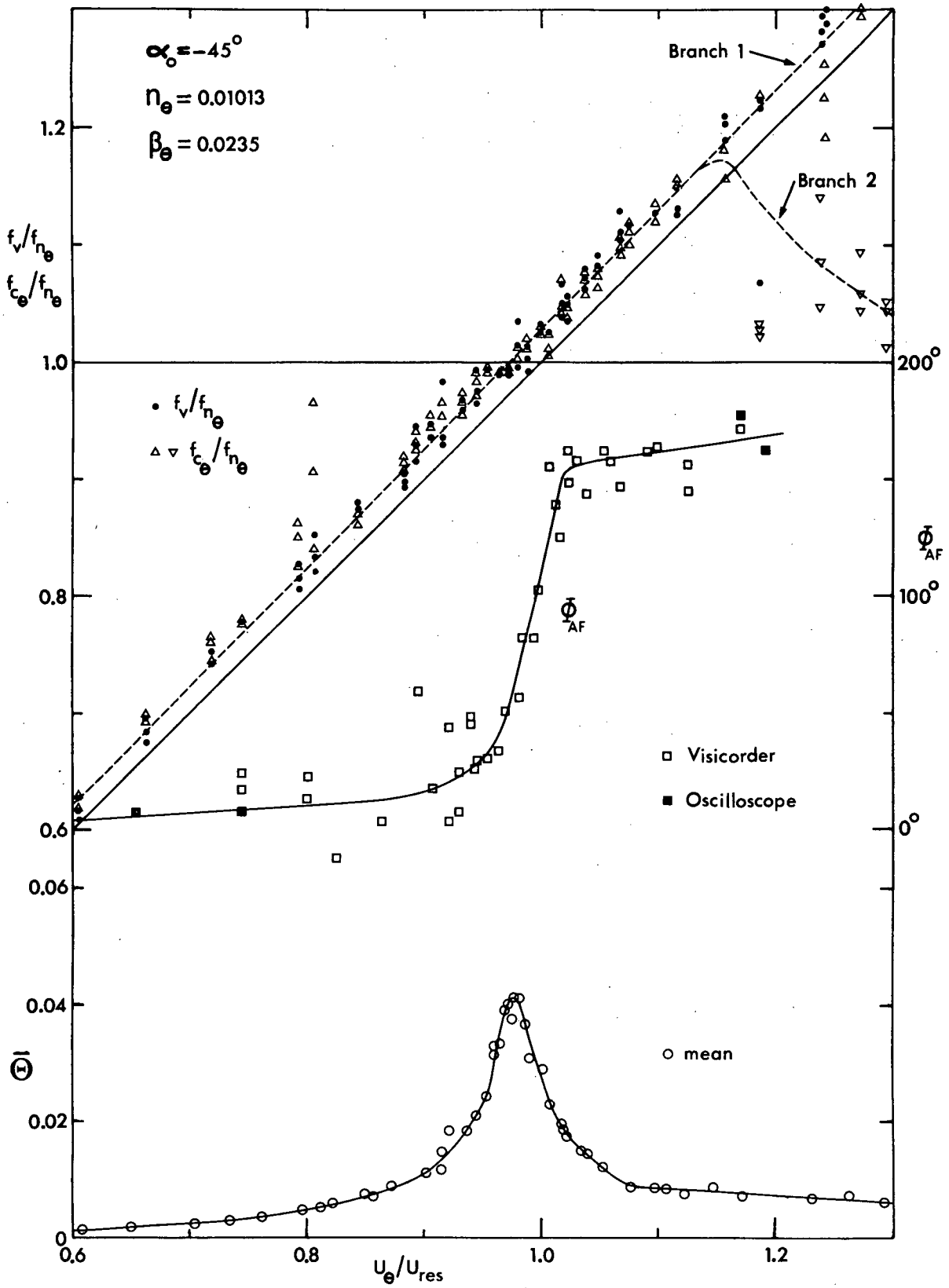

Figure 3-15-ii Variation of cylinder and vortex shedding characteristics with wind speed for α_o = -45° (frequency, phase and mean torsional amplitude near resonance)

for wind speeds well above U_{res} as shown by the sample trace in Figure 3-7(c). The distribution of the phase lag between the motion and the forcing function varying from nearly in-phase at the beginning of resonance and approaching 180° when above U_{res}, is typical of a linear, damped, oscillator experiencing forced harmonic vibration. The control of the torsional cylinder frequency by the vortex excitation is consistent with the mathematical model, but the theory fails to predict the plunging vortex capture phenomenon.

The effect of model dynamics on the fluctuating surface pressures was studied at the wind velocity corresponding to peak amplitude for the angle section at $\alpha_o = -45°$. Figure 3-16 summarizes the midspan and spanwise distributions of the mean fluctuating pressure amplitude, modulation ratio and phase variations; and include, for comparison, the stationary model results. In both, the plunging and torsional degrees of freedom, the pressure coefficient is comparatively larger over the entire surface of the model. For the plunging case, the modulation ratio and phase variation are considerably less; while for the torsional mode, the results show only slight reduction. The spanwise variations of phase and amplitude are still present and have treads similar to the stationary model curves.

A final summary showing the influence of vortex resonance on the magnitude of the unsteady aerodynamic coefficients is given in Figure 3-17. For the torsional case, the unsteady lift and moment at the centre of gravity decrease from the large plunging values to almost the stationary model results. On the other hand, the fluctuating moment about the shear centre shows

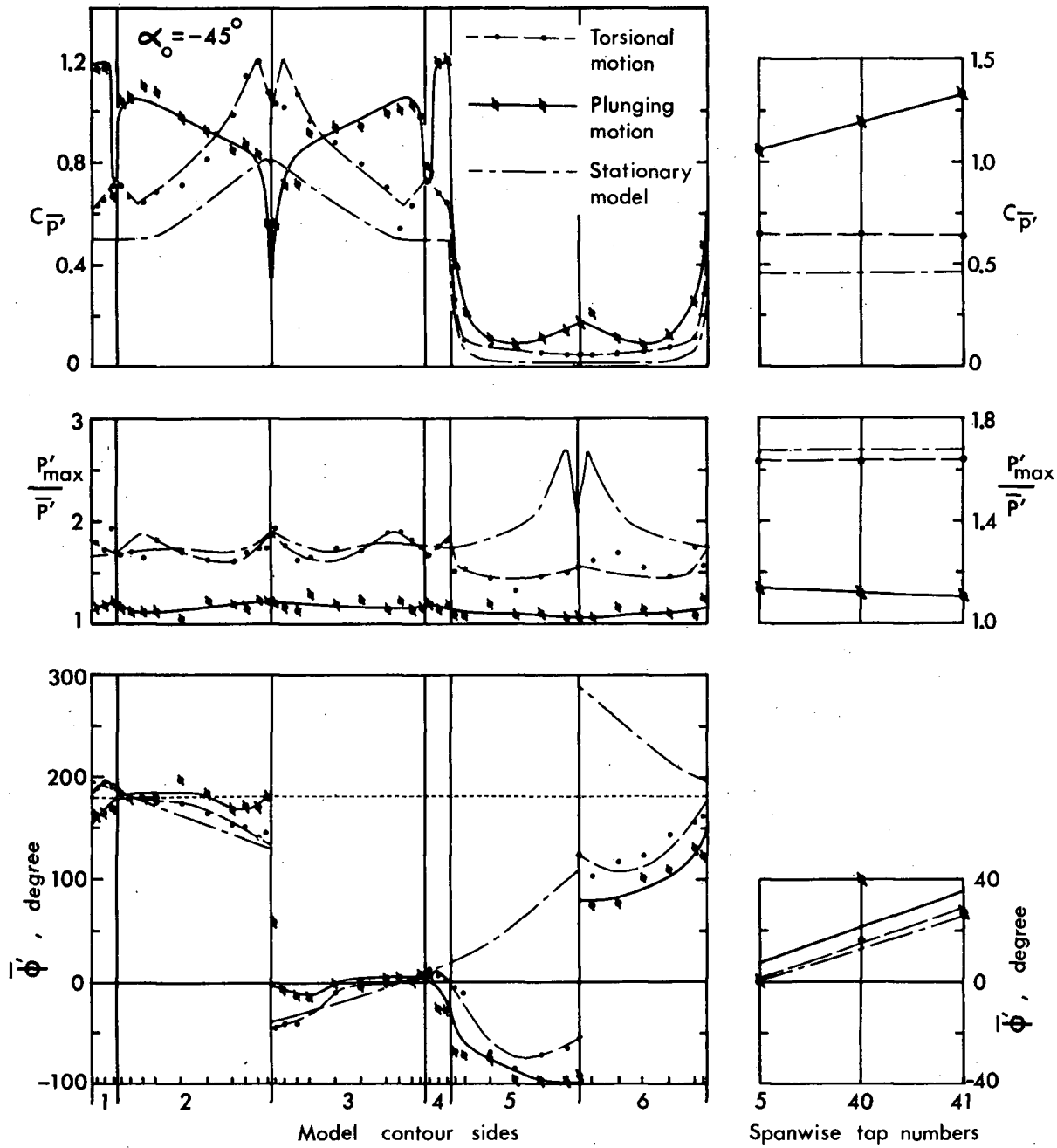

Figure 3-16 Midspan and spanwise distributions of fluctuating pressure coefficient, amplitude modulation ratio and phase during static and dynamic conditions of the model

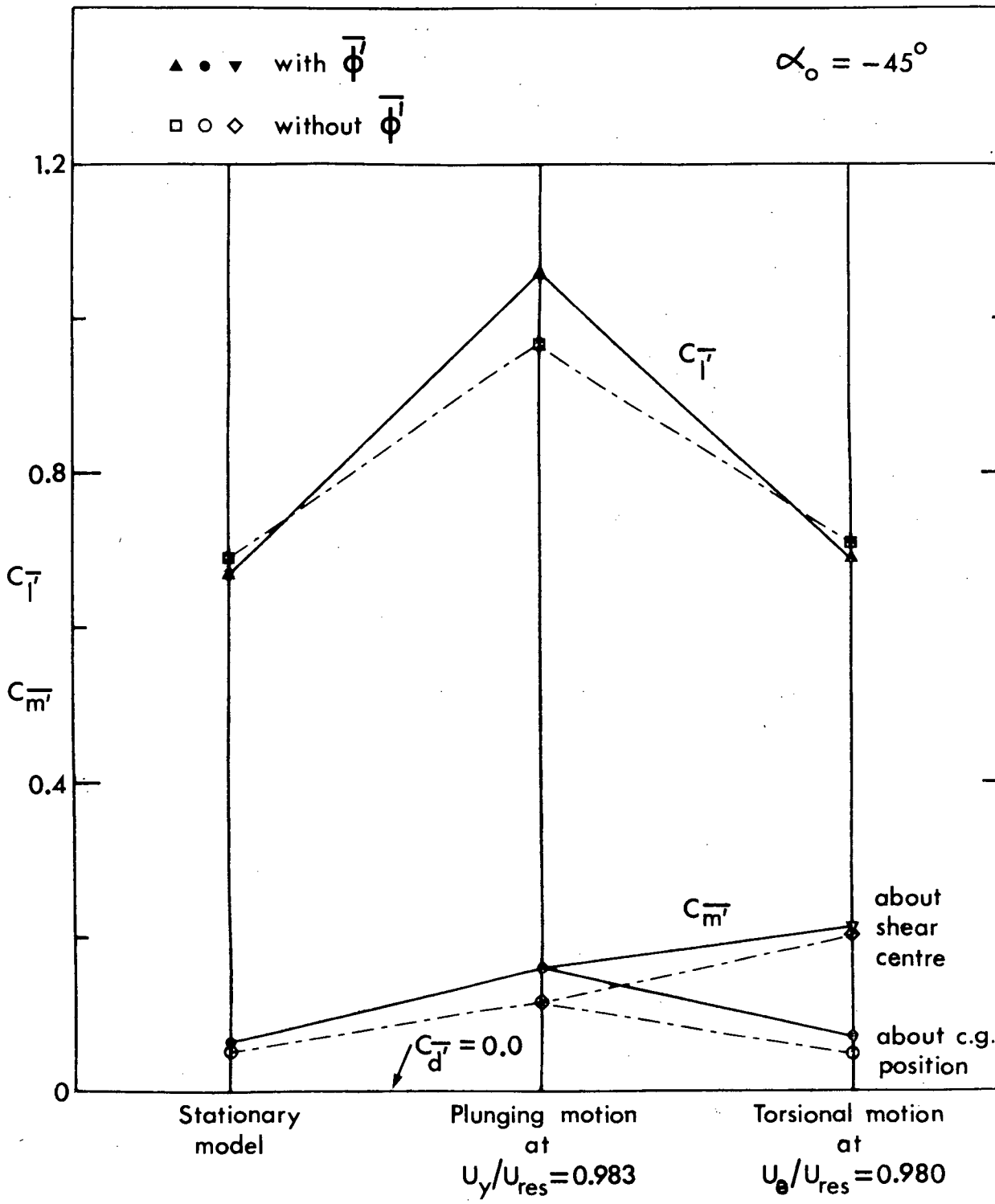

Figure 3-17 Comparison of fluctuating aerodynamic coefficients for stationary and vortex excited conditions of the angle model at $\alpha_o = -45°$

a substantial increase. This variation of pitching moment with axis position substantiates the observed difference in the peak amplitudes reported in Figures 3-10(a) and 3-11(a). At $\alpha_o = -45°$, the fundamental component of the fluctuating drag coefficient is zero for all cases. The effect of the midspan pressure phase on the aerodynamic coefficients compares with the 10% difference obtained for the stationary model (Figure 2-18).

Investigation of the wake geometry during peak plunging and torsional resonant conditions was performed using the pressure tap model oriented at $\alpha_o = -45°$. The fluctuating pressure distributions in the lateral and longitudinal directions (Figure 3-18) are similar in form to the stationary model measurements presented in Chapter 2. As a result, the plots of vortex velocity, and wake geometry with downstream coordinate (Figure 3-19) also show comparable trends although the limiting values may be different in magnitude. A summary of the 'near infinity' values for the angle section during static and dynamic conditions is shown in Figure 3-20. For the oscillating model, the longitudinal spacing and vortex velocity remain essentially unchanged. On the other hand, it is apparent that the lateral spacing of the vortex rows experiences substantial increase during plunging resonance. There is a simultaneous increase in the spacing ratio as well. Nevertheless, an interesting feature becomes apparent if the plunging displacement is used in conjunction with the model frontal width when nondimensionalizing the row spacing. By taking the effective blockage to equal $(2\bar{y} + h)$, the lateral spacing paremeter reduces to almost the same value as the stationary or torsional model result, thus suggesting

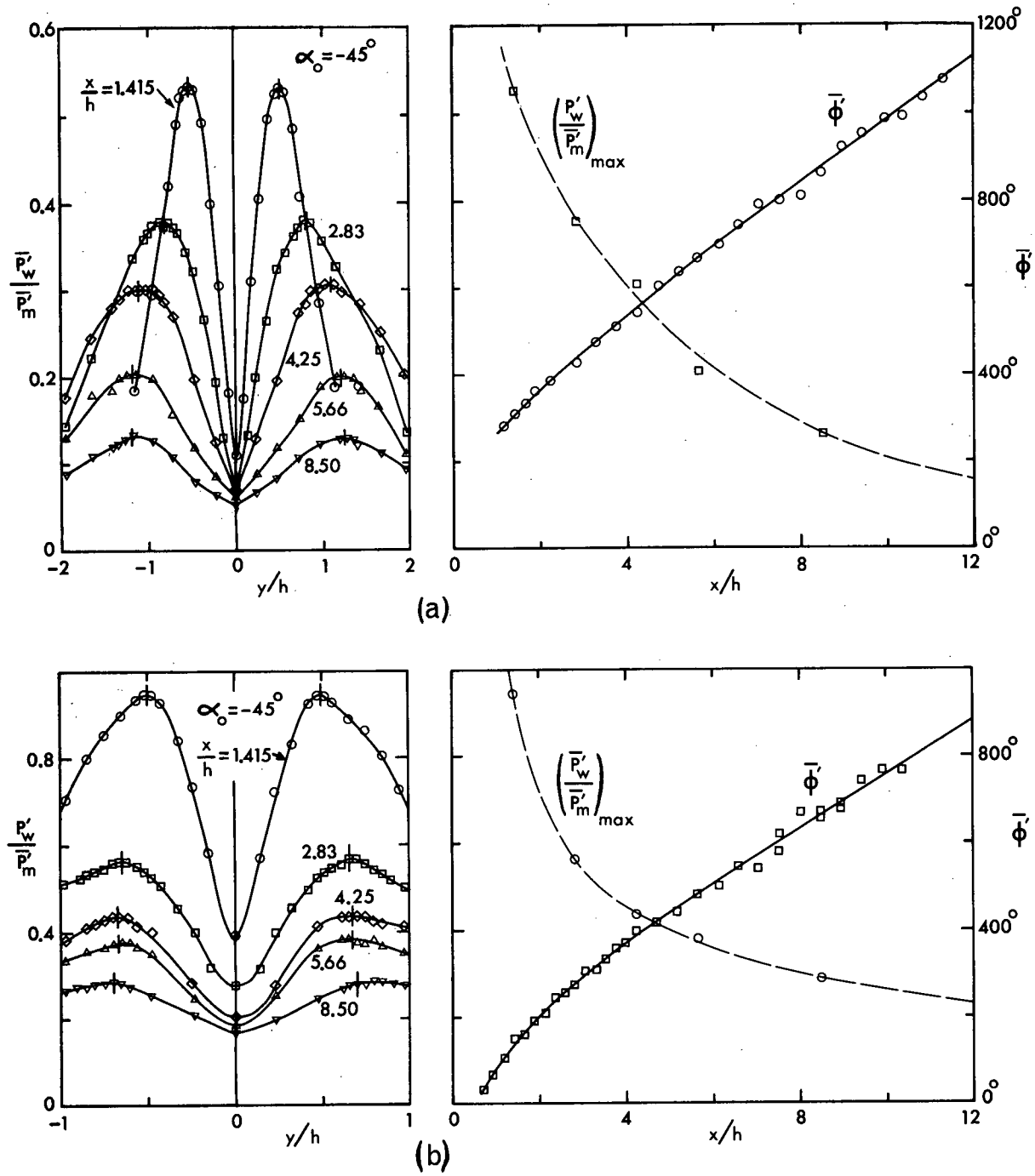

Figure 3-18 Variation of amplitude and phase of fluctuating pressure in wake of angle model experiencing vortex excited motion at α_o = -45°
(a) plunging (b) torsion

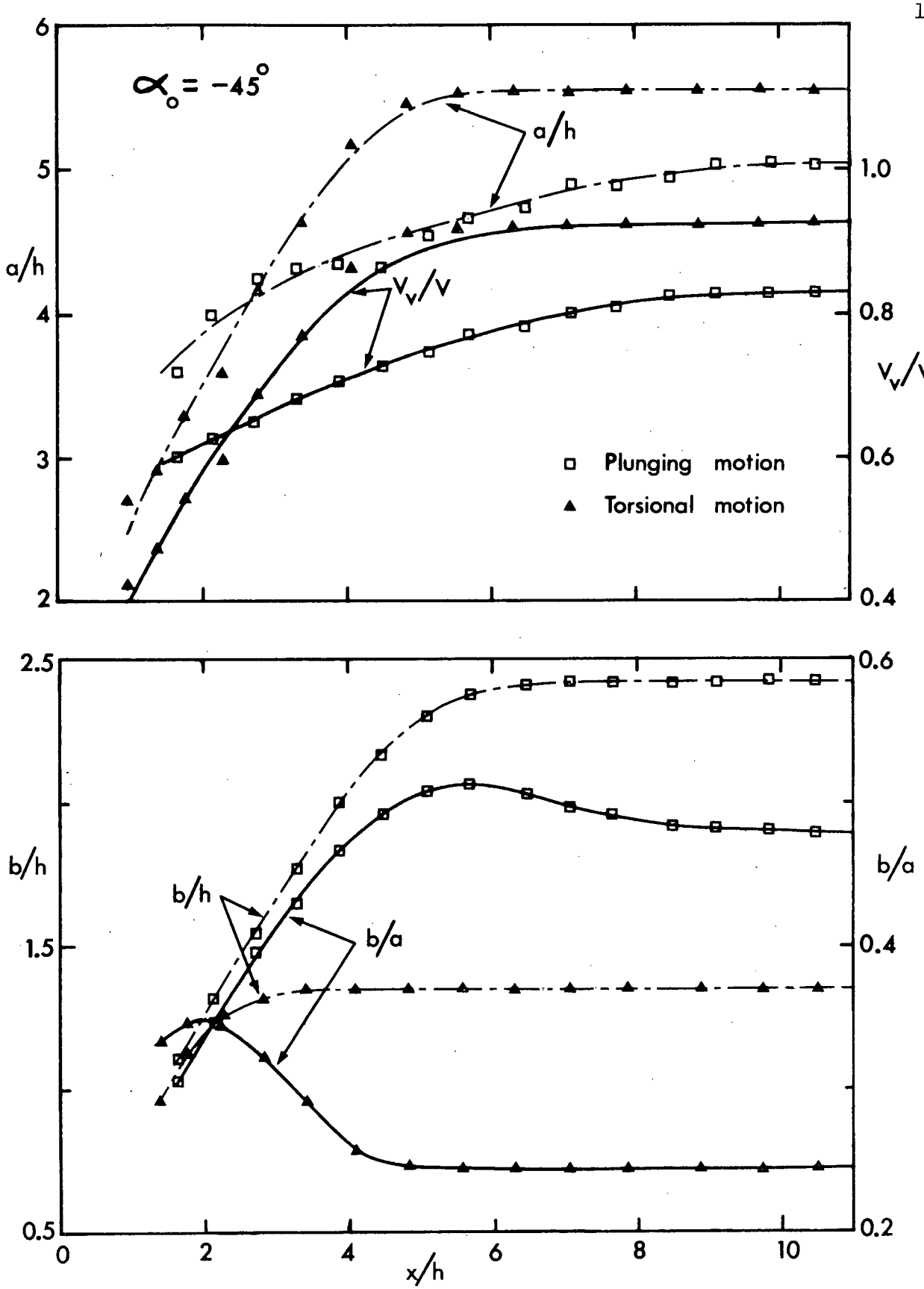

Figure 3-19 Longitudinal variation of wake survey parameters for plunging and torsional conditions of model at $\alpha_o = -45°$

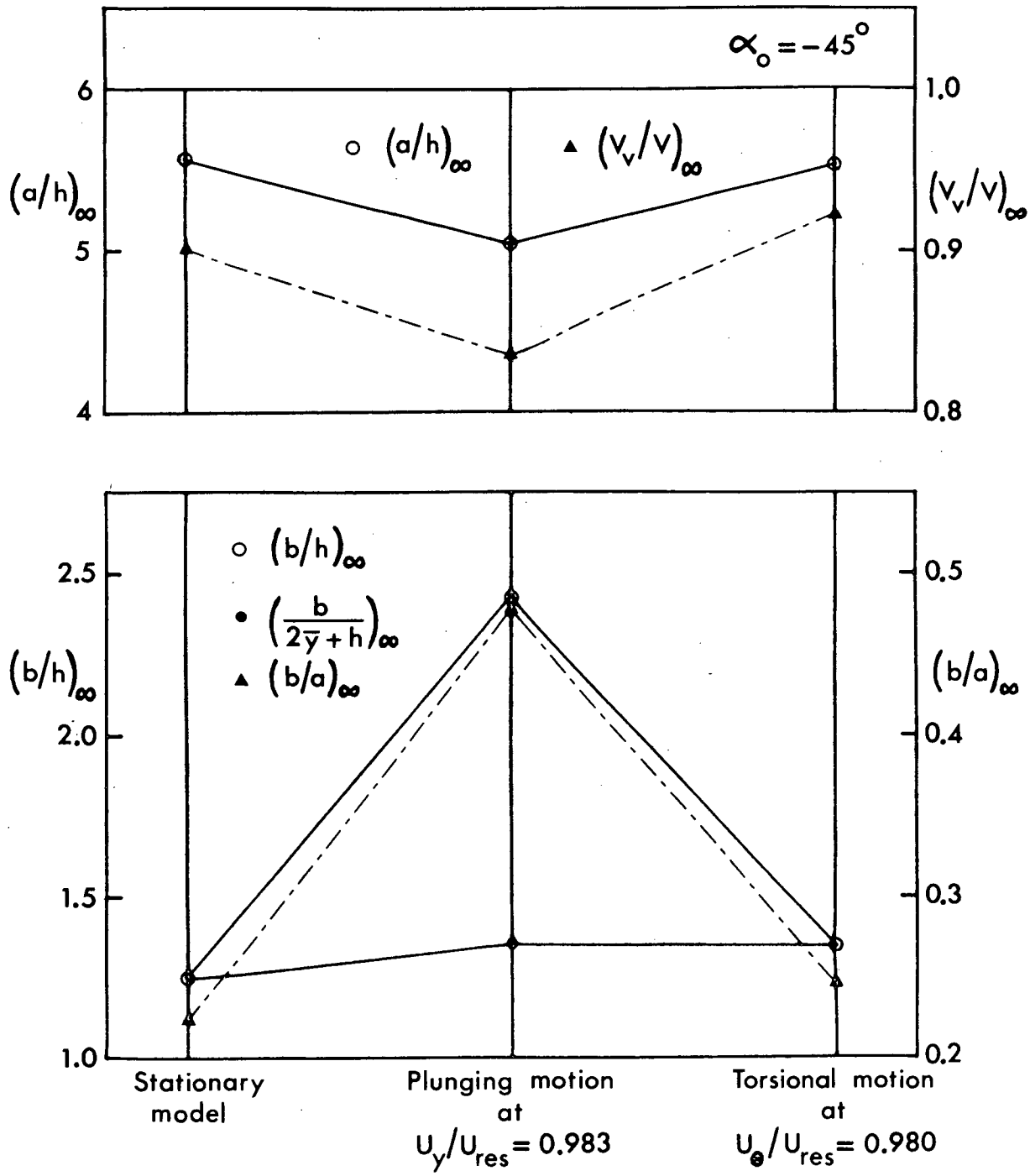

Figure 3=20 Comparison of 'near infinity' values of the wake survey parameters for stationary and vortex excited conditions of the angle model at $\alpha_o = -45^\circ$

that the increase in wake width is effectively caused by the amplitude of the plunging oscillations.

In summary, the wake survey and vortex shedding frequency investigations indicate that the torsional motion of the angle section has virtually no effect on the vortex shedding frequency and wake characteristics. This is in contrast to the pronounced enlargement of the wake width and vortex capture phenomenon which occurs with the plunging resonant motion. It should be noted that these limited results for the fluctuating pressure and wake geometry may not be entirely representative of what may occur at other wind speeds and damping conditions. Ferguson,[33] Feng[47] and Parkinson, et al,[74] during tests on circular and D-section cylinders, observed decrease of the pressure and wake parameters near the resonant peak. The parameters also depended on the magnitude of the oscillations controlled by the damping level. Similar behaviour is anticipated for the angle section where, like the D-section, separation is controlled by the edge geometry.

3.5.1.3 Resonant Theory Predictions

The applicability of the analytical models can be tested by comparing the theoretically predicted and experimentally measured values. However, it may be pointed out that since experimental data is incorporated in the theoretical calculations, the final validity of the analytical solutions rests partially on the accuracy of the experimental results. For example, consider the plunging motion of the angle section mounted at $\alpha_o = -45°$ (Figures 3-14 and 3-17). Here $\beta_y = 0.00414$. $n_y = 0.00505$,

$f_{c_y}/f_{n_y} = 1.00$, $U_y/U_{res} = 0.983$, $U_{res} = 0.986$, $\Phi_{AF} = 67°$, and $C_{\bar{l}'} = 1.057$. Therefore, from equations (3.6) and (3.7), $\bar{Y}_{max}$ = 0.63 and 0.55, respectively. Comparison with the experimental value of $\bar{Y}_{max} = 0.39$ indicates a closer agreement with the analytical solution developed by Parkinson, et al, since the vortex capture effects are incorporated. Note, however, the theoretical predictions are larger than the observed amplitude suggesting the influence of additional factors not included in the analytical considerations. It is anticipated that wind tunnel wall interference is one source of discrepancy, since the discussion in Appendix II indicates an increase in the unsteady force with flow confinement. Lack of spanwise correlation of the unsteady aerodynamics will also contribute to reduction in the experimental amplitude.

For the torsional mode, consider the data given in Figures 3-15-ii and 3-17. Here $\beta_\theta = 0.0235$, $n_\theta = 0.01013$, $f_{c_\theta}/f_{n_\theta} = 1.01$, $U_\theta/U_{res} = 0.980$, $U_{res} = 0.986$, $\Phi_{AF} = 66°$ and $C_{\bar{m}'} = 0.213$. Therefore, from equations analogous to (3.6) and (3.7), the peak displacements are $\bar{\Theta} = 0.045$ and 0.039, respectively. Good agreement with the experimental value of 0.041 substantiates the analyses.

3.5.2 Galloping Motion

3.5.2.1 Theoretical Predictions for Plunging Degree of Freedom

The application of the theoretical analysis to a physical system such as an angle section, for prediction of the galloping oscillations, requires aerodynamic force distributions at various

orientations as the input data. Knowledge of the model amplitude-velocity curves can be obtained from the calculation of the starting velocity U_o and the appropriate roots of the $\delta_y(\bar{Y})$ polynomial. Determination of the model build-up time versus velocity provides useful information concerning the severity of the galloping oscillations.

Using the accurately measured steady lift and drag distributions (Figure 2-7),the force curves at various α_o (Figure 3-21) were expressed as polynomials from which the amplitude-velocity curves were obtained. The analytical data is summarized in Figure 3-22 in the form of a three-dimensional graph of plunging amplitude $\bar{Y}$ as a function of U and α_o for a set of typical mass and damping parameters. The quasi-steady analysis predicts two large regions of instability with two smaller areas in between. For comparison, the vortex resonant velocity curve from Figure 2-10 is also included. It is apparent that there are regions in which the angle section is susceptible to pure vortex resonance together with areas of combined vortex and galloping oscillations. This phenomenon of combined excitations was confirmed by the experimental results given in Figure 3-8.

As shown by previous investigators,[17,50] the governing equation of motion can be transformed by introducing stretched or reduced variables $\bar{Y}^*$, U^*, τ^* to provide a universal solution where the results are independent of the system parameters n_y and β_y. The reduced amplitude-velocity curve initiates from the abscissa at U^* equal to unity. In addition, variation of the build-up time with velocity is only a function of the initial displacement $\bar{Y}_o^*$ when $\hat{Y}_j^*$ is taken to be 95% or some other con-

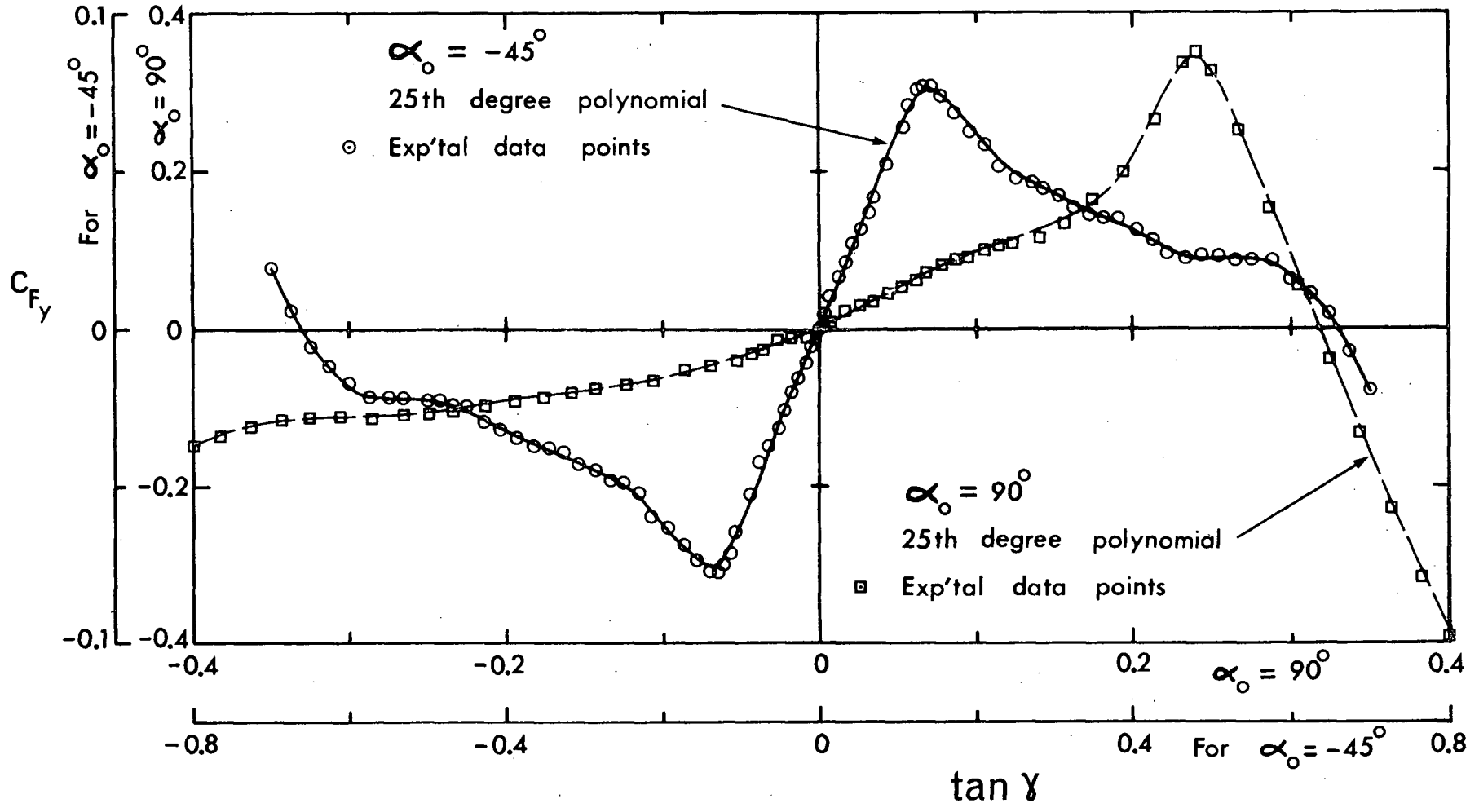

Figure 3-21 Polynomial curve fit of typical lateral force coefficient data

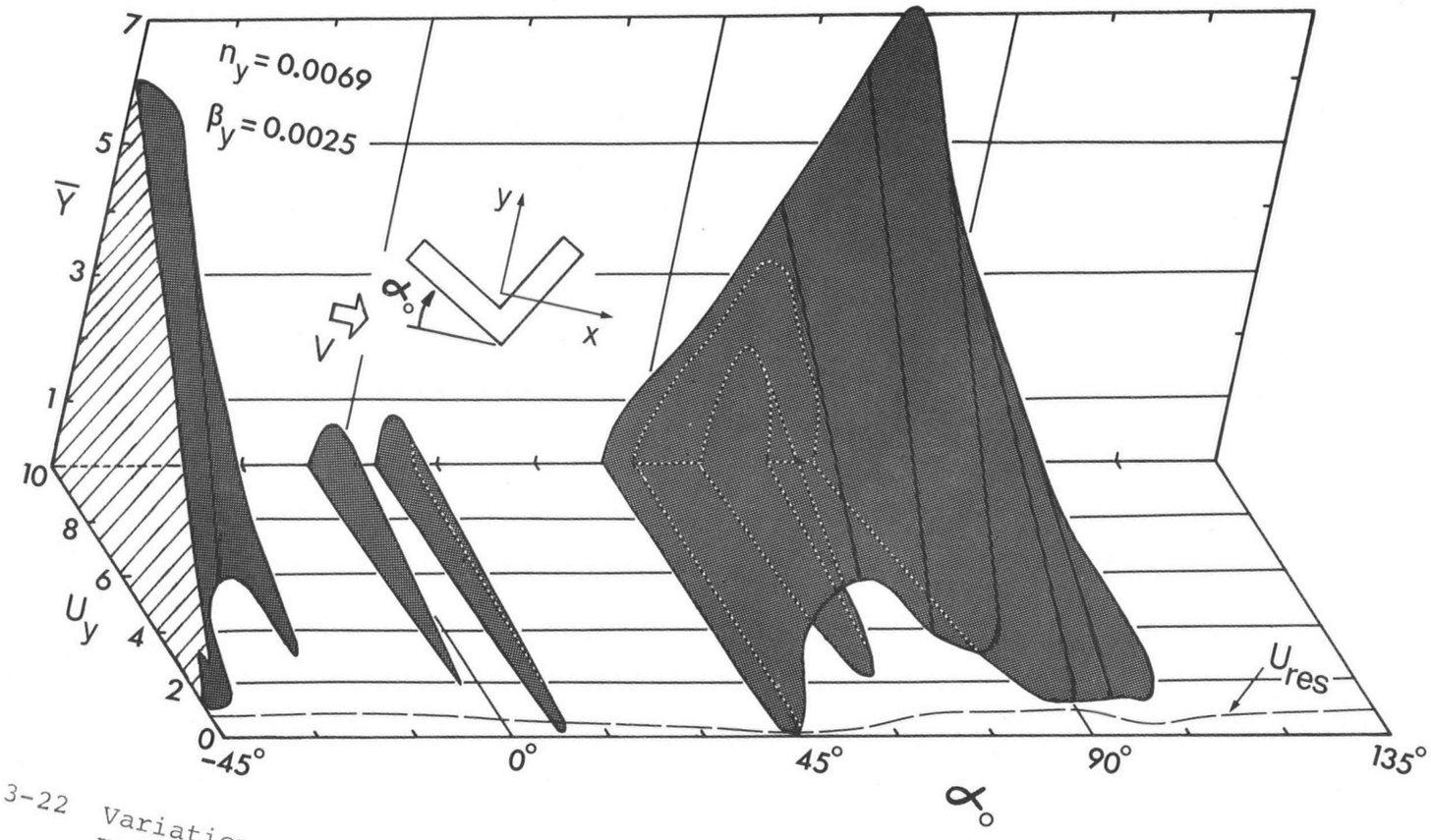

Figure 3-22 Variation of galloping plunging amplitude with wind velocity and model attitude as predicted by the quasi-steady theory

stant value of $\bar{Y}_j^*$. Comparison of the theoretical amplitude-velocity and build-up time curves with the experimentally obtained results is presented in the following section.

3.5.2.2 Plunging Amplitude and Build-up Time Measurements

Figures 3-23 and 3-24 summarize the amplitude-velocity data for the 1 in. angle model oriented at $\alpha_o = -45°$ and 90° with various damping levels. For comparison, the initial galloping results obtained with the 3 in. model at $\alpha_o = -45°$ (Figure 3-8) are included. Note that a smaller model extends the dimensionless velocity and amplitude ranges, besides separating the vortex and galloping instabilities. The experimental results at both orientations indicate the angle section to be a soft oscillator undergoing a discontinuous jump phenomenon. In addition, an increase in β_y or a reduction of n_y delays the initiation of galloping and has a tendency to shift the curves toward larger velocity and displacement values. Using the appropriate starting wind velocities, the results are also plotted in the form of reduced parameters. Collapsing of the experimental data to approximately the same distribution confirms the quasi-steady theory. A slight inconsistency at low $\bar{Y}^*$ is due to the difficulty in determining the exact starting velocity, and the presence of extraneous influences such as tunnel vibration, vortex shedding, and uncertainty of damping at small displacement and its minor fluctuations. The difference between the positions of the knee of the theoretical and measured curves may be attributed to slight inaccuracies in the steady force distribution near the origin and the corresponding polynomial representation used in the analysis.

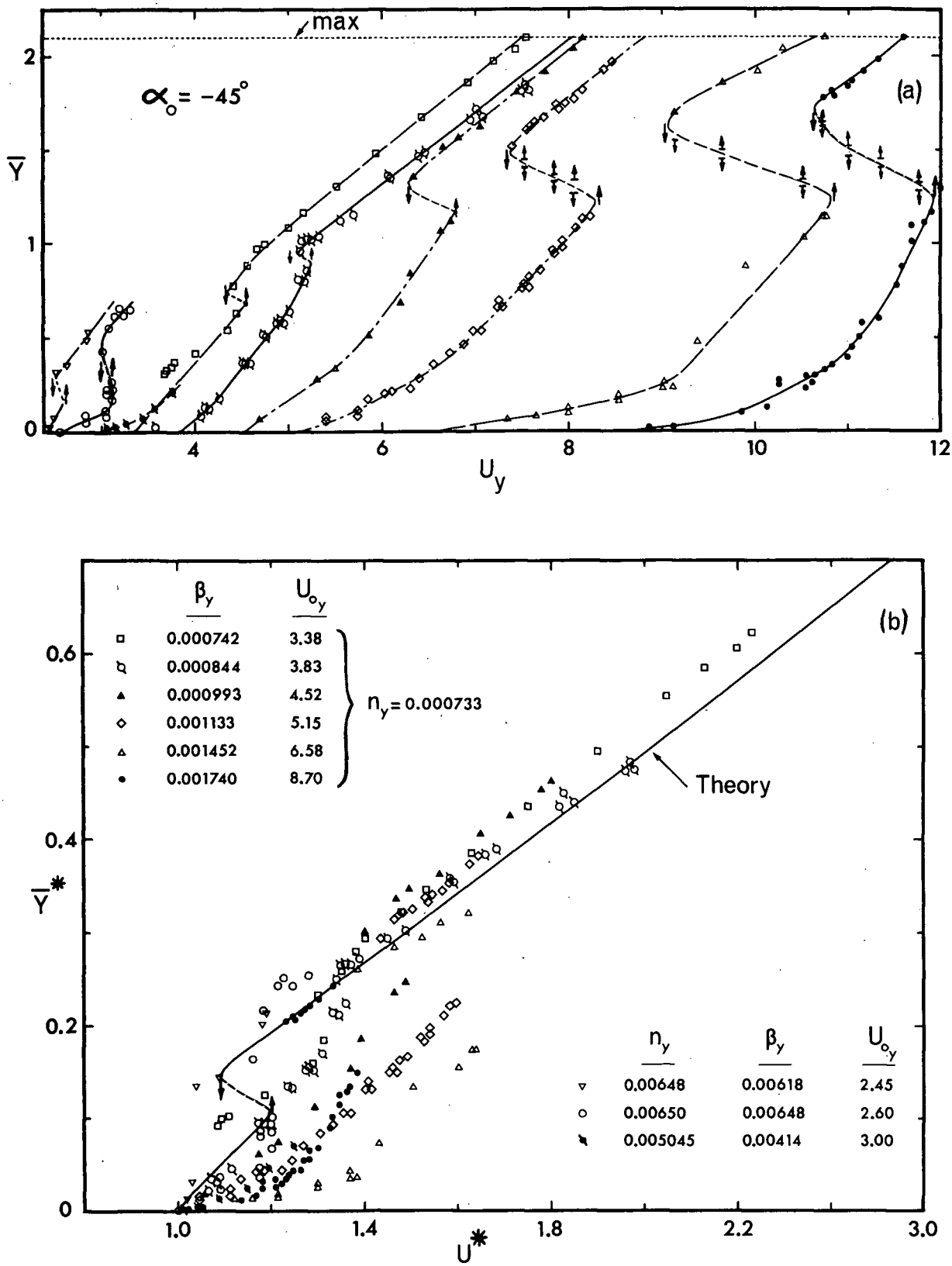

Figure 3-23 Galloping amplitude-velocity results for angle model at α_o = -45° and their comparison with theory

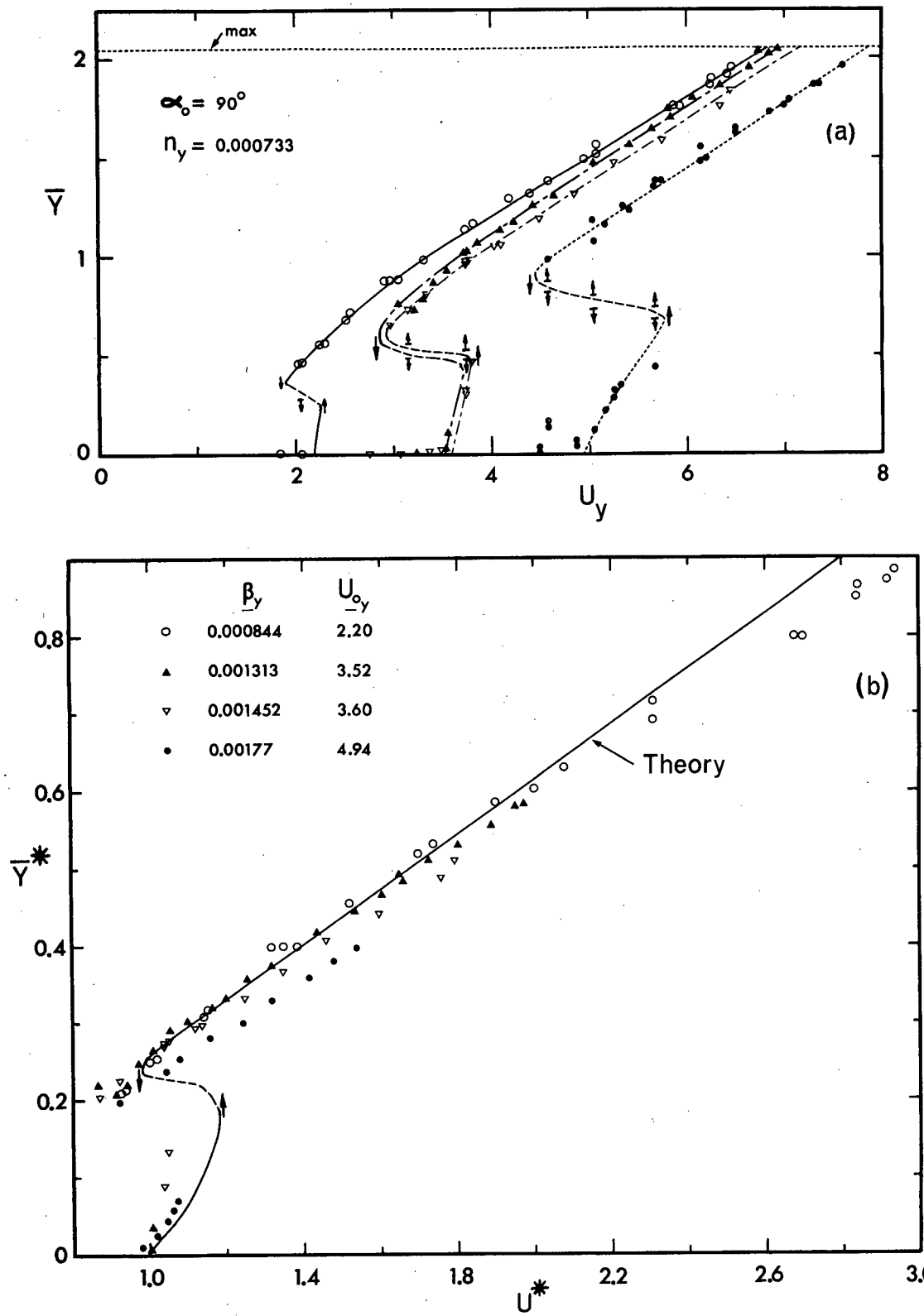

Figure 3-24 Galloping amplitude-velocity results for angle model at α_o = 90° and their comparison with theory

Further measurements were conducted at other angles of attack which generally confirmed the presence or absence of the galloping instability as predicted by the theory (Figure 3-22). One region of particular interest is the range $-15° \leq \alpha \leq 15°$ where the theory predicts two small zones of instability. The experiment substantiated the existence of the galloping motion over approximately the same range of angle of attack except that the amplitudes were slightly larger in magnitude and the two zones were connected together to form one continuous region.

The build-up time results for the 1 in. angle model at $\alpha_o = 90°$ are presented in Figure 3-25. The measurements were conducted at the damping levels used in the model amplitude investigations, and the initial displacements, $\bar{Y}_o$, were selected to give approximately the same value of the reduced variable $\bar{Y}_o^*$. Figure 3-25(a) shows an upward shift of the time-velocity curve with increasing β_y similar to that observed for the model amplitude characteristics. In the reduced time-velocity plot (Figure 3-25(b)), the data for the different damping levels collapse very nearly to one curve and compare well with the theoretical prediction. The lower value of the experimental results at small U* is due to the difference in position of the theoretical and experimental discontinuous jumps (Figure 3-24(b)). The scatter of build-up time data may be attributed to the slight differences in the corresponding amplitude results and the fact that the $\bar{Y}_o^*$ values are not identical for all β_y levels. The results, in general, indicate a monotonically decreasing build-up time with increasing velocity. Therefore, galloping oscillations are more severe at higher wind speeds since the time for build-

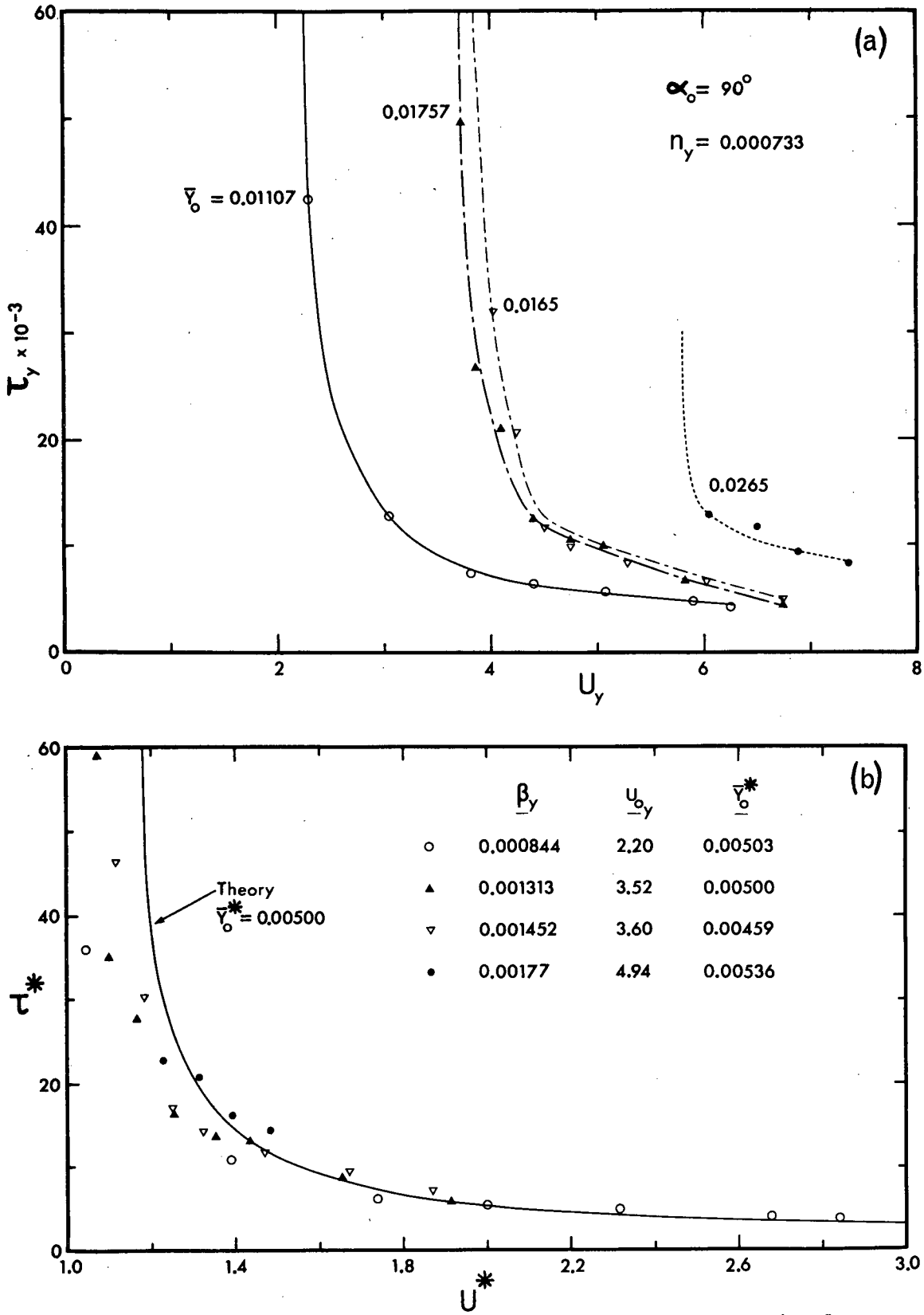

Figure 3-25 Comparison of experimental and theoretical amplitude build-up time for angle model at $\alpha_o = 90°$

up is shorter and the resulting displacement amplitude is larger.

3.5.2.3 Theoretical Predictions for Torsional Degree of Freedom

As discussed before in section 3.4.2.1, the stability analysis of the singularity predicts self-excited oscillations in the ranges $-45° \leq \alpha_o \leq 10°$ and $40° \leq \alpha_o \leq 60°$. However, for various orientations of the 1 in. and 3 in. angle models with a variety of damping and mounting configurations, no galloping instability in the torsional degree of freedom could be induced either from rest or with large initial amplitude. Extraneous vibration of the wind tunnel and model support system at high wind speeds limited the tests to a range below approximately 50 ft/sec.

The absence of the galloping oscillations can be explained using the quasi-steady theory. For example, the relevant portion of the steady aerodynamic moment distribution from the stationary model investigation (Figure 2-7) is replotted in Figure 3-26 for $\alpha_o = -45°$. Evaluation of the moment coefficient using equations given in Appendix IV gives a graph of $C_{M_\theta}(\Theta, \dot{\Theta})$ as shown in Figure 3-27. The representative curves are lines of constant C_{M_θ} which appear nearly linear and parallel, thus substantiating the simplification introduced by taking C_{M_θ} as a function of ξ. The resulting distribution of $C_{M_\theta}(\xi)$ is plotted in Figure 3-28 and approximated by a 17th degree polynomial. Only the positive values of ξ are shown since the moment is symmetric about the origin for $\alpha_o = -45°$.

Using the coefficients of the $C_{M_\theta}(\xi)$ expression in the polynomials for δ_θ and K_θ, the displacement and reduced frequency curves can be determined. Figure 3-29 summarizes the results

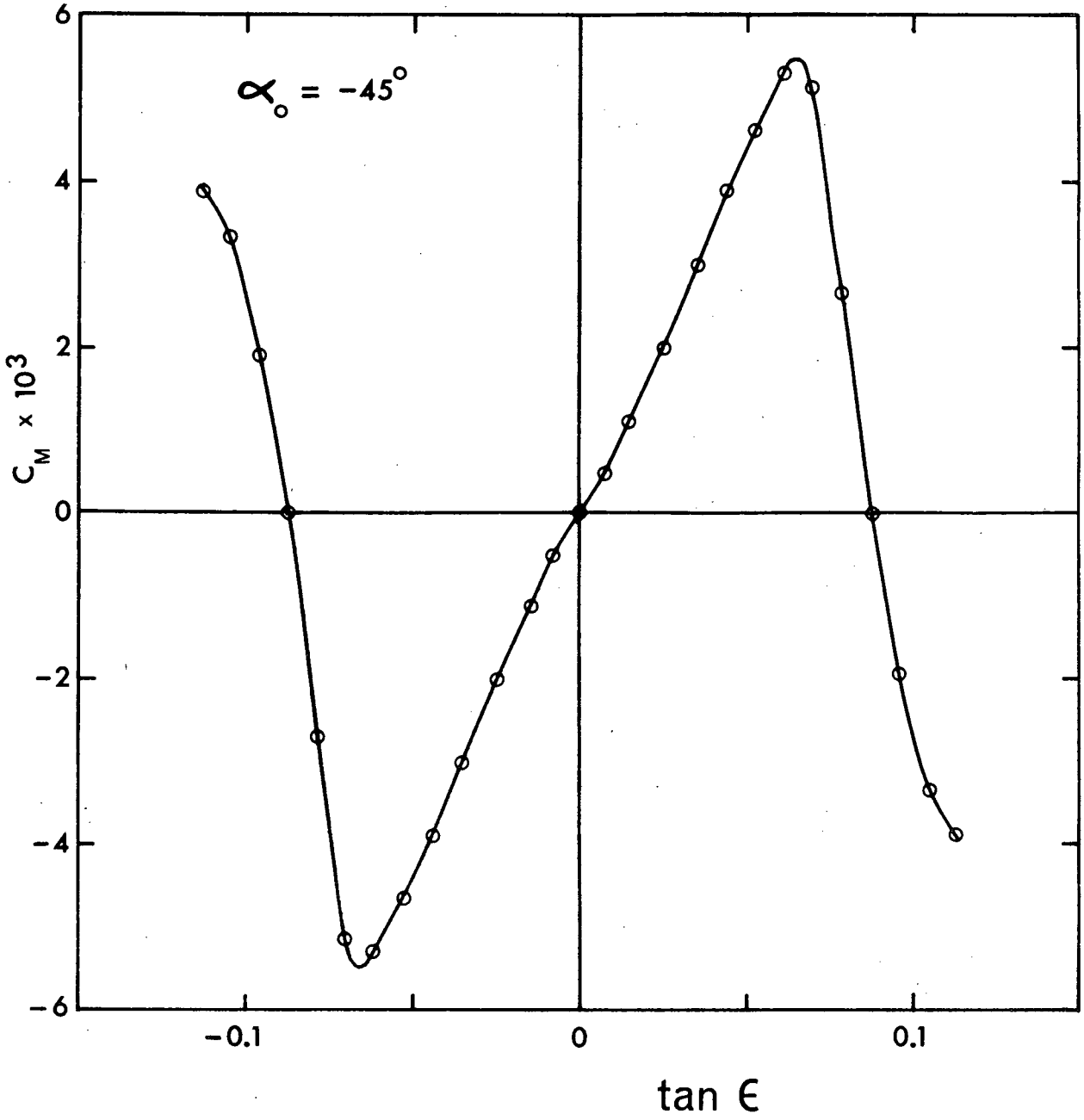

Figure 3-26 Moment coefficient distribution for stationary model at $\alpha_o = 45°$

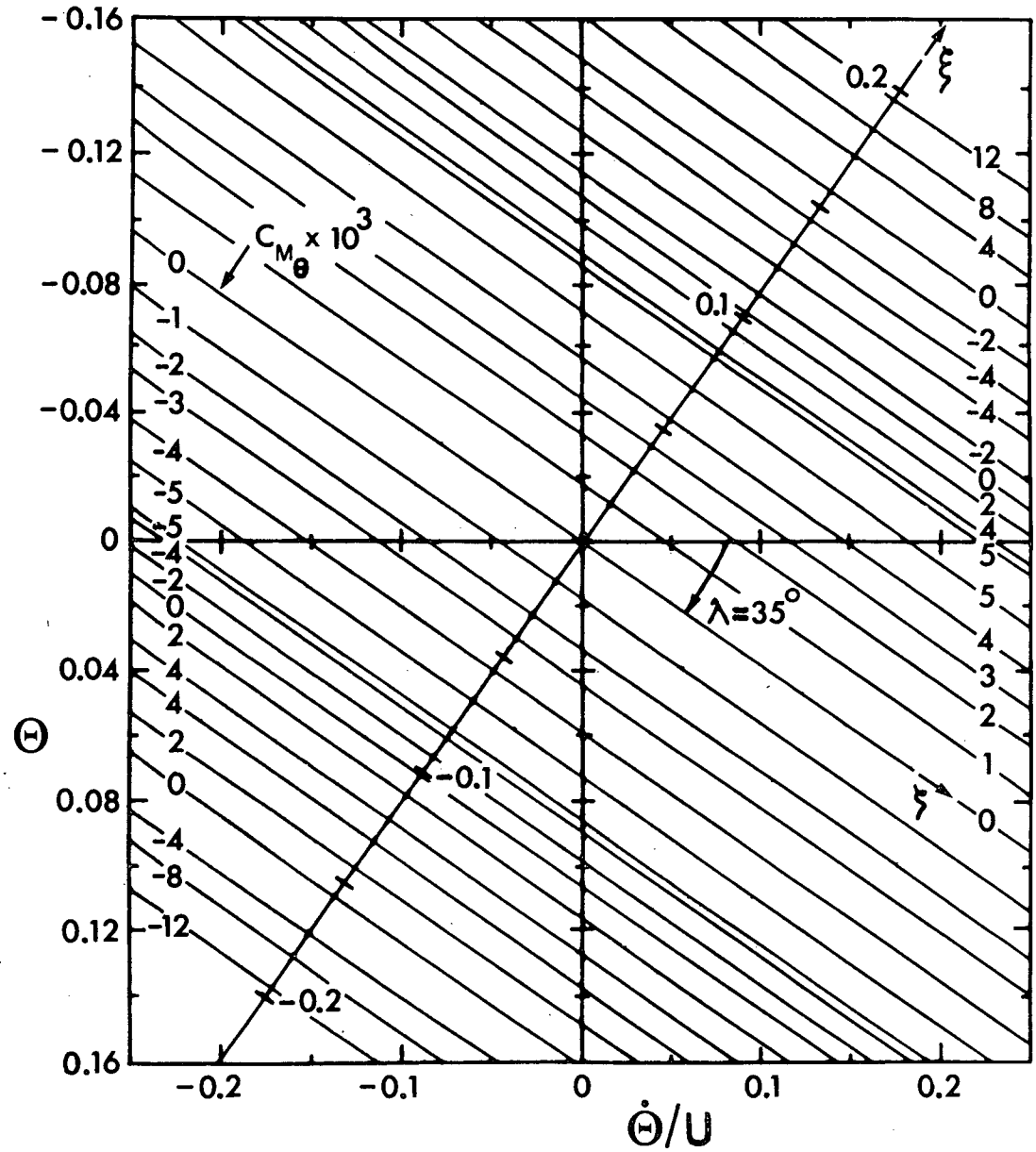

Figure 3-27 Contour plot of torsional moment coefficient as a function of Θ and $\dot{\Theta}$ for $\alpha_o = 45°$

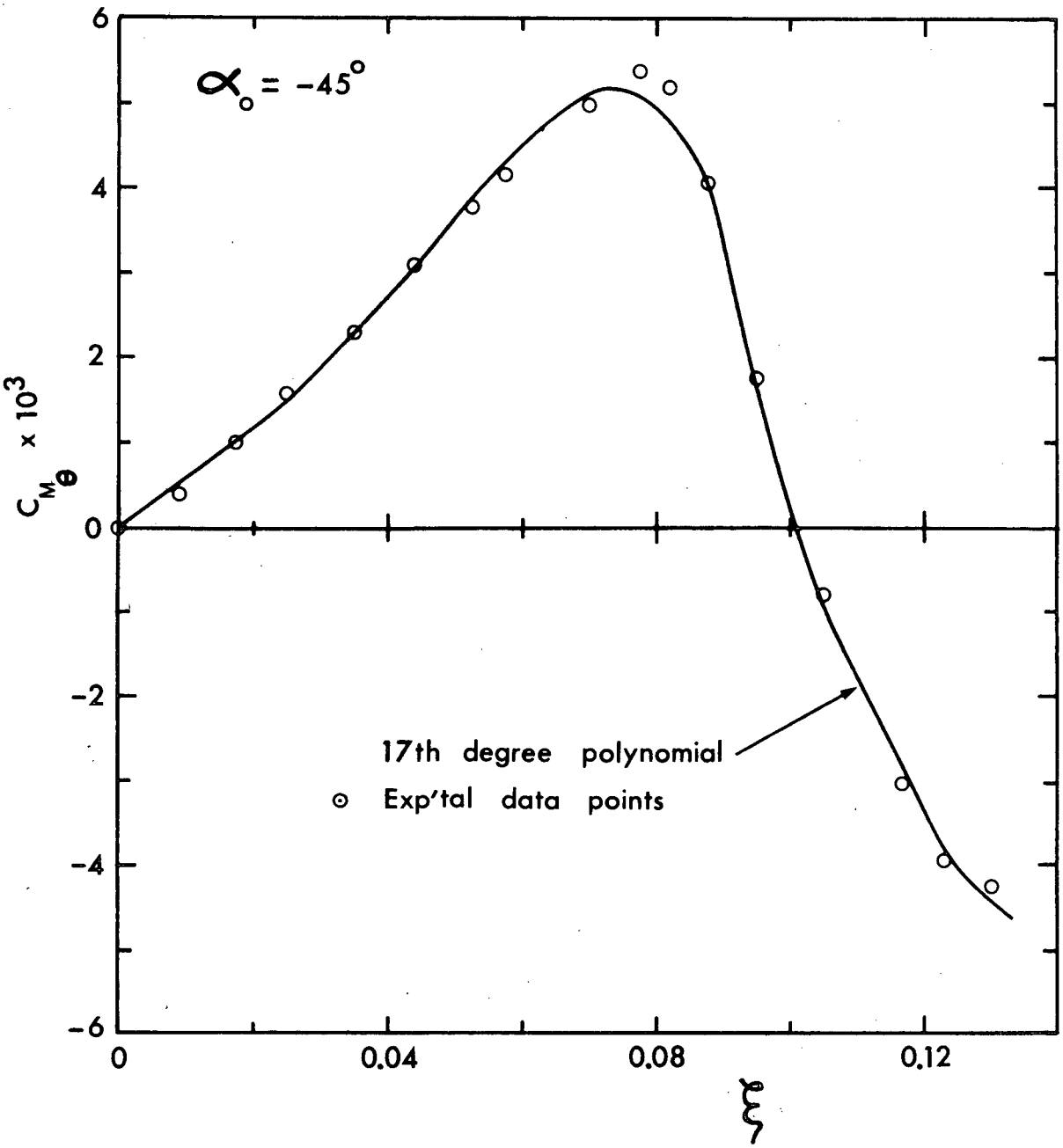

Figure 3-28 Polynomial curve fit of torsional moment coefficient data for angle model at $\alpha_o = -45°$

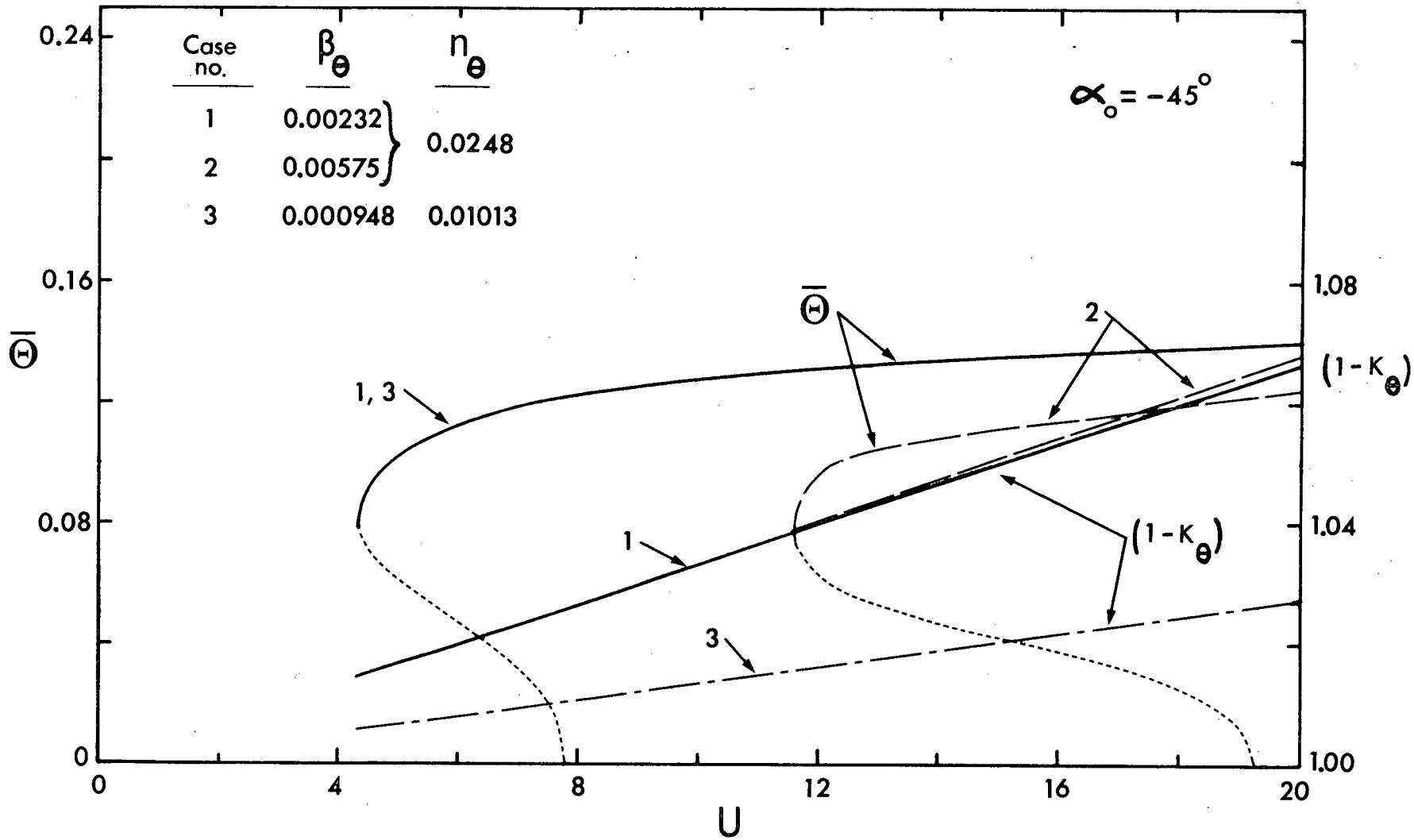

Figure 3-29 Variation of galloping amplitude and reduced frequency with wind velocity for angle section at $\alpha_o = -45°$ as predicted by the quasi-steady theory

for the 3 in. angle model at $\alpha_o = -45°$ with typical values of the system parameters. The plots indicate that the angle section at this orientation is a soft oscillator with a frequency of oscillation slightly higher than the natural frequency. For case 1, the galloping theory predicts a starting velocity $U_o/s = 7.76$ with an amplitude-velocity curve as shown. Similar calculation for the 1 in. angle model at $\alpha_o = -45°$ gives an initial velocity $U_o/s = 590$. The results indicate that galloping will occur only at very high wind speeds or for systems of very low damping, which are outside the range of practical interest.

From Figure 3-29, further information concerning the nature of the galloping instability in torsion can be obtained. The galloping motion shifts to higher velocities with increased damping or reduced inertia parameter. Likewise, the reduced frequency parameter $(1-K_\theta)$ increases with wind velocity and is directly proportional to the inertia parameter n_θ as indicated by the expression for K_θ. However, as suggested by the curves or by direct examination of the equation for δ_θ, the torsional galloping system does not collapse to a reduced or universal form as in the plunging case.

3.6 Concluding Remarks

Based on the experimental and theoretical results the following general remarks can be made concerning the nature of the aeroelastic instability of angle sections with plunging and/or torsional degree(s) of freedom:

(i) Angle sections are susceptible to vortex induced and galloping types of aeroelastic instabilities. The combined plunging and torsional motion indicates the

existence of two distinct centres of rotation, thus substantiating the virtual hinge concept. During lateral resonance and galloping, the coupled motion is predominantly plunging. On the other hand, when distinct torsional resonance occurs, the vibration is principally about a hinge point near the elastic axis. Therefore, the oscillations may be categorized by the type of instability and predominant mode of vibration. Furthermore, the frequency of the coupled motion is essentially the natural frequencies of the individual modes.

In general, the plunging-torsional amplitude results are comparable with the single degree of freedom measurements. Therefore, with consideration of the virtual hinge concept, the investigation of the aeroelastic vibration of angle members can be approximated by studying the individual degrees of freedom. This provides important information about the dynamics and aerodynamics of the structural section. Nevertheless, when plunging galloping precedes the range of torsional resonance, the resulting angular displacement and associated modulation will be substantially reduced.

(ii) In plunging degree of freedom, angle sections are susceptible to both vortex resonance and galloping. There exist ranges of angle of attack of pure vortex resonance or combined vortex and galloping excitations.

Experimental measurements at various orientations confirmed the presence of the galloping instability

as predicted by the quasi-steady theory, thus substantiating the applicability of the analysis. The theory indicates two large regions of galloping instability with two smaller areas in between. Exhibiting either a soft or hard oscillator characteristic, the angle section experiences an increase in galloping amplitude with wind velocity, and undergoes a discontinuous jump at several orientations. The time for amplitude build up reduces with increased wind speed, thus increasing the severity of the galloping instability. Nevertheless, a higher damping or reduced mass parameter shifts the amplitude and build-up time curves toward higher wind velocity, thus delaying the onset of galloping. Collapsing of the experimental results to a single curve in the reduced variable plane confirms the concept of a universal plot as predicted by the quasi-steady theory.

Angle sections experience vortex excitation at all orientations but the severity of the resonance depends on the damping level, mass parameter and unsteady lift coefficient. The stability diagram shows reduction in resonant velocity range and peak displacement with increased damping or decreased mass parameter.

(iii) In torsional degree of freedom, the vortex induced resonance may be severe even at moderate damping levels. However, the section appears to be free from galloping type of aeroelastic instability. This is substantiated by the quasi-steady analysis which predicts that galloping will occur only at relatively high wind velocities

or for systems with very low damping. Furthermore, the galloping theory suggests a variation in the frequency of the torsional oscillation which is in contrast to the plunging case. Although, it is not possible to verify the applicability of the torsional theory, since no galloping was observed experimentally, the quasi-steady approach appears promising based on its success with the plunging analysis.

The vortex excited oscillations, in general, exhibit large random amplitude modulation over the complete range of wind velocity conducive to resonant vibration. Only at certain wind speeds above and below U_{res} does the modulation attain definite frequencies. The maximum as well as the mean amplitudes should be recorded since the peak values, which may be many times greater than the average, may ultimately cause the failure of the structural members. Therefore, the violent, vortex resonance type of instability is, relatively, of more importance than galloping.

(iv) The plunging resonance exhibits the familiar vortex capture phenomenon where the shedding frequency is controlled by the cylinder motion over a finite wind speed range. On the other hand, the torsional vibration shows a vortex control phenomenon where the vortex shedding governs the frequency of oscillation. This extends over a large velocity range following the Strouhal distribution obtained from the stationary model tests. However, at wind speeds far above the resonant value, the cylin-

der frequency is a function of model amplitude. It appears that the vortex shedding initiates the oscillations but loses control as the model amplitude builds up with a resulting drop in oscillation frequency to the natural torsional value. Nevertheless, the displacement eventually diminishes and the cylinder frequency returns to the Strouhal value.

During plunging or torsional motion, the distribution of the phase lag between the displacement and forcing function varies, approximately, from 0°-180° over the region of vortex resonance.

(v) Compared to the stationary and torsional results, the fluctuating pressures on the plunging model are substantially larger in magnitude with less amplitude modulation, and reduced phase variation between neighbouring midspan taps. Consequently the unsteady lift, drag and pitching coefficient increase during plunging resonance. Larger pitching moment about the elastic axis explains the greater torsional resonance observed with the transfer of axis from the centre of gravity to the shear center. Similar to the stationary model results, the local phase difference around the model contour during the dynamic conditions has comparatively little effect (< 10%) on the sectional, unsteady aerodynamic coefficient.

(vi) The wake survey results show similar trend with downstream coordinate for both the stationary and vortex excited models. During resonance in either degree of

freedom, the vortex velocity and longitudinal spacing remain essentially unaltered, however, the wake width experiences substantial increase with plunging motion. Nevertheless, if the lateral spacing is based on the effective blockage ($2\bar{y}$ + h), the resulting nondimensionalized parameter is almost identical to the stationary or torsional model value. It appears that the torsional resonant motion has virtually no effect on the vortex shedding or wake characteristics.

(vii) From the dynamic investigations, it is shown that angle section beams in open engineering structures may exhibit oscillations of a vortex resonance or galloping nature. Therefore, to prevent vibration and possible occurrence of structural failure of the individual members, the design should involve sufficient damping or high natural frequency. This is in agreement with the prediction from the stationary model study.

4. RECOMMENDATIONS FOR FUTURE WORK

Possible theoretical and experimental extensions to the present work may be summarized as follows:

(i) Analysis of the coupled system during galloping using, probably, the method of Variation of Parameters is certainly desirable. The expressions for the aerodynamic force and moment required in the analysis will be, in general, quite complex even with the quasi-steady approach.

(ii) Experimental measurements of torsional galloping to confirm the applicability of the quasi-steady analysis would be a valuable study. This may be carried out using an angle section or some simpler model such as a rectangular cylinder. For such a study accurate pitching moment data is required.

(iii) Determination of spanwise variations of the steady and unsteady aerodynamics along normal and yawed angle sections would be useful. This is important in evaluating the overall three-dimensional nature of the excitation.

(iv) A flow visualization study should prove useful in understanding the character of the flow, such as separation, reattachment, wake geometry, etc.

(v) In general, information concerning wind tunnel wall

interference effects on the steady and unsteady aerodynamic characteristics and wake geometry for bluff bodies is lacking. Therefore, a systematic study during static and dynamic conditions of the model would be of value.

(vi) Since angle sections, when used in open engineering structures, are exposed to atmospheric turbulence, it is of paramount importance to determine its effect on the aeroelastic vibrations. The investigation may be conducted in the wind tunnel under controlled turbulence to obtain an understanding of the phenomenon, but should be supplemented with field tests over terrain exposed to typical turbulent winds.

(vii) Experimental measurements of the steady and unsteady aerodynamic characteristics on angle sections of unequal legs or other structural members under static conditions would be a natural extension of this work. Theoretical predictions of the section dynamics could be ratified by aeroelastic tests.

BIBLIOGRAPHY

1. Kosko, E., "The Frequency Spectrum of a Structural Member in Coupled Flexural-Torsional Vibration," J. Sound and Vibration, Vol.7, No.2, 1968, pp.143-155.

2. Wardlaw, R.L., "Aerodynamically Excited Vibrations of a 3-inch x 3-inch Aluminum Angle in Steady Flow," National Research Council of Canada, Aeronautical Report No. LR-482, June 1967.

3. Wardlaw, R.L. and Davenport, A.G., "Some Experiments on the Fluctuating Forces on Flat Plates in Turbulent Flow," National Research Council of Canada, Aeronautical Report LR-416, December 1964.

4. Strouhal, V., "Über eine besondere Art der Tonerregung," Wied. Ann. Physik u. Chem., Neue Folge, Vol.V, 1878, pp.216-251.

5. Bénard, H. "Hydrodynamique Expérimentale-Formation de centres de giration à l'arriere d'un obstacte en mouvement," Comptes Rendus (Académie des Sciences), Vol.147, 1908, pp.839-842; "Hydrodynamique Expérimentale-Sur les lois de la fréquence des tourbillons atternés détaches derrière un obstacle," Comptes Rendus, Vol.182, 1926, pp.1375-1377; "Hydrodynamique Expérimentale-Sur l'inexatitude, pour les liquides reels, des lois théoriques de Kármán relatives à la stabilité des tourbillons alternés," Comptes Rendus, Vol.182, 1926, pp.1523-1525.

6. Kármán, Th. Von and Rubach, H., "Über den Mechanismus des Flüssigkeitsund Luftwiderstandes," Physik. Z., Vol.13, 1912, pp.49-59; Kármán, Th. Von, "Über den Mechanismus des Widerstands, den ein bewegter Körper in einer Flüssigkeiterfahrt," Göttinger Nachrichten, Math. Physik. Kl., 1911, pp.509-519; and, 1912, pp.547-556.

7. Heisenberg, Von W., "Die Absoluten Dimensionen der Kármánschen Wirbelbewegung," Physik. Z., Vol.23, 1922, pp.363-366.

8. Marris, A.W., "A Review of Vortex Streets, Periodic Wakes, and Induced Vibration Phenomena," J. Basic Engng., ASME, Vol.86, 1964, pp.185-196.

9. Den Hartog, J.P., "Transmission Line Vibration Due to Sleet," Trans. AIEE, Vol.51, No.4, 1932, pp.1074-1086; Mechanical Vibrations, McGraw-Hill, New York, 4th ed., 1956.

10. Strutt, J.W. (Lord Rayleigh), "On Maintained Vibrations," Phil. Mag., Vol.15, Series 5, 1883, pp.229-235; Theory of Sound, 2nd ed., Vol.1, Dover, New York, 1945.

11. van der Pol, B., "The Nonlinear Theory of Electric Oscillations," Proc. Inst. Radio Engineers, Vol.22, No.9, 1934, pp.1051-1086.

12. Le Corbeiller, Ph., "The Non-linear Theory of the Maintenance of Oscillations," J. Inst. Electrical Engineers, Vol.79, 1936, pp.361-378.

13. Minorsky, N., Introduction to Non-Linear Mechanics, Edwards Brothers Inc., Ann Arbor, Michigan, 1947.

14. Sisto, F. "Stall-Flutter in Cascades," J. Aeronautical Sciences, Vol.20, No.9, 1953, pp.598-604.

15. Scruton, C. "On the Wind-Excited Oscillations of Stacks, Towers, and Masts," Proc. First Int. Conf. On Wind Effects on Bldgs. and Structures, NPL, Teddington, Vol.II, 1965, pp.797-832.

16. Parkinson, G.V. and Brooks, N.P.H., "On the Aeroelastic Instability of Bluff Cylinders," Trans. ASME, J. Appl. Mech., Vol.83, June 1961, pp.252-258.

17. Parkinson, G.V. and Smith J.D., "The Square Prism as an Aeroelastic Non-Linear Oscillator," Quart. J. Mech. and Appl. Math., Vol.17, Part 2, May 1964, pp.225-239.

18. Parkinson, G.V. and Santosham, T.V., "Cylinders of Rectangular Section as Aeroelastic Nonlinear Oscillators," ASME Vib. Conf., Paper No.67-VIBR-50, March 1967.

19. Ii, J.M., "A Theoretical Approach to a Study of Stall-Flutter Problems," Cornell Univ., Grad. School of Aeronautical Engineering, Report AFOSR 899, Ithaca, New York, June 1961.

20. Dicker, D., "Aerodynamic Stability of H Sections," J. Engng. Mech. Proc. ASCE, April 1966.

21. Novak, M., "Aeroelastic Galloping of Rigid and Elastic Bodies," Univ. of Western Ontario, London, Canada, BLWT-3-68, March 1968.

22. Scruton, C. "The Use of Wind Tunnels in Industrial Aerodynamic Research," NPL, Aerodynamics Division, Report No.411, September 1960.

23. Richardson, A.S., Martucelli, J.R. and Prise, W.S., "Research Study on Galloping of Electric Power Transmission Lines," Proc. First Int. Conf. on Wind Effects on Bldgs. and Structures, NPL, Teddington, Vol.II, 1965, pp.612-686.

24. Cheers, F., "A Note on Galloping Conductors," National Research Council of Canada, Report No.MT-14, June 1950.

25. Dryden, H.L. and Hill, G.C., "Wind Pressures on a Model of the Empire State Building," J. Res. Natn. Std., Vol.10, Report No.545, pp.493-523.

26. Davenport, A.G., "The Treatment of Wind Loading on Tall Buildings," Proc. Symp. on Tall Bldgs., Southampton, April 1966.

27. Parkinson, G.V. "Aspects of the Aeroelastic Behaviour of Bluff Cylinders," Trans. EIC, Vol.6, No.B-1, November 1963.

28. Dale, J., Henzel, H. and McCandless, J., "Dynamic Characteristics of Underwater Cables Flow Induced Transverse Vibrations," U.S. Naval Air Development Center, Johnsville, Pennsylvania, Report No.NADC-AE-6620, September 1966.

29. Farquharson, F.B., Smith, F.C. and Vincent, G.S., "Aerodynamic Stability of Suspension Bridges," Univ. of Washington Expt. Sta., Seattle, Bul. No.116, Parts I-V, 1950-1954.

30. Kelley, E.F., "Aerodynamic Stability of Suspension Bridges," Trans. ASCE, Vol.120, 1955, pp.753-759.

31. McGregor, D.M., "An Experimental Investigation of the Oscillating Pressures on a Circular Cylinder in a Fluid Stream," Univ. of Toronto, Inst. of Aerophysics, Tech. Note 14, June 1957.

32. Gerrard, J.H., "An Experimental Investigation of the Oscillating Pressures on a Circular Cylinder Shedding Turbulent Vortices," J. Fluid Mech., Vol.11, 1961, pp.244-256.

33. Ferguson, N., "The Measurement of Wake and Surface Effects in the Subcritical Flow Past a Circular Cylinder at Rest and in Vortex Excited Oscillations," Univ. of British Columbia, M.A.Sc. Thesis, September 1965.

34. Modi, V.J. and Heine, W., "On the Pressure Fluctuations and Wake Geometry Associated with Several Bluff Bodies," JSME Proc. 15th Japan Nat. Cong. Appl. Mech., 1965, pp.7-18.

35. Wiland, E., "Unsteady Aerodynamics of Stationary Elliptic Cylinders in Subcritical Flow," Univ. of British Columbia, M.A.Sc. Thesis, April 1968.

36. Grove, A.S., Shair, F.H., Petersen, E.E. and Acrivos, A., "An Experimental Investigation of the Steady Separated Flow Past a Circular Cylinder," J. Fluid Mech., Vol.19, Part 1, 1963, pp.60-80.

37. Bishop, R.E.D. and Hassan, A.Y., "The Lift and Drag Forces on a Circular Cylinder in a Flowing Fluid," Proc. Roy. Soc. of London, Series A, Vol.277, 1964, pp.32-50.

38. Humphreys, J.S., "On a Circular Cylinder in a Steady Wind at Transition Reynolds Numbers," J. Fluid Mech., Vol.9, 1960, pp.603-612.

39. Fung, Y.C., "Fluctuating Lift and Drag Acting on a Cylinder in a Flow at Supercritical Reynolds Numbers," J. Aerospace Sciences, Vol.27, No.11, November 1960, pp.801-814.

40. Vickery, B.J., "Fluctuating Lift and Drag on a Long Cylinder of Square Cross-Section in a Smooth and in a Turbulent Stream," NPL, Aerodynamics Div., Report No.1146, April 1965.

41. Bishop, R.E.D. and Hassan, A.Y., "The Lift and Drag Forces on a Circular Cylinder Oscillating in a Flowing Fluid," Proc. Roy. Soc. of London, Series A, Vol.277, 1964, pp.51-75.

42. Ferguson, N. and Parkinson, G.V., "Surface and Wake Flow Phenomena of the Vortex-Excited Oscillation of a Circular Cylinder," ASME Vib. Conf., Paper No.67-VIBR-31, March 1967.

43. Molyneux, W.G., "Measurement of the Aerodynamic Forces on Oscillating Airfoils," AGARD, Report No.35, 1956.

44. Gerrard, J.H., "The Three-Dimensional Structure of the Wake of a Circular Cylinder, J. Fluid Mech., Vol.25, Part 1, pp.143-164.

45. Toebes, G.H., "Fluidelastic Features of Flow Around Cylinders," Int. Research Seminar: Wind Effects on Bldgs. and Structures, NRC, Ottawa, September 1967.

46. Prendergast, V., "Measurement of Two-Point Correlations of the Surface Pressure on a Circular Cylinder," Univ. of Toronto, Inst. of Aerophysics, Tech. Note 23, 1958.

47. Feng, C.C., "The Measurement of Vortex Induced Effects in Flow Past Stationary and Oscillating Circular and D-Section Cylinders," Univ. of British Columbia, M.A.Sc. Thesis, October 1968.

48. Brooks, P.N.H., "Experimental Investigation of the Aeroelastic Instability of Bluff Two-Dimensional Cylinders," Univ. of British Columbia, M.A.Sc. Thesis, July 1960.

49. Smith, J.D., "An Experimental Study of the Aeroelastic Instability of Rectangular Cylinders," Univ. of British Columbia, M.A.Sc. Thesis, August 1962.

50. Santosham, T.V., "Force Measurements on Bluff Cylinders and Aeroelastic Galloping of a Rectangular Cylinder," Univ. of British Columbia, M.A.Sc. Thesis, February 1966.

51. Chuan, R.L., "Study of Vortex Shedding as Related to Self-excited Torsional Oscillations of an Airfoil," NACA, Tech. Note 2429, September 1951.

52. Otsuki, Y., "Tall Buildings and Aeroelastic Problems," Conf. Earthquake and Wind Effects, 1967.

53. Toebes, G.H. and Eagleson, P.S., "Hydroelastic Vibrations of Flat Plates Related to Trailing Edge Geometry," J. Basic Engng., ASME. Vol.83, Series D, No.4, December 1961, pp. 671-678.

54. Eagleson, P.S., Noutsopoulos, G.K. and Daily, J.W., "The Nature of Self-Excitation in the Flow-Induced Vibration of Flat Plates," J. Basic Engng., ASME, Series D, No.4, November 1963.

55. Thornton, C.P., "Wind Tunnel Tests of the Aerodynamically Induced Vibrations of Some Simple Structural Members," National Research Council of Canada, Mech, Engng. Report MA-245, 1962; also Movie Film, "Aeroelastic Instability of Aluminum Angle Section," National Research Council of Canada, Aeronautical Establishment.

56. Parkinson, G.V., "Aeroelastic Galloping in One Degree of Freedom," Proc. First Int. Conf. on Wind Effects on Bldgs. and Structures, NPL, Teddington, Vol.II, 1965, pp.581-609.

57. Parkinson, G.V. and Modi, V.J., "Recent Research on Wind Effects on Bluff Two-Dimensional Bodies," Int. Research Seminar: Wind Effects on Bldgs. and Structures, NRC, Ottawa, September 1967.

58. Whitbread, R.E., "Model Simulation of Wind Effects on Structures," Pro. First Int. Conf. on Wind Effects on Bldgs. and Structures, NPL, Teddington, Vol.I, 1965, pp.283-306.

59. Soroka, W.W., "Note on the Relation between Viscous and Structural Damping Coefficients," J. Aeronautical Sciences, Vol.16, 1949, pp.409-410.

60. Kimball, A.L. and Lovell, D.E., "Internal Friction in Solids," Physics Review, Vol.30, Series 2, December 1927, p.948.

61. Iokibe, K. and Sakai, S., "The Effect of Temperature on the Modulus of Rigidity and on the Viscosity of Solid Metals," Phil. Mag., Vol.42, Series 6, 1921, pp.397-418.

62. Ockleston, A.J., "The Damping of the Lateral Vibration of a Mild Steel Bar," Phil. Mag., Vol.26, Series 7, 1938, pp.705-712.

63. Bryer, D.W., Walshe, D.E. and Garner, H.C., "Pressure Probes Selected for Three-Dimensional Flow Measurement," Aeronautical Research Council, R. and M. No.3037, 1958.

64. Hoerner, S.F., Fluid-Dynamic Drag, 1965, Chapter 3, pp.6-18 and Chapter 4, p.6.

65. Roshko, A., "A New Hodograph For Free-Streamline Theory," NACA, Tech. Note 3168, July 1954.

66. Roshko, A. "On the Wake and Drag of Bluff Bodies," J. Aeronautical Sciences, Vol.22, No.2, February 1955, pp.124-133.

67. Fage, A. and Johansen, F.C., "The Structures of Vortex Sheets," Phil. Mag., Series 7, Vol.5, No.28, 1928, pp.317-440.

68. Schaefer, J.W. and Eskinazi, S., "An Analysis of the Vortex Street Generated in a Viscous Fluid," J. Fluid Mech., Vol.6, 1959, pp.241-260.

69. Hooker, S.G., "On the Action of Viscosity in Increasing the Spacing Ratio of a Vortex Street," Proc. Roy. Soc. of London, Series A, Vol.154, 1936, pp.67-89.

70. Fage, A. and Johansen, F.C., "On the Flow of Air Behind an Inclined Flat Plate of Infinite Span," Proc. Roy. Soc. of London, Series A, Vol.116, 1927, pp.170-197.

71. Rosenhead, L. and Schwabe, M., "An Experimental Investigation of the Flow Behind Circular Cylinders in Channels of Different Breadths," Proc. Roy. Soc. of London, Series A, Vol.129, 1930, pp.115-135.

72. "Application of Spring Strips to Instrument Design," NPL, Notes on Appl. Sc., No.15, 4th ed., 1965, pp.2-5.

73. Eastman, F.S., "The Design of Flexure Pivots," J. Aeronautical Sciences, Vol.5, No.11, November 1937, pp.16-21.

74. Haringx, J.A., "The Cross-Spring Pivot as a Constructional Element," Appl. Sci. Res., Vol. A1, 1947-49, pp.313-332.

75. Wittrick, W.H. "The Theory of Symmetrical Crossed Flexure Pivots," Austrailian J. Sci. Res., A, Vol.1, No.2, 1948, pp.121-134.

76. Wittrick, W.H., "The Properties of Crossed Flexure Pivots, and the Influence of the Point at which the Strips Cross," The Aeronautical Quarterly, Vol.II, February 1951, pp.272-292.

77. Young, W.E., "An Investigation of the Cross-Spring Pivot," J. Appl. Mech., Vol.II, June 1944, pp.A113-A120.

78. Garland, C.F., "The Normal Modes of Vibrations of Beams Having Noncollinear Elastic and Mass Axes," J. Appl. Mech., ASME Trans., Vol.62, 1940, pp.A97-A105.

79. Parkinson, G.V., Feng, C.C. and Ferguson, N., "Mechanisms of Vortex-Excited Oscillation of Bluff Cylinders," Symposium on Wind Effects on Bldgs. and Structures, NPL/Roy. Aeronautical Society, London, March 1968.

80. Cunningham, W.J., Introduction to Nonlinear Analysis, McGraw-Hill, New York, 1958.

81. Pankhurst, R.C. and Holder, D.W., Wind Tunnel Technique, Pitman and Sons Limited, London, 1952, Chapter 8.

82. Glauert, M., "The Interference of Wind Channel Walls on the Aerodynamic Characteristics of an Aerofoil," British A.R.C., R. and M. 867, March 1923; and, British A.R.C., R. and M. 889, 1923-24.

83. Fage, A., "On the Two-Dimensional Flow Past a Body of Symmetrical Cross-Section Mounted in a Channel of Finite Breadth," British A.R.C., R. and M. 1223, 1928-29.

84. Durand, W.F., Aerodynamic Theory, Durand Reprinting Committee, California, Vol.III, Div.I, Part 1, Chapter III, "Influence on the Dimensions of the Air Stream," 1943, pp.280-319.

85. Allen, H.J. and Vincenti, W.G., "Wall Interference in a Two-Dimensional-Flow Wind Tunnel, with Consideration of the Effect of Compressibility," NACA 13th Annual Report, No. 782, 1944, pp. 155-184.

86. Lock, M., "The Interference of a Wind Tunnel on a Symmetrical Body," British A.R.C., R. and M. 1275, 1929.

87. Glauert, H., "The Characteristics of a Kármán Vortex Street in a Channel of Finite Breadth," British A.R.C., R. and M. 1151, 1928-29.

88. Maskell, E.C., "Theory of the Blockage Effects on Bluff Bodies and Stalled Wings in a Closed Wind Tunnel," British A.R.C., R. and M. 3400, November 1963.

89. Bearman, P.W., "The Flow Around a Circular Cylinder in the Critical Reynolds Number Régime," NPL, Aerodynamics Div., Report No. 1257, January 1968.

90. Jones, W.P., "Wind Tunnel Interference Effects on the Values of Experimentally Determined Derivative Coefficients for Oscillating Aerofoils," British A.R.C., R. and M. 1912, 1943.

91. Jones, W.P., "Wind Tunnel Interference Effects on Measurements of Aerodynamic Coefficients for Oscillating Aerofoils," British A.R.C., R. and M. 2786, 1958.

92. Acum, W.E.A., "Wall Corrections for Wings Oscillating in Wind Tunnels of Closed Rectangular Section," "Part I-Theory and Tables," British A.R.C., Report No. 19593, October 1957; and, "Part II-Application to a Delta Planform in a 9 x 7 tunnel," British A.R.C., Report No. 19756, January 1958.

93. Runyan, H.L., Woolston, D.S. and Rainey, A.G., "Theoretical and Experimental Investigation of the Effect of Tunnel Walls on the Forces Acting on the Oscillating Airfoil in Two-Dimensional Compressible Flow," NACA, Report No. 1262,1956.

94. Molyneux, W.G., "Wind Tunnel Interference in Dynamic Measurements," R.A.E., Tech. Memo. No. Structures 604, March 1964.

95. Roberts, B.W., "The Nature of the Free-Stream Conditions Approaching an Oscillating Body in a Low Speed Wind Tunnel," The Aeronautical Quarterly, Vol.17, Part 4, November 1966.

96. Ross, D., "Vortex-Shedding Sounds of Propellers," Bolt, Beranek and Newman, Report No.1115, March 1964.

97. Cheng, S., "An Experimental Investigation of the Auto-rotation of a Flat Plate," Univ. of British Columbia, M.A.Sc. Thesis, November 1966.

APPENDIX I

Geometrical Properties of Angle Section Members

The cross-sectional features of the designed models were somewhat 'idealized' since their edges were sharp and the surfaces smooth. This was necessary to facilitate the construction of the thin-walled, hollow models. Nevertheless, commercially available aluminum angle sections have similar geometry and, therefore, are well approximated by the sharp-edged models. On the other hand, structural steel angles do have rounded edges as well as rough surfaces (Figure I-1). Table I-1 compares the geometric features of the various wind tunnel models including the commercially available structural angles tested during the experiment. All models were similar in length extending across the effective height of the wind tunnel. The four angle sections listed at the bottom of the table were not tested experimentally but are included for further comparison of the geometric features of commercially available structural angles and the wind tunnel models.

Survey of the tabulated data indicates that the pressure tap, as well as 1 in. and 3 in. dynamic models compare favourably with the structural aluminum angles of similar size except for the filleted inner corner on the commercial members. However, this difference in inner radius will be of minor aerodynamic importance since the fluid near this area on the section is almost stagnant. Flow visualization using a smoke tunnel substantiated this observation.

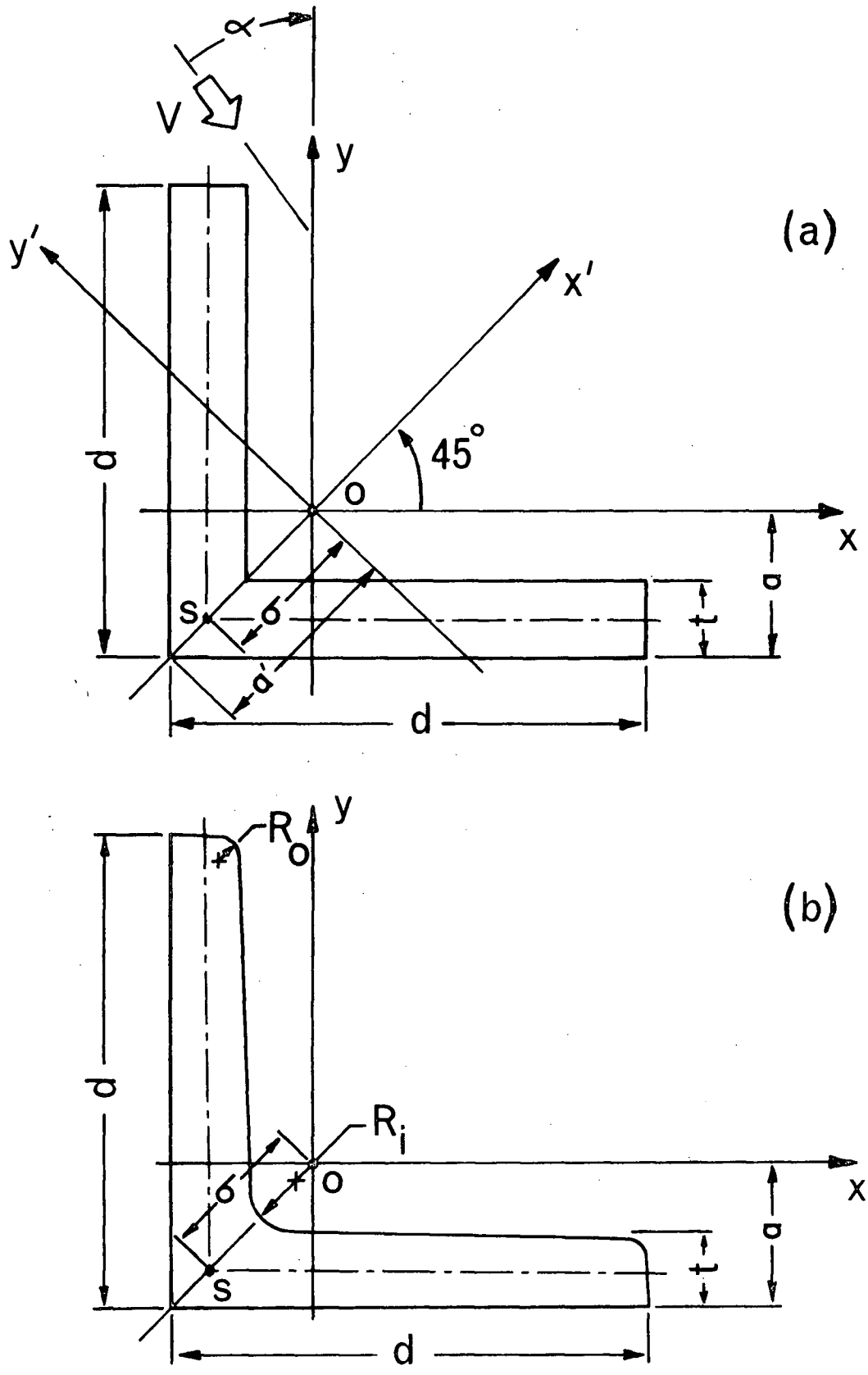

Figure I-1 Cross-sections of angle member (a) 'idealized' angle section (b) typical structural angle

TABLE I-1
Geometric Features of Angle Sections

Model	Nominal dimensions					c.g. a in.	shear centre σ - in.	I_x in.^{4}	system m' lbm/ft	system I lbm-in.^{2}/ft	Material
	d in.	t in.	length in.	R_o in.	R_i in.						
pressure tap	3	1/2	26 3/4	0	0	0.93	0.96	2.3	0.91	8.2	aluminum, acrylic hollow section
large dynamic	3	1/2	26 3/4	0	0	0.92	0.96	2.1	0.71	7.9	acrylic hollow section
small dynamic	1	1/6	26 3/4	0	0	0.31	0.32	0.027	0.70	7.0	aluminum solid section
balance A	3	1/2	27	0	0	0.90	0.93	1.95	2.92	7.2	aluminum solid section
balance B	Identical to model A except for 1/4 in. thick end plates										
balance C	3	1/2	27	1/8	5/16	0.93	0.98	2.2	9.4	24.0	structural steel angle
balance D	3	1/4	27	1/16	5/16	0.84	1.03	1.2	4.9	13.4	structural steel angle
balance E	3	1/4	27	1/64	7/32	0.84	1.01	1.2	1.71	4.5	structural aluminum angle
balance F	2	1/3	27	0	0	0.62	0.64	0.44	1.42	1.6	aluminum solid section
-	3	1/2	-	1/64	1/4	0.93	0.96	2.2	3.30	8.3	structural aluminum
-	1	3/16	-	1/16	3/16	0.31	0.32	0.030	1.16	0.32	structural steel angle
-	1	1/8	-	1/16	3/16	0.30	0.33	0.022	0.80	0.24	structural steel angle
-	1	3/16	-	1/64	5/32	0.31	0.32	0.030	0.41	0.11	structural aluminum angle

APPENDIX II

Wind Tunnel Wall Corrections

There is a considerable body of information[81-87 et al] on wind tunnel interference for stationary streamlined models in steady flow. In general, the theoretical and semi-empirical investigations express the wall effects as a series in ascending powers of the model to tunnel characteristic dimension ratio with the analysis confined to the first or second order terms. These corrections have been found satisfactory in most situations and can be applied with some measure of confidence.

For stationary bluff cylinders, there is some experimental information on wall confinement but the theoretical analysis is relatively less complete. Pankhurst and Holder,[81] and Durand[84] provide techniques for extrapolating streamline body analysis to bluff circular cylinders but their applicability is rather limited. More appropriate, under this condition of completely separated flow, is the simplified expression quoted by Whitbread[58] which is a particular case of a general analysis by Maskell.[88] Using Maskell's mathematical model, Vickery[40] obtained blockage corrections to Strouhal number and fluctuating lift force and applied it to the flow around a square cylinder. For a circular cylinder near the critical Reynolds number, where the drag coefficient drops to approximately 0.2 thus making the solid blockage as important as wake blockage, Bearman[89] has suggested the application of the method of Allen and Vincenti[85] developed for low drag, streamlined airfoils. Glauert[87] and Fage[83] have considered, theoretically, the two-dimensional flow around cylinders in

channels of finite breadth. The experimental measurements by Rosenhead and Schwabe,[71] and Fage and Johansen[70] provide useful information concerning the influence of wall confinement on flow characteristics. Test results on stationary angle models taken during the course of this research programme, gave some information on wall interference with regards to the departmental wind tunnel system.

The analysis of wall interference on oscillating models is considerably more complex, and to date, effective methods for predicting the corrections have not been completely evolved. Nevertheless, for oscillating airfoils in wind tunnels, there are various theoretical and experimental approaches reported[90-93] et al. Molyneux[94] has presented a good review of this literature. On the other hand, for oscillating bluff bodies, information on wall confinement is almost completely lacking.

As indicated by Pankhurst and Holder,[81] the interference from wind tunnel walls during steady flow condition may be divided into:

(i) solid blockage;

(ii) wake blockage;

(iii) lift or circulation effect;

(iv) boundary layer interference; and

(v) streamwise static pressure gradient influence.

For an object symmetrically placed in the flow field, (iii) does not exist. For the wind tunnel at the University of British Columbia, the wall boundary layer thickness in the test section is relatively small partly due to the filleted corners which compensate for boundary layer growth. Furthermore, the pressure

integrated and balance measured aerodynamic coefficients (Figure 2-13) showed good correlation. Therefore, (iv) appears to be negligible. Similarly, for the tunnel (v) was found to be of minor significance (less than 1%). Therefore, solid and wake blockages represent the major interferences on model aerodynamic characteristics. Available corrections appropriate for the stationary angle section measurements are summarized in the following pages.

(1) Mean Free Stream Velocity

According to Pankhurst and Holder,[81] the wind speed correction is a sum of the solid and wake blockages given by

$$\frac{V_F}{V} = (1 + \sigma) \qquad (1)$$

where V_F = free stream or corrected velocity;

V = measured approaching velocity value;

$\sigma = \sigma_s + \sigma_w$, correction factor depending on model and tunnel geometry.

Another estimate of the velocity correction can be obtained from Maskell's simplified relation (equation (2)). Illustrated in Figure II-1, is a comparison between the percentage velocity corrections given by the above two methods when applied to the 3x3 in. angle models. The discrepancy between the two corrections can be explained by the fact that the former is more applicable to streamlined bodies while the latter is for separated flow condition. The velocity correction of Allen and Vincenti as stated by Bearman is identical to that of Pankhurst and Holder.

(2) Fluctuating Free Stream Conditions

Roberts[95] investigated the flow conditions ahead of an

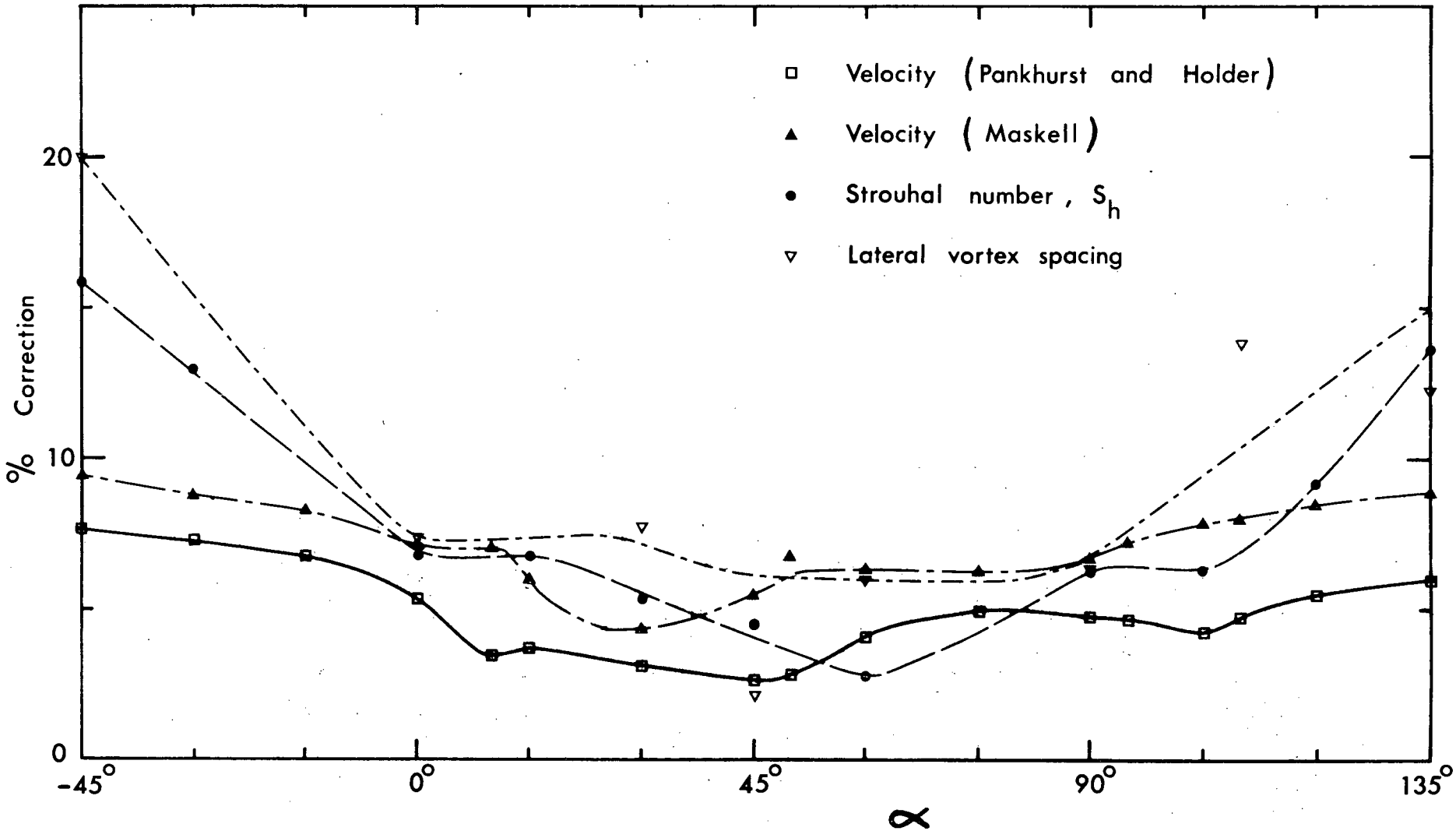

Figure II-1 Percentage correction applicable to 3 in. angle section tested in departmental wind tunnel

oscillating model by using the unsteady form of the Bernoulli's equation. Two-dimensional circular cylinders oscillating harmonically in the streamwise direction showed the upstream flow variables to be functions of the frequency and amplitude of the motion. For amplitudes of one diameter, the velocity and static pressure variations were as large as 20 and 40 percent, respectively. Thus, one would expect the time-dependent phenomenon to be significant where large amplitude, low frequency, model oscillations exist.

(3) Effective Angle of Attack

For thin airfoil sections, both Durand, as well as Allen and Vincenti provide expressions for wall interference corrections to the angle of attack by considering an equivalent induced velocity field of a system of images on the base profile. However, for a bluff section no appropriate analysis is apparently available.

(4) Mean Static Pressure and Resultant Steady Forces

Using the free streamline model, Maskell[88] has shown that the steady static pressure and drag on bluff structures can be corrected as follows:

$$\frac{1 - C_{p_F}}{1 - C_p} = \frac{C_{D_F}}{C_D} = \frac{1}{1 - \frac{C_D}{C_{p_{b_F}}} \frac{S}{C}} \qquad (2)$$

where C_{p_F}, C_{D_F} = free stream or corrected static pressure and drag coefficients, respectively;

C_p, C_D = measured static pressure and drag coefficients;

$C_{p_{b_F}}$ = free stream base pressure coefficient, $-(k^2-1)$;

S = model area on which C_D is based;

C = tunnel test section area.

This is identical to the blockage corrections given by Vickery.[40] The expression is also applicable to the correction of other force and moment coefficients.

Glauert[87] derived an expression for the drag coefficient for a body forming a wake of alternate vortices in a channel of finite width. The analysis, based on Lock's image method and Kármán's vortex street theory, was developed for a plate normal to the flow but, as stated by Durand, is applicable for other bodies of abrupt or sharp-edged form. The theoretical expression for the drag coefficient in confined flow is given by the equation

$$C_D = \left(5.656 - 2.24\frac{u}{V}\right)\frac{ub}{Ve} + 24\left(\frac{ub}{Ve}\right)^2\frac{e}{H} \qquad (3)$$

where $u = W - V_v$

W = surrounding fluid velocity on which the vortex system is superimposed (equation (15));

V_v = vortex streamwise velocity;

b = measured lateral vortex row spacing.

This expression is similar to that given by Kármán for the case of a plane unlimited flow,

$$C_{D_F} = \left(5.656 - 2.24\frac{u_F}{V_F}\right)\frac{u_F b_F}{V_F e} \qquad (4)$$

where

$$u_F = \frac{\Gamma}{2a_F}\tanh\frac{\pi b_F}{a_F}$$

and a_F = longitudinal spacing between consecutive vortices of strength Γ .

However, to use the expression for C_D it is necessary to know, à priori, the values of u/V and b/e for the body in a constrained flow. Glauert gave an approximate theoretical solution to this problem by considering the rate of vorticity generated by the body and the amount of vorticity passing downstream in the form of discrete vortices. This study provided an expression for the drag coefficient in constrained flow as

$$C_D = C_{D_F} + \left\{ 32 - 3.16 \frac{u_F}{V_F} \frac{1-4u_F/V_F}{1-2u_F/V_F} \right\} \left(\frac{u_F b_F}{V_F e} \right)^2 \frac{e}{H} \qquad (5)$$

where u_F/V_F and b_F/e correspond to the unlimited flow. In practice, the second term in the parenthesis is generally negligible and, therefore, the drag expression reduces to

$$C_D = C_{D_F} + 32 \left(\frac{u_F b_F}{V_F e} \right)^2 \frac{e}{H} \qquad (6)$$

However, the theory is still incomplete, since it does not predict u_F/V_F and b_F/e. An analysis by Heisenberg,[7] to complete the theory for a flat plate, gave the values

$$\frac{u_F}{V_F} = 0.2295 \quad \text{and} \quad \frac{u_F b_F}{V_F e} = 0.3535 \qquad (7)$$

If Heisenberg's results are adopted, drag correction for a flat plate normal to the flow becomes

$$\frac{C_{D_F}}{C_D} = 1 - \frac{4}{C_D}\frac{e}{H} \tag{8}$$

which can be referred to as Glauert-Heisenberg's formula. Its predictions are in agreement with experimental results given by Fage and Johansen.[70] It should be noted that this expression is of the same form as Maskell's simplified equation (2) except that $-C_D/C_{p_{b_F}}$ is replaced by $4/C_D$.

Applicability of Glauert's simplified equation (6) for C_D to the measurements on the angle section can be shown by the following example. For the 1 in. angle model mounted at $\alpha = -45°$, and considering the approximate experimental values of $(u/V)_\infty = 0.201$ and $(b/e)_\infty = 1.77$, the drag expression becomes

$$\frac{C_{D_F}}{C_D} = 1 - \frac{4.05}{C_D}\frac{e}{H} \tag{9}$$

which compares well with equation (8) for the flat plate.

Bearman, as well as Pankhurst and Holder suggested that their velocity corrections can also be applied to static pressures and forces by

$$\frac{1 - C_{p_F}}{1 - C_p} = \frac{C_{d_F}}{C_d} = \frac{C_{l_F}}{C_l} = \frac{C_{m_F}}{C_m} = \frac{1}{(1+\sigma)^2} \doteq 1 - 2\sigma \tag{10}$$

(5) Fluctuating Forces Caused by Vortex Shedding

Vickery[40] has presented a blockage correction for the fluctuating lift based on the analysis by Ross,[96] which predicts

that the ratio $C_{\bar{l}'}/C_D$ is almost independent of the wall confinement. Therefore, to the first approximation, the fluctuating forces can be corrected using the steady force expressions.

(6) Strouhal Number and Vortex Velocity

Using the same model as employed by Maskell and introducing Roshko's[66] Universal Strouhal Number (S_*), Vickery developed an expression for the correction of the Strouhal number,

$$\frac{S_F}{S} = \frac{d_w}{d_{w_F}} \frac{k_F}{k} \tag{11}$$

where $\frac{d_w}{d_{w_F}}$ is the effect of wall constraint on the wake width;

and $k = (1-C_{p_b})^{1/2}$.

On the other hand, the Strouhal number, which is a function of the fluid velocity and vortex shedding frequency, may be affected by their variations. Bearman assumed that the correction for the Strouhal number was a function of the velocity correction only, and neglected any effect of wall interference on the shedding frequency.

To introduce the correction for the vortex shedding frequency, it is appropriate to consider the expression

$$f_v = V_v / a \tag{12}$$

and, thereby, investigate the variations of the vortex velocity and longitudinal spacing with wall interference effects. The vortex velocity is a function of the absolute velocity of the surrounding fluid and the relative velocity of the vortices in the wake, and is given by $V_v = W-u$. Theoretically, for an

unconfined flow, W would equal V_F, and u would be given by Kármán's vortex velocity relation. For the flow in a channel, Glauert[87] has derived using the image method an expression for the reduction of the vortex velocity by the presence of the walls,

$$\frac{u}{U_F} = 1 - 8 e^{-\lambda} \cosh^2 \frac{\pi b}{a} \tag{13}$$

where $\lambda = 2\pi \frac{H}{a}$

However, since $e^{-\lambda}$ is generally very small, the influence of the walls appears to be negligible. The frequency correction can then be expressed in the form

$$\frac{f_{V_F}}{f_V} = \frac{V_{V_F}}{V_V} \frac{a}{a_F} = \frac{V_F - u_F}{W - u_F} \left(\frac{a}{a_F}\right) \tag{14}$$

Using flow continuity as suggested by Glauert, the velocity W on which the vortex system is superimposed is greater than the approaching stream velocity by the amount equal to the backward flow induced by the vortex street and image system. Hence, velocity W is determined by the equation

$$W = V + \frac{\Gamma b}{aH} \tag{15}$$

Using Kármán's stability results,

$$W = V + 2\sqrt{2}\, u_F \frac{b}{H} \tag{16}$$

which can be substituted into the frequency correction equation. The final expression for the free stream Strouhal number is of the form

$$\frac{S_F}{S} = \frac{f_{v_F}}{f_v}\frac{V}{V_F} \qquad (17)$$

Although the Strouhal number forms one of the important parameters in aeroelastic instability studies, the available literature for its correction do not correlate well. Therefore, a series of experimental measurements were conducted with 1, 2, and 3 in. angle sections. The results, plotted in Figure II-2, show the variation of the Strouhal number with blockage for various angles of attack. The extrapolation of these results gives an estimate of the equivalent Strouhal number in an unlimited flow. The percentage correction for the 3 in. model as plotted in Figure II-1, though similar in form to the velocity curves, is generally larger over most of the angle of attack range.

(7) Wake Geometry

The measurements by Rosenhead and Schwabe[71] indicate that both the longitudinal and lateral vortex spacings decrease with increasing blockage at such a rate as to maintain the wake geometry ratio b/a essentially constant. This was determined for model to tunnel width ratios of up to 1/3 and, therefore, is also likely to be representative of the angle model wakes. Glauert,[87] on the other hand, has developed an expression for determining the characteristics of the vortex street in a channel,

$$\frac{b}{b_F} = \frac{a}{a_F} = 1 + \frac{\sqrt{2}}{1-2u_F/V_F}\left(\frac{u_F b_F}{V_F e}\right)\frac{e}{H} \qquad (18)$$

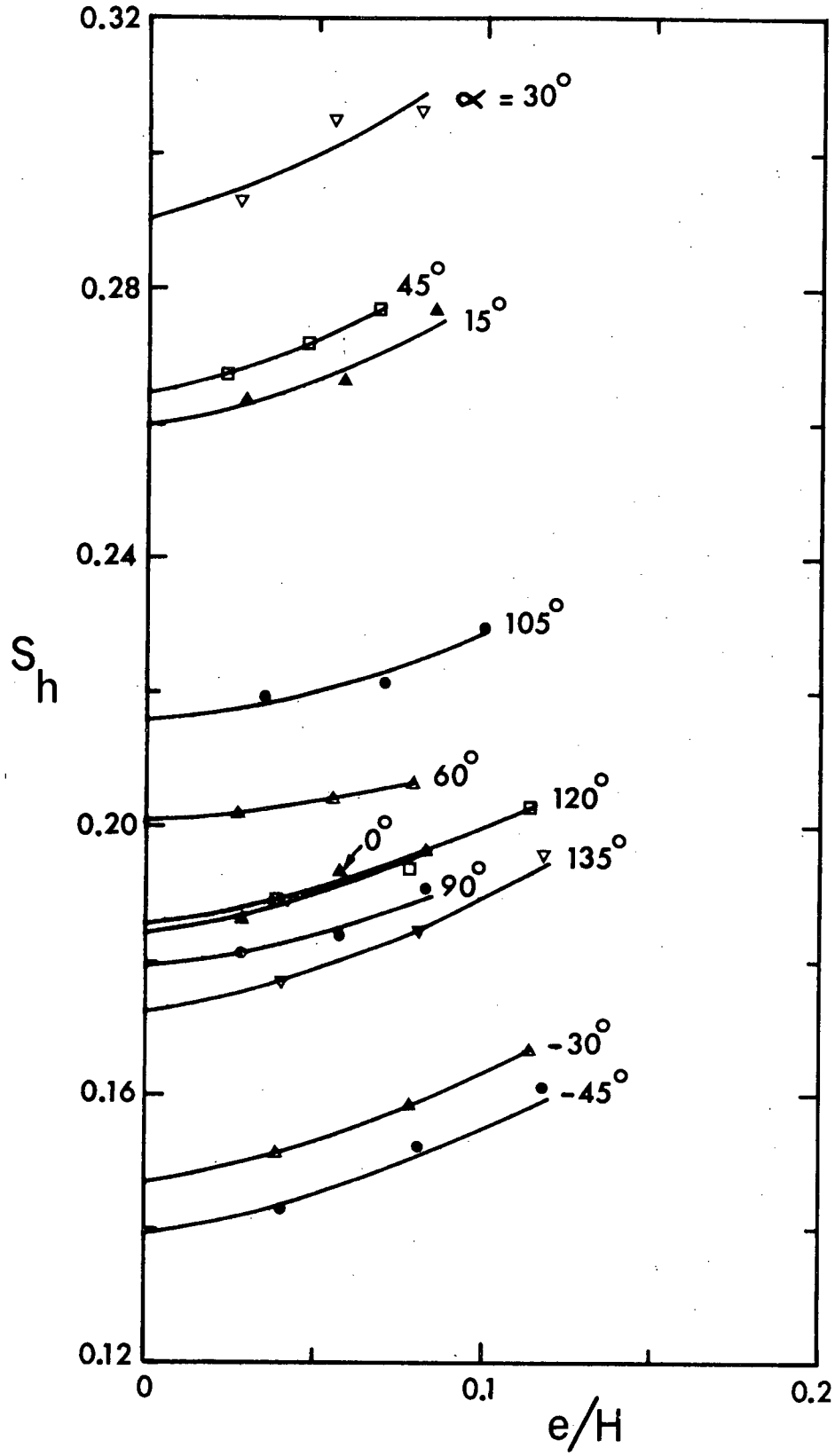

Figure II-2 Variation of Strouhal number with blockage for various orientations of the angle models

which suggests that the dimensions of the wake in a constrained flow are greater than those in an unlimited flow. This is an opposite trend to the experimental measurements by Rosenhead and Schwabe, and contradicts general physical intuition.

Maskell[88] has derived the relationship,

$$\frac{d_{w_F}}{d_w} = 1 + \frac{C_D - C_{D_F}}{(k^2-1)(k_F^2-1)} \frac{S}{C} \qquad (19)$$

indicating the influence of wall constraint on the wake width. However, based on the experimental data for the 3 in. angle model, the second term in the above equation is of the order 0.02 and, therefore, Maskell's analysis suggests that the wake width is approximately independent of the wall constraints.

To establish the correct trend for wall interference on wake geometry, a series of wake measurements were conducted with the 1 in. and 3 in. angle sections. This set of data, indicates that the lateral vortex spacing is confined by the presence of the walls and, thereby, agrees with the trend of the experimental results of Rosenhead and Schwabe. An approximate estimate of the percentage correction for the lateral spacing in the wake of the 3 in. model is plotted in Figure II-1 for comparison.

APPENDIX III

Electronic Instruments

Following is a list of the recording and auxiliary electronic instruments used in the calibration and experimental tests:

Pressure Transducer:	Datametric, Barocel Pressure Sensor, Type 511-10; Signal Conditioner, Type 1015; Power Supply, Type 700.
Filter:	Krohn-Hite, band pass variable filter 0.02 cps-2Kc, model 330B.
Oscilloscope:	Tektronix, Type 564, dual beam storage oscilloscope.
Chart Recorder:	Honeywell, 906C Visicorder; Sub-miniature Galvanometers, Type M100-120 and M200-120; Standard, spec. 2, Visicorder Recording Paper.
Voltmeters:	Hewlett Packard, HP-3400A true rms voltmeter; and HP-412 vacuum tube voltmeter.
Function Generators:	Hewlett Packard, low frequency function generator, model 202A; Heathkit, audio frequency generator, model 1G-72.
Vibration Generator:	Goodmans, Type V47.
Amplifier and Power Supplies:	Low frequency, transistorized power amplifier with two 12 volt d.c. power supplies, built in the department. [97]
R-C damping circuit:	Resistor-capacitor system, variable time constant 0 to 60 seconds, built in the department. [35]
Balance:	Aerolab, 6 component, pyramidal strain gauge balance; two corresponding 3 channel readout electronic cabinets with built-in d.c. voltmeters.
Time-Mark Generator:	Tektronix, Type 184, 2 nanoseconds to 5 seconds crystal oscillator.

Lateral Displacement Transducer:	Air-core transformer, built in the department. [49]
Lateral Transducer Demodulator:	Full wave rectifier and RC filter, built in the department. [49]
Dampers and Power Supplies:	Electromagnetic dampers; variable d.c. and a.c. power supplies, built in the department. [49]
Power Supply:	Electro, variable, filtered, d.c. power supply, Model D-612T.
Variac:	General Radio Company, Type W5M, adjustable autotransformer.
Strobotachometer:	General Radio Company, Strobotac, Type 1531.
Angular Displacement Transducer:	4-arm strain-gauge bridge, built in the department.
Angular Transducer Power Supply and Output System:	Ellis, Bridge-Amplifier-Meter, Model BAM-1.

APPENDIX IV

Theory for Plunging or Torsional Degree of Freedom

1 General Equations of Motion

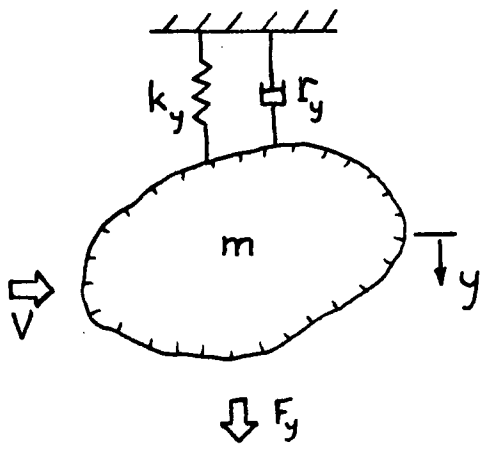

Figure IV-1

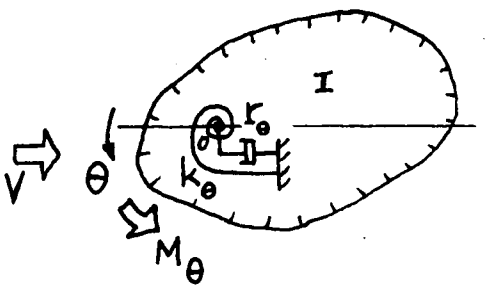

Figure IV-2

The system of mass m (Figure IV-1), restrained to a plunging degree of freedom perpendicular to the flow direction, is subjected to linear spring and viscous damping forces and aerodynamic loading F_y. A corresponding system with a torsional degree of freedom is shown in Figure IV-2. It is convenient to express the aerodynamic terms in coefficient form which, in general, may be a function of model displacement and velocity, and time t. Using the Lagrangian formulation, the equation of motion for the plunging and torsional degrees of freedom become

$$m\ddot{y} + r_y\dot{y} + k_y y = \tfrac{1}{2}\rho V^2 h l C_{F_y}(y, \dot{y}; t) \qquad (1)$$

$$I\ddot{\theta} + r_\theta\dot{\theta} + k_\theta\theta = \tfrac{1}{2}\rho V^2 h^2 l C_{M_\theta}(\theta, \dot{\theta}; t) \qquad (2)$$

These equations are analyzed with vortex resonant or galloping excitations to determine the aeroelastic instability of angle sections.

2 Vortex Resonance

The analysis considers plunging degree of freedom only since the torsional solution is similar. For transverse excitation due to vortex shedding, the force coefficient is approximated by a sinusoidal function of amplitude $C_{\bar{l}}$, and frequency ω_v. Equation (1) then becomes

$$m\ddot{y} + r_y\dot{y} + k_y y = \tfrac{1}{2}\rho V^2 h \ell C_{\bar{l}} \sin \omega_v t \tag{3}$$

which can be written in the nondimensional form

$$\Omega_v^2 \ddot{Y} + 2\beta_y \Omega_v \dot{Y} + Y = \eta_y U^2 C_{\bar{l}} \sin \tau_v \tag{4}$$

giving the steady-state amplitude as

$$\bar{Y} = \eta_y C_{\bar{l}} \frac{U^2}{\sqrt{(1-\Omega_v^2)^2 + (2\beta_y \Omega_v)^2}} \tag{5}$$

Therefore, the resonant amplitude becomes

$$\bar{Y}_{max} = \frac{1}{2}\frac{\eta_y}{\beta_y} C_{\bar{l}} U_{res}^2 \tag{6}$$

For a physical system consisting of an elastically mounted cylinder in an air flow, it has been observed that the oscillations near the resonance peak do not comply with the prediction of the simple mathematical model, but rather exhibit a phenomenon called vortex capture. Parkinson,et al[79] solved equation (1), approximately, under the conditions of vortex capture by assuming

and

$$y = \bar{y} \sin \omega_{c_y} t$$

$$C_{F_y} = C_{\bar{l}'} \sin (\omega_{c_y} t + \Phi_{AF}) \tag{7}$$

The final expression for the resonant displacement now becomes

$$\bar{Y}_{max} = \frac{\omega_{n_y}}{\omega_{c_y}} \frac{n_y U^2}{2 \beta_y} C_{\bar{l}'} \sin \Phi_{AF} \tag{8}$$

3 Galloping of Aerodynamically Unstable Section

3.1 Preliminary Remarks

Geometrically bluff sections may exhibit a galloping type of oscillation because of the nature of the aerodynamic forces or moment. If, from the mean angle of attack α_o, the aerodynamic loading shows an increase with model attitude and the amount of resulting energy input by the fluid force exceeds that dissipated by the viscous damping, then oscillations will continue to grow until a net energy balance is established. The quasi-steady approach is adopted so that the instantaneous forcing function acting on the oscillating model can be replaced by its steady value acting on the stationary model oriented at the same apparent angle of attack. This assumption implies that no aerodynamic hysteresis effects exist in the force or moment characteristics and the vortex shedding frequency is far removed from the cylinder frequency.

From the nature of the problem, the lateral force or twisting moment turn out to be highly nonlinear functions. However, certain simplifications are possible in the aeroelastic problem since:

(i) the ratio of air density to model density is small and consequently, the aerodynamic force is small compared with the elastic and inertial forces of the system;

(ii) the frequency of oscillation is close to the natural frequency;

(iii) the equilibrium motion is nearly sinusoidal.

Under these assumptions the problem becomes quasi-linear which can be solved by various analytical techniques.

For the plunging degree of freedom, the quasi-steady theory has been established by Scruton[15] and Parkinson, et al.[16-18] Sisto[14] and Ii,[19] considering the problem of stall-flutter, incorporated the downwash condition at the three-quarter point to simplify the analysis. For the torsional galloping of bluff cylinders a modified theory following the plunging quasi-steady approach is presented. However, the torsional analysis is slightly more complicated since the nonlinear aerodynamic moment is a function of the instantaneous angular position as well as the velocity. A derivation of the basic expressions for the plunging and torsional degrees of freedom is given in the following sections.

3.2 Plunging Degree of Freedom

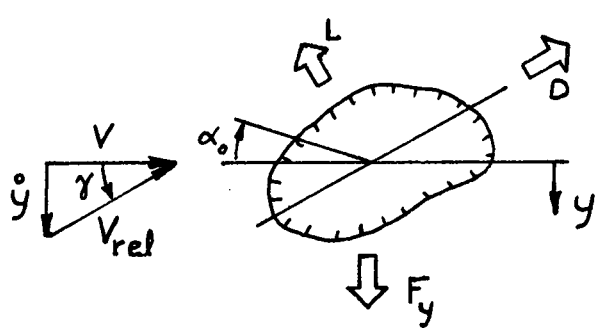

Figure IV-3

Following the analysis established by Parkinson and associates,[17] the instantaneous aerodynamic force (Figure IV-3) is related to the steady lift and drag by

$$F_y = -(L\cos\gamma + D\sin\gamma) \tag{9}$$

where

$$L = \tfrac{1}{2}\rho V_{rel}^2 h l C_L$$
$$D = \tfrac{1}{2}\rho V_{rel}^2 h l C_D \tag{10}$$

and the instantaneous angle of attack $\alpha = \alpha_o + \gamma$. Noting that $V = V_{rel}\cos\gamma$, the final expression for the force coefficient becomes

$$C_{F_y} = -(C_L + C_D \tan\gamma)\sec\gamma \tag{11}$$

The change in model attitude is related to the transverse velocity component by

$$\gamma = \tan^{-1}\frac{\dot{y}}{V} \tag{12}$$

Therefore, the governing equation (1) becomes

$$m\ddot{y} + r_y\dot{y} + k_y y = \tfrac{1}{2}\rho V^2 h l C_{F_y}(\dot{y}) \tag{13}$$

It has been customary to obtain an expression for C_{F_y} in the form of a polynomial using C_L and C_D experimental data, and analyze the particular case where the model is mounted at a symmetrical angle of attack. In this case, C_{F_y} is an odd function. Santosham[50] considered the problem of aeroelastic insta-

bility of rectangular sections and used odd functioned Chebyshev polynomials of 11th degree for obtaining the solutions. However, for analyzing the galloping oscillations of an angle section, the theory has been generalized to consider the model oriented at unsymmetrical angles of attack and the degree of the polynomial containing all terms has been extended to 25. However, the actual degree of the polynomial used is 25 or less based on a least square error criterion. Thereby, the expression for C_{F_y} can be written in the polynomial form

$$C_{F_y} = a_1\left(\frac{\dot{y}}{V}\right) + a_2\left(\frac{\dot{y}}{V}\right)^2 + a_3\left(\frac{\dot{y}}{V}\right)^3 + a_4\left(\frac{\dot{y}}{V}\right)^4 + \cdots + a_N\left(\frac{\dot{y}}{V}\right)^N \qquad (14)$$

where $N \leq 25$.

Note that $a_o = 0$ because y represents the displacement from the apparent zero position governed by the steady lift force. C_{F_y} is generally plotted as a function of tan γ, since $(\dot{y}/V)$ and tan γ are directly related by (12).

Equation (13) can be nondimensionalized to

$$\ddot{Y} + Y = -2\beta_y \dot{Y} + n_y U^2 C_{F_y}(\dot{Y}) \qquad (15)$$

or combining the two terms on the right hand side to give

$$\ddot{Y} + Y = \mu_y f_y(\dot{Y}) \qquad (16)$$

where $\mu_y = n_y a_1$

and $$f_y(\dot{Y}) = \left\{(U-U_o)\dot{Y} + \frac{a_2}{a_1}\dot{Y}^2 + \frac{a_3}{a_1 U}\dot{Y}^3 + \cdots + \frac{a_N}{a_1 U^{N-2}}\dot{Y}^N\right\} \qquad (17)$$

Based on the aforementioned assumption, $\mu_y << 1$; therefore, (16) is a quasi-linear differential equation of the autonomous

type. Actually, the quasi-linear form requires the complete right hand side of equation (16) to remain small, thus specifying, implicity, an upper limit to the velocity U.

Using the Variation of Parameter method, the first order approximate solution of equation (16), when $\mu_y = 0$, is of the form

$$Y = \bar{Y} \sin(\tau + \phi) \tag{18}$$

therefore

$$\dot{Y} = \bar{Y} \cos(\tau + \phi)$$

For $\mu_y << 1$, the first order solution is determined by reducing (16) to a system of first order differential equations

$$\begin{aligned} \dot{Y} &= Z \\ \dot{Z} &= -Y + \mu_y f_y(Z) \end{aligned} \tag{19}$$

considering

$$\begin{aligned} Y &= \bar{Y} \sin(\tau + \phi) \\ Z &= \bar{Y} \cos(\tau + \phi) \\ \psi &= \tau + \phi \end{aligned} \tag{20}$$

and assuming $\bar{Y}$ and ϕ to be functions of time τ, equation (19) reduces to

$$\begin{aligned} \frac{d\bar{Y}}{d\tau} &= \mu_y f_y[\bar{Y} \cos\psi] \cos\psi \\ \frac{d\phi}{d\tau} &= -\frac{\mu_y}{\bar{Y}} f_y[\bar{Y} \cos\psi] \sin\psi \end{aligned} \tag{21}$$

Since $\frac{d\bar{Y}}{d\tau}$ and $\frac{d\phi}{d\tau}$ are proportional to μ_y, $\bar{Y}$ and ϕ will be slowly varying functions of time. Hence, $\bar{Y}$ and ϕ can be considered, approximately, constant during one cycle. Equa-

tion (21) can then be replaced by their average values

$$\frac{d\bar{Y}}{d\tau} = \frac{\mu_y}{2\pi}\int_0^{2\pi} f_y[\bar{Y}\cos\psi]\cos\psi\, d\psi$$
$$\frac{d\phi}{d\tau} = -\frac{\mu_y}{2\pi\bar{Y}}\int_0^{2\pi} f_y[\bar{Y}\cos\psi]\sin\psi\, d\psi \qquad (22)$$

By examining $\dot{\phi}$ and recalling the polynomial form of the function $f_y(\dot{Y})$, the integrand can be replaced by a Fourier sine series. Upon integration each term in this series vanishes and, therefore, (22) can be written as

$$\frac{d\bar{Y}}{d\tau} = -\bar{Y}\,\delta_y(\bar{Y})$$
$$\frac{d\phi}{d\tau} = 0 \qquad (23)$$

where

$$\delta_y(\bar{Y}) = -\frac{\mu_y}{2\pi\bar{Y}}\int_0^{2\pi} f_y[\bar{Y}\cos\psi]\cos\psi\, d\psi \qquad (24)$$

On substituting (17) into (24), δ_y becomes

$$\delta_y(\bar{Y}) = -\frac{\mu_y}{2}\left\{(U-U_0) + b_3\frac{a_3}{a_1U}\bar{Y}^2 + b_5\frac{a_5}{a_1U^3}\bar{Y}^4 + \cdots + b_k\frac{a_k}{a_1U^{k-2}}\bar{Y}^{k-1}\right\} \qquad (25)$$

where

$$k = \begin{cases} N & \text{for } N \text{ odd} \\ N-1 & \text{for } N \text{ even} \end{cases}$$

and

$$b_1 = 1$$

$$b_i = \frac{i}{i+1}\, b_{i-2} \quad , \quad i = 3,5,7,\cdots,k\ .$$

The displacement amplitudes of the limit cycles are obtained by determining the real positive roots $\bar{Y}_j$ of the $\delta_y(\bar{Y})$

polynomial, from which the stability of the sustained motions can be analyzed.

3.3 Torsional Degree of Freedom

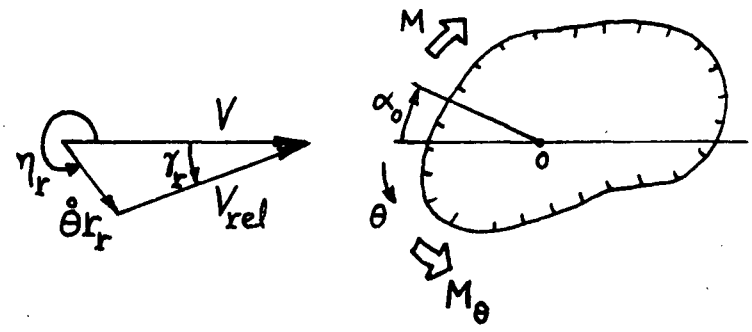

Figure IV-4

For the analysis of the torsional degree of freedom, the excitation is the instantaneous moment M_θ, which using the quasi-steady approach can be related to the experimental value, M, by

$$C_{M_\theta} = -\frac{V_{rel}^2}{V^2} C_M(\alpha) \tag{26}$$

where

$$C_M = M/(\tfrac{1}{2}\rho V_{rel}^2 h^2 \ell)$$

$$\alpha = \alpha_o - \theta + \gamma_r \tag{27}$$

It is apparent that V_{rel} is different from V in both magnitude and direction because of the angular velocity $\dot{\theta}$. Furthermore, each surface element on the contour experiences a different relative velocity governed by its position with respect to the centre of rotation. It is assumed that an effective relative

velocity can be written as

$$v_r = \dot{\theta} r_r e^{i\eta_r} \tag{28}$$

where r_r is the effective radius of rotation and η_r is the direction of v_r. For the angle model suspended about the centre of gravity at $\alpha_o = 0°$, the representative parameter values suitably nondimensionalized are

$$\begin{aligned} R_r &= 0.3015 \\ \eta_{r_o} &= \frac{5\pi}{4} \end{aligned} \tag{29}$$

For different angles of attack, the representative direction angle η_r can be obtained using the relation

$$\eta_r = \eta_{r_o} - (\alpha_o - \theta) \tag{30}$$

The approach when applied to a flat plate airfoil gives an effective downwash velocity at the three-quarter chord point. This agrees with the value adopted in the stall flutter analysis by Sisto[14] and Ii.[19]

For the oscillating cylinder, the overall velocity vector diagram is as shown in Figure IV-4. Hence, the relative velocity can be written as

$$\left(\frac{V_{rel}}{V}\right)^2 = 1 - \frac{2\dot{\theta} r_r}{V} \cos\eta_r + \left(\frac{\dot{\theta} r_r}{V}\right)^2 \tag{31}$$

and the representative angle γ_r becomes

$$\gamma_r = \tan^{-1}\left\{\frac{-\dot{\theta} r_r \sin\eta_r}{V - \dot{\theta} r_r \cos\eta_r}\right\} \tag{32}$$

In nondimensional form, the governing differential equation of motion (2) becomes

$$\ddot{\Theta} + \Theta = -2\beta_\theta \dot{\Theta} + \eta_\theta U^2 C_{M_\theta}(\Theta, \dot{\Theta}) \tag{33}$$

with auxiliary expressions transformed to

$$C_{M_\theta} = -\left(\frac{U_{rel}}{U}\right)^2 C_M(\alpha)$$

$$\alpha = \alpha_0 - \Theta + \gamma_r$$

$$\left(\frac{U_{rel}}{U}\right)^2 = 1 - 2\frac{\dot{\Theta}R_r}{U}\cos\eta_r + \left(\frac{\dot{\Theta}R_r}{U}\right)^2 \tag{34}$$

$$\gamma_r = \tan^{-1}\left\{\frac{-\frac{\dot{\Theta}R_r}{U}\sin\eta_r}{1-\frac{\dot{\Theta}R_r}{U}\cos\eta_r}\right\}$$

$$\eta_r = \eta_{r_0} - (\alpha_0 - \Theta)$$

Upon evaluation of C_{M_θ} as a function of Θ and $\dot{\Theta}$ from equations (34), it was observed that lines of constant C_{M_θ} were almost linear and parallel at an angle λ to the $\dot{\Theta}$ axis. As a result, a new cartesian coordinate system, ξ and ζ, was established with ζ axis along the contourline $C_{M_\theta} = 0$. Therefore, to a first approximation, C_{M_θ} can be expressed as a function of ξ which is related to Θ and $\dot{\Theta}$ by the coordinate transformation

$$\xi = \left[\frac{\dot{\Theta}}{U}s - \Theta c\right] \tag{35}$$

where $s = \sin\lambda$

and $c = \cos\lambda$

Similar to the plunging case, the aerodynamic moment coefficient is expressed as a polynomial in ξ

$$C_{M_\theta} = a_1 \xi + a_2 \xi^2 + a_3 \xi^3 + \cdots + a_N \xi^N \tag{36}$$

where $N \leq 25$.

Substituting (35) and (36) into (33) and combining the two terms on the right hand side, the nondimensional equation of motion reduces to the form

$$\ddot{\Theta} + \Theta = \mu_\theta f_\theta(\Theta, \dot{\Theta}) \tag{37}$$

where $\mu_\theta = n_\theta a_1$

and

$$f_\theta(\Theta,\dot{\Theta}) = U^2\left\{\left(\frac{U_s - U_o}{U^2}\right)\dot{\Theta} - c\Theta + \frac{a_2}{a_1}\left(\frac{\dot{\Theta}}{U}s - \Theta c\right)^2 + \frac{a_3}{a_1}\left(\frac{\dot{\Theta}}{U}s - \Theta c\right)^3 + \cdots + \frac{a_N}{a_1}\left(\frac{\dot{\Theta}}{U}s - \Theta c\right)^N\right\} \tag{38}$$

For a system in air, $\mu_\theta << 1$.

Using the method of Variation of Parameters as in the plunging analysis, the solution of (37) can be written as

$$\frac{d\bar{\Theta}}{d\tau} = -\bar{\Theta}\,\delta_\theta(\bar{\Theta})$$
$$\frac{d\phi}{d\tau} = -K_\theta(\bar{\Theta}) \tag{39}$$

where

$$\delta_\theta(\bar{\Theta}) = -\frac{\mu_\theta}{2\pi\bar{\Theta}}\int_0^{2\pi} f_\theta[\bar{\Theta}\sin\psi, \bar{\Theta}\cos\psi]\cos\psi\, d\psi$$
$$K_\theta(\bar{\Theta}) = \frac{\mu_\theta}{2\pi\bar{\Theta}}\int_0^{2\pi} f_\theta[\bar{\Theta}\sin\psi, \bar{\Theta}\cos\psi]\sin\psi\, d\psi \tag{40}$$

Note, the variation of phase with time which was not present in the plunging case. Substituting (38) into (40) and carrying out the integration, δ_θ and K_θ become

$$\delta_\theta(\bar{\Theta}) = -\frac{\mu_\theta U^2}{2}\Big[\Big(\frac{U_s - U_o}{U^2}\Big) + \frac{a_3}{a_1}\Big\{\Big(\frac{s}{U}\Big)^3 b_{3,1} + \Big(\frac{s}{U}\Big) c^2 b_{3,3}\Big\}\bar{\Theta}^2$$
$$+\cdots+\frac{a_i}{a_1}\Big\{\Big(\frac{s}{U}\Big)^i b_{i,1}+\Big(\frac{s}{U}\Big)^{i-2} c^2 b_{i,3}+\cdots+\Big(\frac{s}{U}\Big)^{i-(j-1)} c^{j-1} b_{i,j} \qquad (41)$$
$$+\cdots+\Big(\frac{s}{U}\Big) c^{i-1} b_{i,i}\Big\}\bar{\Theta}^{i-1}+\cdots.\Big]$$

$$K_\theta(\bar{\Theta}) = -\frac{\mu_\theta U^2}{2}\Big[\, c + \frac{a_3}{a_1}\Big\{\Big(\frac{s}{U}\Big)^2 c\, t_{3,2} + c^3 t_{3,4}\Big\}\bar{\Theta}^2$$
$$+\cdots+\frac{a_i}{a_1}\Big\{\Big(\frac{s}{U}\Big)^{i-1} c\, t_{i,2}+\Big(\frac{s}{U}\Big)^{i-3} c^3 t_{i,4}+\cdots+\Big(\frac{s}{U}\Big)^{i-j} c^j t_{i,j+1} \qquad (42)$$
$$+\cdots+ c^i t_{i,i+1}\Big\}\bar{\Theta}^{i-1}+\cdots.\Big]$$

where $\quad i = 3, 5, 7, \cdots, N \quad ; \quad j = 1, 3, 5, \cdots, i \quad .$

The coefficients $b_{i,j}$ and $t_{i,j+1}$ are given by

$$b_{i,j} = c_{i,j}\, d_{i,j}$$
$$\qquad (43)$$
$$t_{i,j+1} = c_{i,j+1}\, s_{i,j+1}$$

Here the $c_{i,j}$ are the binomial coefficients of the terms in equation (38), and $d_{i,j+1}$ and $s_{i,j+1}$ are constants obtained from the integration of equation (40). These coefficients can be determined from the following expressions:

$$c_{i,1} = c_{i,i+1} = d_{i,1} = g_{i,1} = e_{i,i} = 1$$

$$c_{i,k+1} = \frac{i-(k-1)}{k}\, c_{i,k}$$

$$g_{i,j+2} = \frac{j}{(i+1)-(j-1)}\, g_{i,j}$$

$$e_{i,i-j-1} = \frac{j+2}{j+3}\, e_{i,i-j+1} \qquad (44)$$

$$d_{i,j+2} = g_{i,j+2}\, e_{i,j}$$

$$s_{i,j+1} = d_{i,i-j+1}$$

where $i = 1,3,5,\cdots,N$; $j = 1,3,5,\cdots,i$; $k = 1,2,3,\cdots,i-1$.

The amplitudes of the limit cycles can be obtained from (39) using the condition, $d\bar{\Theta}/d\tau = 0$. The stability of the sustained motions can be analyzed by examining the sign of $\partial \delta_\theta / \partial \bar{\Theta}$ evaluated at these limit cycles.

On determining the limit cycle amplitude, ϕ can be evaluated using equation (42) as

$$\phi = -K_\theta \tau + \phi_o \qquad (45)$$

where ϕ_o is the constant of integration. Thus, the steady-state

amplitude of oscillation is given by

$$\Theta = \bar{\Theta} \sin \psi \tag{46}$$

where $$\psi = \tau + \phi = (1 - K_\theta)\tau + \phi_o \tag{47}$$

From (47) it appears that the frequency of oscillation is reduced from the natural frequency by the amount K_θ. Therefore, the second equation of (39) in terms of the reduced frequency parameter becomes

$$1 + \dot{\phi} = 1 - K_\theta \tag{48}$$